

Copyright
by
Gurpreet Singh
2014

The Dissertation Committee for Gurpreet Singh
certifies that this is the approved version of the following dissertation:

**Coupled Flow and Geomechanics Modeling for
Fractured Poroelastic Reservoirs**

Committee:

Mary Fanett Wheeler, Supervisor

Todd James Arbogast

Mojdeh Delshad

Marc Hesse

Sanjay Srinivasan

**Coupled Flow and Geomechanics Modeling for
Fractured Poroelastic Reservoirs**

by

Gurpreet Singh, B.S., M.S.

DISSERTATION

Presented to the Faculty of the Graduate School of
The University of Texas at Austin
in Partial Fulfillment
of the Requirements
for the Degree of

DOCTOR OF PHILOSOPHY

THE UNIVERSITY OF TEXAS AT AUSTIN

December 2014

Mukat nahee bidi-aa bigi-aan.

(Liberation does not come from learning without understanding.)

- Guru Granth Sahib (903-14)

Acknowledgments

I am grateful to my family for their patience and unwavering moral support all through these years. To my father, who taught me perseverance and to laugh in the face of difficulties. To my mother, for her calming advice in matters which seemed irresolvable to me. To my you younger brother, for his witty humor and for taking care of mother and father in my absence.

I thank my advisor, Dr. Mary Fanett Wheeler for guiding my doctoral research and for providing a nurturing environment with an abundant supply of enthusiasm. I must especially mention here that Dr. Wheeler's enthusiasm is at the same level as mine, when I was 20 years old. I was never short of resources and knowing it takes substantial amount of effort in gathering them, I am grateful for your support. I will do my best to carry your school of thought forward.

I would also like to thank my committee members, Drs. Todd James Arbogast, Mojdeh Delshad, Marc Hesse and Sanjay Srinivasan for their suggestions and inputs. To Dr. Arbogast for overlooking all the spelling mistakes and inadvertent corrections. I am thankful to all of you for your time and patience.

I am thankful to Dr. Gergina Pencheva who taught me the basics of mixed finite element method and helped me come up to speed in a very short

period of time. To Dr. Kundan Kumar for helping me structure my research and for his advice in different matters from time to time. You are the most cheerful person I have met over the years.

To Dr. Thomas Wick for his German efficiency which helped me expand my research interests to geomechanics. I wish to outperform you in beer drinking one day. To Dr. Benjamin Ganis for the fruitful discussions and swift implementations. I would like to thank Connie Baxter for all the help which goes unseen sometimes and for spearheading the green revolution. Also to my friends Prashant Mittal and Reza Tavakoli. Thank you for making Center for Subsurface Modeling the best academic experience I have had so far.

I am thankful to my friends Ashwin Venkatraman, Hariharan Ramachandran and Lokendra Jain who have been my brothers in arms. The research discussions and hard work is finally manifesting itself in the form of cooking skills. To Ameya Chaudhary and Nishant Panda for listening to my tangential rants during coffee breaks and while loitering in the student lounge.

Last but not the least, I am thankful to my friends Engin Hassamanci, Himanshu Chauhan, Can Pehlivan Türk, Sara Pınar Önder and Stephanie Rose Taylor for enriching my experiences beyond the confines of academia.

Coupled Flow and Geomechanics Modeling for Fractured Poroelastic Reservoirs

Publication No. _____

Gurpreet Singh, Ph.D.

The University of Texas at Austin, 2014

Supervisor: Mary Fanett Wheeler

Tight gas and shale oil play an important role in energy security and in meeting an increasing energy demand. Hydraulic fracturing is a widely used technology for recovering these resources. The design and evaluation of hydraulic fracture operation is critical for efficient production from tight gas and shale plays. The efficiency of fracturing jobs depends on the interaction between hydraulic (induced) and naturally occurring discrete fractures. In this work, a coupled reservoir-fracture flow model is described which accounts for varying reservoir geometries and complexities including non-planar fractures. Different flow models such as Darcy flow and Reynold's lubrication equation for fractures and reservoir, respectively are utilized to capture flow physics accurately.

Furthermore, the geomechanics effects have been included by considering a multiphase Biot's model. An accurate modeling of solid deformations

necessitates a better estimation of fluid pressure inside the fracture. The fractures and reservoir are modeled explicitly allowing accurate representation of contrasting physical descriptions associated with each of the two. The approach presented here is in contrast with existing averaging approaches such as dual and discrete-dual porosity models where the effects of fractures are averaged out. A fracture connected to an injection well shows significant width variations as compared to natural fractures where these changes are negligible. The capillary pressure contrast between the fracture and the reservoir is accounted for by utilizing different capillary pressure curves for the two features.

Additionally, a quantitative assessment of hydraulic fracturing jobs relies upon accurate predictions of fracture growth during slick water injection for single and multistage fracturing scenarios. It is also important to consistently model the underlying physical processes from hydraulic fracturing to long-term production. A recently introduced thermodynamically consistent phase-field approach for pressurized fractures in porous medium is utilized which captures several characteristic features of crack propagation such as joining, branching and non-planar propagation in heterogeneous porous media. The phase-field approach captures both the fracture-width evolution and the fracture-length propagation. In this work, the phase-field fracture propagation model is briefly discussed followed by a technique for coupling this to a fractured poroelastic reservoir simulator.

We also present a general compositional formulation using multipoint

flux mixed finite element (MFME) method on general hexahedral grids with a future prospect of treating energized fractures. The mixed finite element framework allows for local mass conservation, accurate flux approximation and a more general treatment of boundary conditions. The multipoint flux inherent in MFME scheme allows the usage of a full permeability tensor. An accurate treatment of diffusive/dispersive fluxes owing to additional velocity degrees of freedom is also presented. The applications areas of interest include gas flooding, CO₂ sequestration, contaminant removal and groundwater remediation.

Table of Contents

| | |
|--|------------|
| Acknowledgments | v |
| Abstract | vii |
| List of Tables | xv |
| List of Figures | xvi |
| Chapter 1. Introduction | 1 |
| 1.1 Problem Statement | 1 |
| 1.2 Research Objectives | 3 |
| 1.3 Thesis Outline | 4 |
| Chapter 2. Single Phase Flow | 7 |
| 2.1 Model Formulation | 7 |
| 2.1.1 Boundary & Initial Conditions | 8 |
| 2.1.2 Closure and Other Conditions | 8 |
| 2.2 Weak Formulation | 9 |
| 2.2.1 Finite element spaces | 9 |
| 2.2.2 Quadrature Rules | 11 |
| 2.2.3 Fully Discrete Formulation | 12 |
| 2.3 Linearization | 12 |
| 2.3.1 Reduction to a Cell-Centered Stencil | 13 |
| Chapter 3. Two-phase Flow | 18 |
| 3.1 Formulation I | 19 |
| 3.1.1 Boundary & Initial Conditions | 19 |
| 3.2 Formulation II | 20 |
| 3.2.1 Boundary & Initial Conditons | 21 |

| | | |
|--|--|-----------|
| 3.3 | Closure & Other Conditions | 21 |
| 3.4 | Fully Discrete Formulation | 22 |
| 3.4.1 | Formulation I | 23 |
| 3.4.2 | Formulation II | 24 |
| 3.5 | Linearization | 26 |
| 3.5.1 | Formulation I | 26 |
| 3.5.2 | Formulation II | 27 |
| 3.6 | Results | 28 |
| 3.6.1 | Capillary End Effect | 29 |
| 3.6.2 | Capillary and Gravity Equilibrium | 30 |
| Chapter 4. Compositional Flow | | 34 |
| 4.1 | Introduction | 34 |
| 4.2 | Model Formulation | 38 |
| 4.2.1 | Component conservation equations | 39 |
| 4.2.2 | Boundary and initial conditions | 40 |
| 4.2.3 | Closure and constraints | 41 |
| 4.3 | Hydrocarbon Phase Behavior Model | 42 |
| 4.4 | Fully Discrete Formulation | 46 |
| 4.4.1 | Treatment of diffusion/dispersion | 48 |
| 4.5 | Linearization | 49 |
| 4.6 | Results | 51 |
| 4.6.1 | Verification and benchmarking | 51 |
| 4.6.2 | Full permeability tensor test | 53 |
| 4.6.3 | Checker-board pattern test | 54 |
| 4.6.4 | Frio field test case | 55 |
| 4.6.5 | Brugge field CO ₂ flooding | 57 |
| Chapter 5. Coupled Two-Phase Reservoir Fracture Flow and Geomechanics Model | | 61 |
| 5.1 | An Illustrative Example | 66 |
| 5.2 | Model Formulation | 70 |
| 5.2.1 | Equations in the reservoir ($\Omega \setminus \Gamma$) | 71 |

| | | |
|---------|--|-----|
| 5.2.1.1 | Flow equations | 71 |
| 5.2.1.2 | Mechanics | 72 |
| 5.2.2 | Equations in the fracture (Γ) | 73 |
| 5.2.3 | Closure conditions | 73 |
| 5.2.4 | Boundary, interface and initial conditions | 74 |
| 5.2.4.1 | Case I | 75 |
| 5.2.4.2 | Case II | 75 |
| 5.2.4.3 | Case III | 75 |
| 5.3 | Solution Algorithm and Discretization | 76 |
| 5.4 | Iterative Coupling | 80 |
| 5.4.1 | Reservoir and fracture pressure coupling | 80 |
| 5.4.1.1 | Explicit coupling | 81 |
| 5.4.1.2 | Implicit Coupling | 83 |
| 5.4.2 | Pressure and saturation coupling | 84 |
| 5.4.3 | Flow and mechanics coupling | 86 |
| 5.5 | Fully Discrete Formulation | 87 |
| 5.6 | Linearization | 91 |
| 5.6.1 | Explicit Coupling | 91 |
| 5.6.2 | Implicit coupling | 92 |
| 5.7 | Results | 93 |
| 5.7.1 | Capillary imbibition in a fractured core | 94 |
| 5.7.2 | Discrete natural fractures | 98 |
| 5.7.3 | Multi-stage hydraulic fracture | 100 |
| 5.7.4 | Coupled flow and mechanics | 102 |
| 5.7.5 | Frio field case with natural fractures | 104 |
| 5.8 | Nomenclature | 108 |

Chapter 6. Coupled Fracture Propagation and Reservoir Flow Model 110

| | | |
|-------|---|-----|
| 6.1 | Introduction | 110 |
| 6.2 | Pressurized and Fluid-filled Crack Propagation Models using Phase-field | 115 |
| 6.2.1 | Pressurized fracture propagation model (two-field problem) | 117 |

| | | |
|--|---|------------|
| 6.2.2 | Fluid-filled fracture propagation model (three-field problem) | 120 |
| 6.2.3 | Discretization and solution algorithm | 122 |
| 6.3 | Integrating Phase-field Crack Propagation and Fractured Reservoir Flow Models | 122 |
| 6.3.1 | Projection of variables/ mesh reconstruction | 125 |
| 6.3.2 | Fractured well model | 128 |
| 6.4 | Results | 130 |
| 6.4.1 | Comparing fracture propagation in 3D and 2D domains | 133 |
| 6.4.2 | Effect of fracture spacing on fracture growth | 135 |
| 6.4.3 | Effect of discrete fractures on fracture growth | 136 |
| 6.4.4 | Effect of heterogeneity on fracture growth | 137 |
| 6.4.5 | Effect of stress shadowing on fracture growth | 139 |
| 6.4.6 | Coupling the phase-field model to a reservoir simulator | 143 |
| 6.5 | Nomenclature | 148 |
| Chapter 7. Conclusions and Recommendations | | 150 |
| Appendices | | 152 |
| Appendix A. Wellbore Models | | 153 |
| A.1 | Introduction | 153 |
| A.2 | Vertical Well Models | 154 |
| A.2.1 | Bottomhole Pressure Specified Wells | 158 |
| A.2.2 | Rate Specified Wells | 158 |
| A.3 | Horizontal/Deviated Well Models | 159 |
| A.3.1 | Bottomhole Pressure Specification | 161 |
| A.3.2 | Rate Specified Wells | 161 |
| Appendix B. Phase Behavior Model: Derivatives | | 162 |
| B.1 | Peng-Robinson Cubic Equation of State | 162 |
| B.2 | Derivatives of Fugacity Equation | 163 |
| B.2.1 | Derivative with respect to pressure (P^*) | 164 |
| B.2.2 | Derivative with respect to component concentration (N_k) | 165 |

| | | |
|-------|--|------------|
| B.2.3 | Derivative with respect to $\ln K_k$ | 166 |
| B.2.4 | Derivative with respect to ν | 168 |
| | Bibliography | 169 |

List of Tables

| | | |
|-----|---|-----|
| 3.1 | Rock and fluid property information | 29 |
| 5.1 | Capillary imbibition: rock and fluid property information . . . | 95 |
| 5.2 | Multi-stage hydraulic fractures: reservoir and fluid properties . | 101 |
| 5.3 | Frio with fractures: reservoir and fluid properties | 106 |
| 6.1 | Brugge field: reservoir and fluid properties | 144 |

List of Figures

| | | |
|-----|---|----|
| 2.1 | Velocity degrees of freedom associated with the corner marked red along x (left), y (middle) and z (right) directions | 14 |
| 2.2 | Coupling velocity and pressure degrees of freedom corresponding to a vertex | 16 |
| 3.1 | Flowchart depicting iteratively coupled IMPES/IMPEC schemes | 22 |
| 3.2 | Oil and water phase relative permeability curves | 29 |
| 3.3 | Rock matrix capillary pressure curve | 30 |
| 3.4 | Cylindrical core | 31 |
| 3.5 | Water phase pressure distribution after 2 (left) and 4 (right) days | 31 |
| 3.6 | Water saturation distribution after 2 (left) and 4 (right) days . | 32 |
| 3.7 | Water phase pressure distribution after 0 (left) and 4 (right) days | 32 |
| 3.8 | Oil phase pressure distribution after 0 (left) and 2 (right) days | 33 |
| 3.9 | Water phase saturation distribution after 20 (left) and 2 (right) days | 33 |
| 4.1 | Iteratively coupled implicit pressure explicit concentration (IMPEC) scheme. | 48 |
| 4.2 | Gas saturation profile after 500 days using TPFA (left) and MFMFE (right) discretizations. | 52 |
| 4.3 | Component concentrations along the injector-producer line after 500 days for MFMFE (solid line) and TPFA (circles) schemes | 53 |
| 4.4 | Oil saturation profiles after 50 days for MFMFE (left) and TPFA (right) discretizations. | 54 |
| 4.5 | Permeability field (left) and gas saturation profiles after 3000 days for MFMFE (middle) and TPFA (right) discretizations. . | 55 |
| 4.6 | Concentration profiles for lightest (C_1) and heaviest (C_{20}) components after 1000 days. | 56 |
| 4.7 | Saturation profiles for gas (left) and oil (right) phases after 1000 days. | 57 |
| 4.8 | Brugge field geometry with well locations. | 58 |

| | | |
|------|---|-----|
| 4.9 | Water, oil and gas relative permeabilities. | 59 |
| 4.10 | Capillary pressure curves. | 59 |
| 4.11 | X (left) and Y (right) direction permeability fields. | 59 |
| 4.12 | Z direction permeability (left) and porosity (right) fields. | 60 |
| 4.13 | Oil and gas saturation profiles after 1000 days. | 60 |
| 4.14 | Pressure and concentration profiles after 1000 days. | 60 |
| | | |
| 5.1 | Oil and water phase relative permeability curves for reservoir and fracture. | 67 |
| 5.2 | Saturation profiles for averaging, meshed-in and interface approaches (left to right) for time $t = 0, 50$ and 100 days (top to bottom). | 69 |
| 5.3 | Schematic of a fractured reservoir flow model. | 70 |
| 5.4 | Fixed stress flow and mechanics coupling. | 77 |
| 5.5 | Iteratively coupled IMPES scheme | 78 |
| 5.6 | Iteratively coupled reservoir and fracture pressure solve | 79 |
| 5.7 | Coupling pressure and velocity degrees for a corner point | 89 |
| 5.8 | Rock matrix capillary pressure curve | 95 |
| 5.9 | Rock matrix relative permeability curve | 96 |
| 5.10 | Fracture relative permeability curve | 97 |
| 5.11 | Experimental saturation profiles from Karpyn (2005) using digital radiography at different times | 97 |
| 5.12 | Numerical saturation profiles (left to right) | 98 |
| 5.13 | Saturation profiles at $t = 1, 100, 150$ and 200 days (left to right). | 99 |
| 5.14 | Schematic of a three-stage hydraulic fracture connected to a well-bore. | 100 |
| 5.15 | Pressure (top) and saturation (bottom) profiles at $t = 1, 2$ and 6 days (from left to right). | 101 |
| 5.16 | Problem description. | 102 |
| 5.17 | Stress magnitude (contour, psi) and principal stress direction (vector) for a single fracture injection case for $t = 0.02, 0.2, 2.0$ days(top row, from left to right) and $t = 3.7, 6.4$ and 20 days (bottom row, from left to right). | 103 |
| 5.18 | Stress magnitude (contour, psi) and principal stress direction (vector) for a single fracture production case for $t = 0.02, 0.1, 6.0$ days (top row, left to right) and $t = 2.5, 7.5$ and 20 days (bottom row, left to right). | 104 |

| | | |
|------|---|-----|
| 5.19 | Frio field case with discrete fractures (shaded orange). | 105 |
| 5.20 | Pressure (left) and saturation (right) profiles after 2.2 years. . . | 106 |
| 6.1 | Evolution of two pressurized fractures: first joining, then non-planar growth and finally branching in heterogeneous porous media. | 114 |
| 6.2 | Problem description. | 116 |
| 6.3 | Determination of crack shape using threshold of the phase field variable to determine fracture cells (marked red). The phase-field module uses locally-refined grids with hanging nodes, which allows to reduce the computational cost significantly. | 126 |
| 6.4 | Reconstructing the fracture geometry. | 126 |
| 6.5 | Work-flow for reconstructing 3D fracture geometry from 2D information. | 127 |
| 6.6 | Integrating fractures generated by phase field model as a fractured well model. | 129 |
| 6.7 | Crack pattern for simultaneous propagation of two penny-shaped fractures at $T = 0, 15$ and 25 seconds in 3D domain. | 133 |
| 6.8 | Crack pattern for simultaneous propagation of two fractures at $T = 0, 20$ and 30 seconds in a 2D domain. | 133 |
| 6.9 | Transient pressure at the center of the fractures for 3D case. . . | 134 |
| 6.10 | Transient pressure at the center of the fractures for 2D case. . . | 135 |
| 6.11 | Crack pattern for simultaneous propagation of two fractures, with larger spacing, at $T = 0, 20$ and 30 seconds. | 136 |
| 6.12 | Crack pattern for sequential hydraulic fracturing at $T = 0, 20$ and 40 seconds. | 137 |
| 6.13 | Stress field for sequential hydraulic fracturing at $T = 0, 20$ and 40 seconds. | 137 |
| 6.14 | Initial crack pattern (left), randomly distributed Lamé coefficients (middle) and non-constant permeability (right). In the two latter figures, red denotes high values and blue/green low values. | 138 |
| 6.15 | Crack pattern for fracture propagation in a heterogeneous medium at $T = 20, 30, 50$ seconds. | 138 |
| 6.16 | Crack pattern for fracture propagation in a heterogeneous medium and non-constant permeability at $T = 5, 10$ and 15 seconds. . . | 138 |
| 6.17 | Example 3, Test 1, crack pattern at $T = 0, 20, 30, 50$ | 139 |

| | | |
|------|--|-----|
| 6.18 | Example 3, Test 2, stress distribution at $T = 0, 20, 30, 50$ | 140 |
| 6.19 | Example 3, Test 2, crack pattern at $T = 0, 20, 30, 50$ | 141 |
| 6.20 | Example 3, Test 2, stress distribution at $T = 0, 20, 30, 50$ | 141 |
| 6.21 | Example 3, Test 3, crack pattern at $T = 0, 20, 30, 50$ | 142 |
| 6.22 | Example 3, Test 3, stress distribution at $T = 0, 20, 30, 50$ | 142 |
| 6.23 | Coarse fracture mesh after adaptation. | 143 |
| 6.24 | Brugge field geometry with fractured injection wells. | 144 |
| 6.25 | Original Brugge field with injection and production wells. . . . | 145 |
| 6.26 | X (left) and Y (right) direction permeability fields. | 146 |
| 6.27 | Z direction permeability (left) and porosity (right) fields. . . . | 146 |
| 6.28 | Pressure profiles after 1000 days for fractured (left) and original (right) Brugge field cases. | 147 |
| 6.29 | Saturation profiles after 1000 days for fractured (left) and orig- inal (right) Brugge field cases. | 147 |
| A.1 | Vertical, horizontal and deviated well (left to right) | 154 |
| A.2 | Elements containing vertical well in a discretized reservoir | 156 |
| A.3 | Calculation of pressure distribution for rate specified vertical wells | 159 |

Chapter 1

Introduction

This chapter presents a problem statement broadly outlining the challenges and motivation guiding the research direction. A list of research objectives and a brief description of the following chapters is also presented to give an overview of the work presented here.

1.1 Problem Statement

Tight and shale formations play a pivotal role in strengthening our energy security and meeting an ever increasing future energy demand. These formations are usually characterized by high pore volumes and low permeabilities making it challenging to recover oil and gas using conventional techniques. Another characteristic feature of such formations is the presence of natural or discrete fractures which are low pore volume and high permeability entities. A formation volume can then be thought of as reservoir storage capacity or hydrocarbons in place and the natural fracture network as reservoir flow capacity.

Hydraulic fracturing is a well known production stimulation technology which lets us access this network by creating artificial fractures extending from

a well-bore into the reservoir. The overall process can be broadly subdivided into three stages: (1) perforation, (2) pressurized fluid injection and (3) proppant distribution. In layman's terms, a ballistic device is first used to perforate well-bore casing and initiate a fracture. The next stage involves injection of water at high pressures with chemical additives for various purposes. The slick water injection is followed by polymer injection with suspended solids called proppants. Once the fluid injection is stopped the solids redistribute and prop the rock matrix from closing while providing the artificial fracture an aperture (opening). This allows a high flow capacity channel extending from the well bore to either the porous reservoir rock matrix or an existing natural fracture network.

The development of an effective toolset for fractured reservoir planning and management is a requirement. This entails accurate modeling of the involved processes beginning from hydraulic fracture propagation and proppant placement followed by long term hydrocarbon recovery predictions from the fracture reservoir system. Inherent in the latter is the prediction and isolation of possible failure zones owing to stress changes associated reservoir depletion or pressurization. One of the challenges is the integration of various complex sub-processes under a single framework. It is therefore necessary to develop detailed mathematical models, representative of the underlying physics, efficient and robust numerical solution approaches along with consistent schemes for coupling these sub-processes.

1.2 Research Objectives

The goal of this research is to develop and integrate models, for field-scale fractured-reservoir recovery predictions, consistently under a single framework and to this end the work can be divided into three phases:

1. **Phase I:** Extension of a multipoint flux mixed finite element (MFME) discretization with general hexahedral elements to span from single and two phase, incompressible and slightly compressible flow to an equation of state (EOS) compositional flow. The general hexahedral grids allow complex reservoir and non-planar fracture geometries to be captured without requiring substantial manipulation of petrophysical properties associated with the reservoir.
2. **Phase II:** Development of a coupled fractured reservoir flow and geomechanics model, solution algorithm and a convergent numerical solution scheme. This entails capturing the differences in fracture and reservoir flow physics and petrophysical properties such as capillary pressure and permeability. Further, address differences between hydraulic and natural fractures by integrating the former with horizontal/deviated well-bore models.
3. **Phase III:** Coupling of a phase field fracture propagation model with a field-scale, coupled, fractured-reservoir flow and geomechanics model. Identify and develop a coupling scheme that takes into account the differences in time scales associated with each of the above physical model.

1.3 Thesis Outline

In the second chapter, we begin by describing a single phase slightly compressible flow model using an MFME scheme. A description of finite element spaces and quadrature rules associated with the scheme are presented once to make the reader familiar with the subject matter. The MFME scheme is locally mass conservative and provides accurate fluxes at the cell faces. Further the additional flux degrees of freedom due to an enhanced BDDF₁ (Brezzi Douglas Durán Fortin, Brezzi et al. (1987)) space allows treatment of a full tensor permeability. This provides avenues for several developments in the following chapters.

The second chapter discusses a slightly compressible two phase flow model using the spatial discretization scheme presented in the previous chapter. Two different formulations, namely formulation I and II, with different primary unknowns are presented. A detailed description of each solution is discussed differing in degree of implicit treatment of the primary unknowns associate with each of the two formulations. An implicit pressure explicit saturation and implicit pressure explicit concentration scheme is used for formulations I and II, respectively. The differences in the two formulations suggest that the first one is more appropriate for multiphase flow systems where phase densities are not affected by phase or component concentrations. The second formulation is later used for equation of state compositional flow modeling in the next chapter.

In the third chapter, we present an equation of state (EOS) composi-

tional flow model where the model formulation is adapted to use the aforementioned MFME scheme. An implicit pressure explicit concentration (IMPEC) solution approach is employed. The chapter also briefly discusses a variant of successive substitution phase behavior and stability algorithm along with the associate mathematical description. A comparison between MFME and two-point flux approximation (TPFA) scheme shows that a full tensor permeability is capable of accounting for grid-orientation effects. A number of other numerical tests including Frio and Brugge field gas flooding is also presented.

The fourth chapter describes a coupled two-phase fractured reservoir flow and geomechanics model with different capillary pressure curves in the reservoir and fractures. The differences in flow physics are captured using a Reynold's lubrication equation and Darcy's law inside the fracture and the reservoir, respectively. The two domains are again discretized using the MFME scheme. Here the general hexahedral grids allow us to capture non-planar fracture geometries. A solution algorithm is described along with two numerical schemes owing to differences in the treatment of jump in fluxes across the fracture or the leakage term. The results section presents a comparison between numerical and experimental results for a fracture core along with several other numerical tests and field scale examples.

In the fifth chapter, we present a coupled phase field fracture propagation model and fractured reservoir flow model. We begin with a brief description of the phase field fracture propagation model. An explicit coupling scheme is chosen based upon differences in time-scales associated with fracture

propagation and coupled reservoir-fracture flow modeling and the physically discrete nature of the two physical processes. A workflow for reconstructing 2D and 3D fracture information and later integrating into the coupled fracture reservoir flow model is described. The results section shows several numerical tests studying effect of fracture spacing, reservoir heterogeneities, initial fracture lengths. A Brugge field case demonstrating the aforementioned coupling approach is also presented.

The seventh chapter provides conclusions of the research presented here and a brief outlook towards future work and improvements. A brief literature survey pertaining to each of the research areas pursued as a part of this work is presented at the beginning of corresponding chapter.

Chapter 2

Single Phase Flow

In this chapter, we begin by describing a single phase slightly compressible flow model formulation. This is followed by a weak formulation of the model with a brief description of finite element spaces and quadrature rules associated with the spatial discretization scheme employed here. A fully discrete formulation is then presented where a backward Euler scheme is used for temporal discretization whereas a multipoint flux mixed finite element (MFME) method is used for spatial discretization. Finally the linearized system and a discussion reduction to cell-centered stencil resulting from local elimination of fluxes from the linear system is presented.

2.1 Model Formulation

This section describes a single phase slightly compressible flow model. The mass conservation equation for single phase flow in porous medium on a domain $\Omega \in \mathbb{R}^3$ is written as,

$$\frac{\partial(\phi\rho)}{\partial t} + \nabla \cdot z = q \text{ in } \Omega \times (0, T], \quad (2.1)$$

where ϕ , ρ and q are the rock matrix porosity, density and source term, respectively. The flux z is given by the Darcy's law as,

$$z = -K \frac{\rho}{\nu} \nabla (p - \rho g \nabla d) \text{ in } \Omega. \quad (2.2)$$

Here, ν is the fluid viscosity.

2.1.1 Boundary & Initial Conditions

The Neumann and Dirichlet boundary conditions are prescribed as,

$$z \cdot n = z^N \text{ on } \partial\Omega^N \times (0, T], \quad (2.3)$$

$$p = p^D \text{ on } \partial\Omega^D \times (0, T], \quad (2.4)$$

along with an initial condition of,

$$p = p(0) \text{ in } \Omega \quad (2.5)$$

Here, n is the unit normal to the boundary $\partial\Omega$

2.1.2 Closure and Other Conditions

We further assume a slightly compressible flow for which the equation of state is given by,

$$\rho = \rho_0 \exp [c_f (p - p_{0,SC})]. \quad (2.6)$$

Here, c_f is the fluid compressibility and $p_{0,SC}$ is the pressure at standard conditions. The porosity varies linearly with pressure, given by Eqn. (3.16), with rock compressibility (c_r) as the constant of proportionality and ϕ_0 as the reference porosity.

$$\phi = \phi_0 [1 + c_r (p - p_{0,SC})] \quad (2.7)$$

2.2 Weak Formulation

We use a multipoint flux mixed finite element method (MFMFE) to construct a fully discrete form of the flow problem describe earlier. MFMFE methods have been developed by Wheeler and Yotov (2006) for quadrilateral and simplicial grids and were later extended to general hexahedral grids by Ingram et al. (2010). Mixed finite element (MFE) methods are preferred over other variational formulations due to their local mass conservation and improved flux approximation properties. An appropriate choice of mixed finite element spaces and degrees of freedom based upon the quadrature rule for numerical integration (Wheeler et al. (2011a); Wheeler and Xue (2011)) allows flux degrees of freedoms to be defined in terms of cell-centered pressures.

2.2.1 Finite element spaces

For the sake of document completeness we briefly discuss the appropriate finite element spaces used to formulate the MFMFE scheme. We recall the finite dimensional spaces and the reduction to cell-centered pressure scheme introduced by Wheeler and Yotov (2006); Ingram et al. (2010); Wheeler et al. (2011a); Wheeler and Xue (2011). Rewriting the problem defined by Eqns. (2.1)-(2.4) in the mixed form leads to a natural choice of spaces for velocity and pressure variables, namely $V = \{v \in H(\text{div}; \Omega) : v \cdot n = 0 \text{ on } \partial\Omega^N\}$, and $W = L^2(\Omega)$, respectively. Let $V_h \times W_h$ be the lowest order BDDF₁ mixed finite element spaces defined on a hexahedra Brezzi et al. (1985, 1987). The linear functions provide three degrees of freedom per face which are chosen to

be the normal component of velocities at the faces. On a reference unit cube these spaces are defined as,

$$\begin{aligned}
BDDF_1(\hat{E}) &= P_1(\hat{E})^3 + r_0 \text{curl}(0, 0, \hat{x}\hat{y}\hat{z})^T + r_1 \text{curl}(0, 0, \hat{x}\hat{y}^2)^T + s_0 \text{curl}(\hat{x}\hat{y}\hat{z}, 0, 0)^T \\
&\quad + s_1 \text{curl}(\hat{y}\hat{z}^2, 0, 0)^T + t_0 \text{curl}(0, \hat{x}\hat{y}\hat{z}, 0)^T + t_1 \text{curl}(0, \hat{x}^2\hat{z}, 0)^T \\
&= P_1(\hat{E})^3 + r_0(\hat{x}\hat{z}, -\hat{y}\hat{z}, 0)^T + r_1(2\hat{x}\hat{y}, -\hat{y}^2, 0)^T + s_0(0, \hat{x}\hat{y}, -\hat{x}\hat{z})^T + \\
&\quad s_1(0, 2\hat{y}\hat{z}, -\hat{z}^2)^T + t_0(-\hat{x}\hat{y}, 0, \hat{y}\hat{z})^T + t_1(-\hat{x}^2, 0, 2\hat{x}\hat{z})^T
\end{aligned} \tag{2.8}$$

$$\hat{W}(\hat{E}) = P_0(\hat{E}) \tag{2.9}$$

Let \mathcal{T}_h be a finite element partition of Ω comprising of hexahedral elements. The mixed finite element spaces on a physical element is mapped from a reference element using the Piola and scalar transformations (2.10).

$$\begin{aligned}
v \leftrightarrow \hat{v} : \hat{v} &= \frac{1}{J_E} DF_E \hat{v} \circ F_E^{-1} \\
w \leftrightarrow \hat{w} : w &= \hat{w} \circ F_E^{-1}
\end{aligned} \tag{2.10}$$

where F_E denotes the trilinear mapping from the reference element \hat{E} to the physical element E where DF_E is the Jacobian matrix and $J_E = |\det DF_E|$. Note that we have used the Piola transformation for the velocity space which preserves the normal traces. The discrete finite element spaces V_h and W_h on \mathcal{T}_h are given by,

$$\begin{aligned}
V_h &\equiv \{v \in V : v|_E \leftrightarrow \hat{v}, \hat{v} \in \hat{V}(\hat{E}), \forall E \in \mathcal{T}_h\}, \\
W_h &\equiv \{w \in W : w|_E \leftrightarrow \hat{w}, \hat{w} \in \hat{W}(\hat{E}), \forall E \in \mathcal{T}_h\},
\end{aligned} \tag{2.11}$$

An enhanced $BDDF_1$ mixed finite element space on \hat{E} , with one additional degree of freedom per face resulting in bilinear functions, for a general hexahedral element is defined on a reference unit cube Eqn.(2.12) by enhancing

the BDDF₁ space Eqn.(2.8).

$$\begin{aligned}
\hat{V}^*(\hat{E}) &= BDDF_1(\hat{E}) + r_2 \text{curl}(0, 0, \hat{x}^2 \hat{z})^T + r_3 \text{curl}(0, 0, \hat{x}^2 \hat{y} \hat{z})^T + s_2 \text{curl}(\hat{x} \hat{y}^2, 0, 0)^T \\
&\quad + s_3 \text{curl}(\hat{x} \hat{y}^2 \hat{z}, 0, 0)^T + t_2 \text{curl}(0, \hat{y} \hat{z}^2, 0)^T + t_3 \text{curl}(0, \hat{x}^2 \hat{z}, 0)^T \\
&= BDDF_1(\hat{E}) + r_2(0, -2\hat{x} \hat{z}, 0)^T + r_3(\hat{x}^2 \hat{z}, -2\hat{x} \hat{y} \hat{z}, 0)^T + s_2(0, 0, -2\hat{x} \hat{y})^T \\
&\quad + s_3(0, \hat{x} \hat{y}^2, -2\hat{x} \hat{y} \hat{z})^T + t_2(-2\hat{y} \hat{z}, 0, 0)^T + t_3(-2\hat{x} \hat{y} \hat{z}, 0, \hat{y} \hat{z}^2)
\end{aligned} \tag{2.12}$$

2.2.2 Quadrature Rules

In this section, we discuss quadrature rules the numerical integration of the velocity mass matrix. For $q, v \in V_h^*$ the local (on element E) and global (on domain Ω) quadrature rules are given by Eqns.(2.14)-(2.13) and Eqn.(2.15), respectively. Here Eqns.(2.13) and (2.14) give the symmetric and non-symmetric quadrature rules, respectively. The non-symmetric quadrature rule has been shown to have convergence properties for general hexahedra by Wheeler et al. (2011b).

$$(K^{-1}z, v)_{Q,E} = \frac{1}{8} \sum_{i=1}^8 J_E(\hat{r}_i) (DF_E^{-1})^T(r_i) DF_E^T(r_i) K_E^{-1}(F_E(\hat{r}_i)) q(r_i) \cdot v(r_i) \tag{2.13}$$

$$(K^{-1}z, v)_{Q,E} = \frac{1}{8} \sum_{i=1}^8 J_E(\hat{r}_i) (DF_E^{-1})^T(r_i) DF_E^T(\hat{r}_{c,\hat{E}}) \bar{K}_E^{-1} q(r_i) \cdot v(r_i) \tag{2.14}$$

$$(K^{-1}z, v)_Q \equiv \sum_{E \in \mathcal{T}_h} (K^{-1}q, v)_{Q,E} \equiv \sum_{E \in \mathcal{T}_h} \frac{|\hat{E}|}{8} \sum_{i=1}^8 \mathcal{K}^{-1}(\hat{r}_i) \hat{q}(\hat{r}_i) \cdot \hat{v}(\hat{r}_i) \tag{2.15}$$

Here, \hat{r}_i is a vertex of the reference element \hat{E} , $\hat{r}_{c,\hat{E}}$ is the center of mass of \hat{E} , \bar{K}_E is the mean of K on E .

2.2.3 Fully Discrete Formulation

In this section, we present a fully discrete formulation of the model described before. An MFMFE and backward Euler schemes are used for spatial and temporal discretizations, respectively. For simplicity we assume Dirichlet and no-flow boundary conditions. The discrete weak problem reads: Given $p_h^n \in W_h$, find $z_h \in V_h$ and $p_h \in W_h$ such that,

$$\left\langle \frac{\nu}{\rho} K^{-1} z_h, v_h \right\rangle_{Q,E} - (p_h, \nabla \cdot v_h)_E = (\rho g \nabla d, v_h)_E - \int_{\partial E \cap \partial \Omega} p v_h \cdot n \quad \forall v_h \in V_h, \quad (2.16)$$

$$\left(\frac{(\phi \rho)^{n+1} - (\phi \rho)^n}{\Delta t}, w_h \right)_E + (\nabla \cdot z_h, w_h)_E = (q, w_h)_E \quad \forall w_h \in W_h. \quad (2.17)$$

Here, the superscript n represents the time level iterate. We use one of the two quadrature rules described in the previous section to perform numerical integration. Please note that in the above all terms are evaluated at time level ‘ $n+1$ ’ unless explicitly stated otherwise.

2.3 Linearization

The resulting system of equations is solved implicitly in z_h and p_h using an inexact Newton method. We begin by linearizing the discrete weak formulation to obtain a linear system of equations in the unknowns δz_h and δp_h with superscript ‘ k ’ representing the Newton iterate.

$$\left\langle \frac{\nu}{\rho^k} K^{-1} \delta z_h^k, v_h \right\rangle_{Q,E} = (\delta p_h^k, \nabla \cdot v_h)_E - \left\{ \left\langle \frac{\nu}{\rho^k} K^{-1} z_h^k, v_h \right\rangle_{Q,E} - (p_h^k, \nabla \cdot v_h)_E - (\rho^k g \nabla d, v_h)_E + \int_{\partial E} p v_h \cdot n \right\} \quad (2.18)$$

$$\begin{aligned} ((c_r \phi_0 \rho + \phi c_f)^{n+1,k} \delta p_h^k, w_h)_E + (\Delta t \nabla \cdot \delta z_h^k, w_h)_E = & - \left\{ ((\phi \rho)^{n+1,k} - (\phi \rho)^n, w_h)_E \right. \\ & + (\Delta t \nabla \cdot z_h^k, w_h)_E \\ & \left. - (\Delta t q^k, w_h)_E \right\} \end{aligned} \quad (2.19)$$

2.3.1 Reduction to a Cell-Centered Stencil

Ingram et al. (2010) described the process of eliminating velocity degrees of freedom resulting in a cell centered pressure system for an MFMFE scheme. In this section we follow the same procedure for a non-linear system. The four velocity degrees of freedom at a face \hat{e} on the reference element \hat{E} are chosen to be normal component of velocities at the vertices of \hat{e} . Thus there are three degrees of freedom associated with each corner \hat{r}_i , $i = 1, \dots, 8$. Let \hat{v}_{ij} , $j = 1, 2, 3$ be the basis functions associate with \hat{r}_i . The quadrature rule, given by Eqn. (2.15), then couples the three basis functions associated with the corner-point such that,

$$\begin{aligned} (\mathcal{K}^{-1} \hat{v}_{11}, \hat{v}_{11})_{\hat{Q}, \hat{E}} &= \frac{\mathcal{K}_{11}^{-1}(\hat{r}_1)}{8}, & (\mathcal{K}^{-1} \hat{v}_{11}, \hat{v}_{12})_{\hat{Q}, \hat{E}} &= \frac{\mathcal{K}_{21}^{-1}(\hat{r}_1)}{8}, \\ (\mathcal{K}^{-1} \hat{v}_{11}, \hat{v}_{13})_{\hat{Q}, \hat{E}} &= \frac{\mathcal{K}_{31}^{-1}(\hat{r}_1)}{8}, & (\mathcal{K}^{-1} \hat{v}_{11}, \hat{v}_{ij})_{\hat{Q}, \hat{E}} &= 0 \quad \forall ij \neq 11, 12, 13. \end{aligned} \quad (2.20)$$

Thus, taking $v = v_1$ in Eqn. (2.18) results in coupling of δz_1 with δz_5 , δz_8 , δz_9 and δz_{12} .

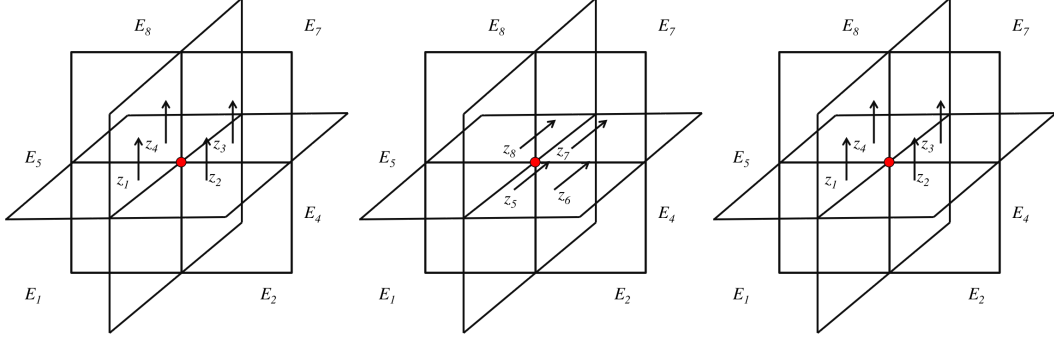


Figure 2.1: Velocity degrees of freedom associated with the corner marked red along x (left), y (middle) and z (right) directions

We can form a local linear system of equations, corresponding to a corner point, in $\delta z_1, \dots, \delta z_{12}$ by taking $v = v_1, \dots, v_{12}$. An interior corner-point is surrounded by eight elements E_1, \dots, E_8 and twelve faces e_1, \dots, e_{12} with normal velocity components z_1, \dots, z_{12} in x, y and z directions as shown in Fig. 2.1. For example, if we take $v = v_9$ then the left hand side of Eqn. (2.18) can be written as,

$$\left(K^{-1} \frac{\nu}{\rho} \delta z_h, v_9 \right)_{Q,E} = \left(K^{-1} \frac{\nu}{\rho} \delta z_h, v_9 \right)_{Q,E_1} + \left(K^{-1} \frac{\nu}{\rho} \delta z_h, v_9 \right)_{Q,E_2}. \quad (2.21)$$

Using Eqn. (2.15) the first and second terms on the right hand side of Eqn. (2.21) can be expanded as,

$$\left(K^{-1} \frac{\nu}{\rho} \delta z_h, v_9 \right)_{Q,E_1} = \frac{1}{8} \left(\mathcal{K}_{11,E_1}^{-1} \frac{\nu}{\rho_{e_9}} |e_9| \delta z_9 + \mathcal{K}_{12,E_1}^{-1} \frac{\nu}{\rho_{e_5}} |e_5| \delta z_5 + \mathcal{K}_{13,E_1}^{-1} \frac{\nu}{\rho_{e_1}} |e_1| \delta z_1 \right) |e_9|, \quad (2.22)$$

$$\left(K^{-1} \frac{\nu}{\rho} \delta z_h, v_9 \right)_{Q, E_2} = \frac{1}{8} \left(\mathcal{K}_{11, E_2}^{-1} \frac{\nu}{\rho_{e_9}} |e_9| \delta z_9 + \mathcal{K}_{12, E_2}^{-1} \frac{\nu}{\rho_{e_6}} |e_6| \delta z_6 + \mathcal{K}_{13, E_2}^{-1} \frac{\nu}{\rho_{e_2}} |e_2| \delta z_2 \right) |e_9|. \quad (2.23)$$

The right hand side of Eqn. (2.18) can be written as,

$$(\delta p_h, \nabla \cdot v_9) = (\delta p_h, \nabla \cdot v_9)_{E_1} + (\delta p_h, \nabla \cdot v_9)_{E_2} = \frac{1}{4} (\delta p_1 - \delta p_2) |e_9|, \quad (2.24)$$

where p_1, \dots, p_8 are the cell centered pressures corresponding to elements E_1, \dots, E_8 shown in Fig. 2.1 Using Eqns. (2.21)-(2.24) in Eqn. (2.18),

$$\left\{ \frac{\nu}{\rho_{e_9}} \left(\frac{1}{2} \mathcal{K}_{11, E_1}^{-1} + \frac{1}{2} \mathcal{K}_{11, E_2}^{-1} \right) |e_9| \delta z_9 + \frac{\nu}{2\rho_{e_5}} \mathcal{K}_{12, E_1}^{-1} |e_5| \delta z_5 + \frac{1}{2\rho_{e_6}} \mathcal{K}_{12, E_2}^{-1} |e_6| \delta z_6 \right. \\ \left. + \frac{\nu}{2\rho_{e_1}} \mathcal{K}_{13, E_1}^{-1} |e_1| \delta z_1 + \frac{\nu}{2\rho_{e_2}} \mathcal{K}_{13, E_2}^{-1} |e_2| \delta z_2 \right\} = \delta p_1 - \delta p_2. \quad (2.25)$$

Here $\rho_{e_1}, \dots, \rho_{e_9}, \dots, \rho_{e_{12}}$ are the fluid densities on faces $e_1, \dots, e_9, \dots, e_{12}$ approximated as an average density. For example,

$$\rho_{e_9} = \frac{\rho_{E_1} + \rho_{E_2}}{2} = \frac{\rho_{p_1} + \rho_{p_2}}{2}. \quad (2.26)$$

We can similarly write 11 more equations using remaining v_j s ($j \neq 9$) thus forming a total of 12 linear equations in unknowns $\delta z_1, \dots, \delta z_{12}$ and $\delta p_1, \dots, \delta p_8$. Thus δz can be expressed in terms of cell-centered δp using these 12 linear equations. Fig. 2.2 shows the coupling of velocity and pressure degrees of freedom around a corner point. The saddle point system from Eqns. (2.18) and (2.19) can be written as,

$$\begin{pmatrix} A & -B \\ B^T & C \end{pmatrix} \begin{pmatrix} \delta z_h \\ \delta p_h \end{pmatrix} = \begin{pmatrix} -\mathbf{R}_1 \\ -\mathbf{R}_2 \end{pmatrix}. \quad (2.27)$$

$$R_1 = \left\{ \left\langle \frac{\nu}{\rho^k} K^{-1} z_h^k, v_h \right\rangle_{Q,E} - (p_h^k, \nabla \cdot v_h)_E - (\rho^k g \nabla d, v_h)_E + \int_{\partial E} p v_h \cdot n \right\}, \quad (2.28)$$

$$R_2 = \left\{ ((\phi \rho)^{n+1,k} - (\phi \rho)^n, w_h)_E + (\Delta t \nabla \cdot z_h^k, w_h)_E - (\Delta t q^k, w_h)_E \right\}. \quad (2.29)$$

A cell-centered pressure stencil is obtained by substituting the above ex-

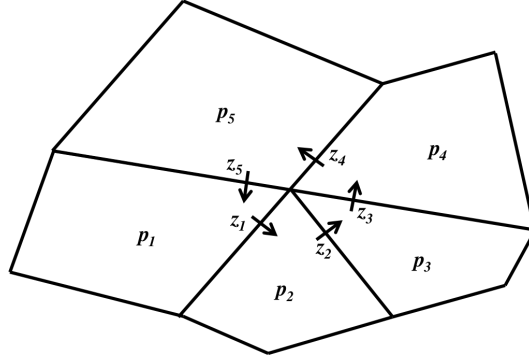


Figure 2.2: Coupling velocity and pressure degrees of freedom corresponding to a vertex

pressions in the mass conservation equation (Eqn. (2.19)). For a logically rectangular grid it can be shown that this results in a 27 point and 9 point pressure stencils for 3D and 2D cases, respectively. The matrix A is positive definite and therefore invertible for the symmetric quadrature rule. The same hold true for the non-symmetric quadrature rule with mild restrictions on the regularity of the grid and/or permeability anisotropy (Wheeler et al. (2011b)). Eliminating fluxes δz_h from Eqn. (2.27) result in a cell-centered system for δp_h with a symmetric positive definite matrix $B^T A^{-1} B$.

$$(B^T A^{-1} B + C) \delta p_h^k = B^T A^{-1} R_1 - R_2. \quad (2.30)$$

This linear system of equations is then solved to obtain an updated pressure following a Newton step given by,

$$p_h^{k+1} = p_h^k + \delta p_h^k. \quad (2.31)$$

The MFME scheme presented here will be used for spatial discretization of degenerate parabolic equations corresponding to phase or component mass conservation in the following chapters. As will be seen, the general hexahedral elements allow complex geometries to be captured with ease without requiring substantial changes in the associated petrophysical properties. Further the multipoint flux feature utilizes a full permeability tensor as opposed to the diagonal tensor for two-point flux approximation scheme. The front at the injected and displaced fluids contact is therefore captured more accurately.

Chapter 3

Two-phase Flow

In this chapter, we use the MFME scheme discussed in the previous chapter to a two phase flow problem. A treatment of capillary pressure and relative permeabilities in the mixed methods framework is presented. In order to avoid inverting zero mobility values at the relative permeability end-points either a total mass conservation approach (Hoteit and Firoozabadi (2008b)) or an expanded mixed finite element method (Arbogast et al. (1997)) is used. Two different model formulations are discussed for solving this problem. This is used to develop an understanding of the applicability of the two model formulations to different two-phase flow systems.

We begin by describing a slightly compressible, two-phase flow problem in porous media. The constitutive equation relating phase fluxes z_β to phase pressures p_β given by a multiphase Darcy's law (3.1).

$$z_\beta = -K \rho_\beta \frac{k_{r\beta}}{\nu_\beta} (\nabla p_\beta - \rho_\beta g \nabla D) \text{ in } \Omega \quad (3.1)$$

Here $\beta = w$ or o representing water (wetting) and oil (non-wetting) phases, respectively.

3.1 Formulation I

The primary unknowns are chosen to be p_w and S_w to simplify the model description with water as the reference phase. However either choice of p_β and S_β can be chosen as the primary unknowns and a similar treatment as presented below will apply. The phase mass conservation equations are given by Eqn. (3.2).

$$\frac{\partial(\phi\rho_\beta S_\beta)}{\partial t} + \nabla \cdot (z_\beta) = q_\beta \text{ in } \Omega \times (0, T] \quad (3.2)$$

Here, q_β represents a source or sink term and is evaluated using a well model. The reader is referred to Appendix A for details regarding well bore modeling approaches followed in this work. Summing the mass conservation equation, over all the phases β , (3.2) leads to a total mass conservation equation,

$$\frac{\partial\left(\phi \sum_{\beta} \rho_{\beta} S_{\beta}\right)}{\partial t} + \nabla \cdot (z_t) = q_t \text{ in } \Omega \times (0, T], \quad (3.3)$$

with the total phase mass flux given by,

$$z_t = -K \sum_{\beta} \left(\rho_{\beta} \frac{k_{r\beta}}{\nu_{\beta}} (\nabla p_{\beta} - \rho_{\beta} g \nabla D) \text{ in } \Omega \right), \quad (3.4)$$

and the total point source/sink term by,

$$q_t = \sum_{\beta} q_{\beta} \quad (3.5)$$

3.1.1 Boundary & Initial Conditions

Here we discuss boundary and initial conditions pertinent to two-phase flow system. For the sake of brevity we restrict ourselves to only two types

of boundary conditions: (1) no-flow ($\partial\Omega^N$) and (2) Dirichlet ($\partial\Omega^D$) boundary conditions with $\partial\Omega^N \cup \partial\Omega^D = \partial\Omega$. The no-flow boundary condition is given by,

$$z_\beta \cdot n = 0 \text{ for } \beta = w \text{ and } o \text{ on } \partial\Omega^N \times (0, T] \quad (3.6)$$

The Dirichlet boundary condition is,

$$\left. \begin{array}{l} p_w = p_w^D \\ S_w = S_w^D \end{array} \right\} \text{ on } \partial\Omega^D \times (0, T] \quad (3.7)$$

Please note that the choices described here are not restrictive and more general boundary conditions can also be treated. Furthermore initial conditions are,

$$\left. \begin{array}{l} p_w = p_w(0) \\ S_w = S_w(0) \end{array} \right\} \text{ in } \Omega. \quad (3.8)$$

3.2 Formulation II

Let N_β be the concentration of phase β given by,

$$N_\beta = \rho_\beta S_\beta. \quad (3.9)$$

A different formulation is obtained by choosing p_w and N_β as the primary unknowns. The phase mass conservation equation can then be written as,

$$\frac{\partial(\phi N_\beta)}{\partial t} + \nabla \cdot (z_\beta) = q_\beta \text{ in } \Omega \times (0, T]. \quad (3.10)$$

Please note that there are three unknowns for this systems: p_w , N_o and N_w . As will be seen later in the fully discrete and further linearization sections this results in a more implicit treatment of the unknowns compared to the previous formulation.

3.2.1 Boundary & Initial Conditions

The boundary conditions corresponding to Eqn. (3.13) for the current system is given by,

$$z_\beta \cdot n = 0 \text{ for } \beta = w \text{ and } o \text{ on } \partial\Omega^N \times (0, T], \quad (3.11)$$

$$\left. \begin{array}{l} p_w = p_w^D \\ N_\beta = N_\beta^D \end{array} \right\} \text{ for } \beta = w \text{ and } o \text{ on } \partial\Omega^D \times (0, T]. \quad (3.12)$$

Here, $\partial\Omega^N \cup \partial\Omega^D = \partial\Omega$. Similarly the initial condition is given by,

$$\left. \begin{array}{l} p_w = p_w(0) \\ N_\beta = N_\beta(0) \end{array} \right\} \text{ in } \Omega. \quad (3.13)$$

3.3 Closure & Other Conditions

The capillary pressure is defined as a continuous and monotonic function of S_w ,

$$p_{c\beta} = \begin{cases} 0 & \text{for } \beta = w \\ f(S_w) & \text{for } \beta = o \end{cases}. \quad (3.14)$$

Here $p_{w,SC}$ is the water phase pressure at standard conditions, c_β is the compressibility and $p_{c\beta}$ is the capillary pressure of phase β . Similar to single phase flow, we assume a slightly compressible flow for both wetting and non-wetting phases,

$$\rho_\beta = \rho_{\beta 0} \exp [c_\beta (p_w + p_{c\beta} - p_{c\beta,SC} - p_{w,SC})], \quad (3.15)$$

The value of $p_{c\beta,SC}$ is usually assumed to be zero at standard conditions and its use is therefore curtailed hereafter. The porosity variation with pressure is

given by Eqn. (3.16) where ϕ_0 is the porosity at standard conditions.

$$\phi = \phi_0 [1 + c_r(p_w - p_{w,SC})] \quad (3.16)$$

Further the saturation constraint is given by,

$$S_w + S_o = 1. \quad (3.17)$$

3.4 Fully Discrete Formulation

In this section, we present the fully discrete forms of the two previously described model formulations. An iteratively coupled implicit pressure explicit saturation approach (IMPES) and an implicit pressure explicit concentration (IMPEC) method is used to solve formulations I and II, respectively. Fig. 3.1 shows a schematic of the iteratively coupled IMPES/IMPEC. Similar to

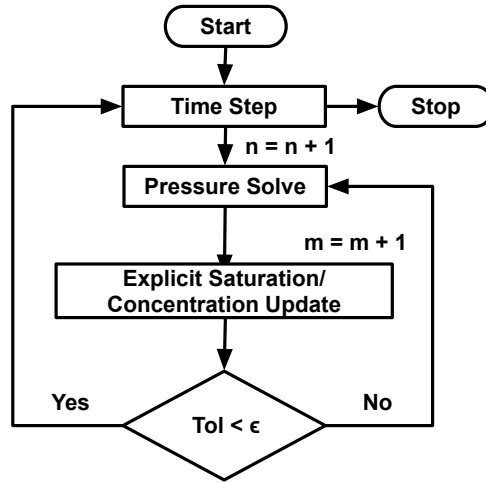


Figure 3.1: Flowchart depicting iteratively coupled IMPES/IMPEC schemes

single phase flow, a backward Euler scheme is used for temporal discretization along with an MFME scheme for spatial discretization of pressure equations. The saturation and concentration equations are time and space discretized using forward Euler and finite volume schemes, respectively. Please note that a discussion on the finite element spaces and quadrature rules associated with the MFME scheme has already been presented in section 2.2. Eqn. (3.3) and (3.2), with $\beta = o, w$ along with the associated Darcy phase fluxes form the pressure and saturation equations, respectively.

3.4.1 Formulation I

Let ‘n’ and ‘m’ be the time and iterative coupling iterates, respectively then the discrete variational problem for the pressure equation reads: Given $S_{w,h}^{m+1,m}, P_{w,h}^n \in W_h, P_{w,h}^{n+1,m} \in W_h$ and $z_{t,h}^{n+1,m} \in V_h$, find $p_{w,h}^{n+1,m+1} \in W_h$ and $z_{t,h}^{n+1,m+1} \in V_h$ such that,

$$\begin{aligned}
& \left\langle \frac{K^{-1}}{\lambda_t^{n+1,\tilde{m}}} z_{t,h}^{n+1,\tilde{m}}, v_h \right\rangle_{Q,E} - (p_{w,h}^{n+1,m+1}, \nabla \cdot v_h)_E \\
& = \left(\left[\frac{\lambda_w}{\lambda_t} \right]^{n+1,\tilde{m}} p_{cw}^{n+1,m}, \nabla \cdot v_h \right)_E + \left(\sum_{\beta} \left[\frac{\lambda_{\beta}}{\lambda_t} \right]^{n+1,\tilde{m}} \rho_{\beta}^{n+1,m+1} g \nabla d, v_h \right)_E \\
& - \int_{\partial E \cap \partial \Omega} \left[\frac{\lambda_w}{\lambda_t} \right]^{n+1,\tilde{m}} p_{cw} v_h \cdot n - \int_{\partial E \cap \partial \Omega} p_{w,h} v_h \cdot n \quad \forall v_h \in V_h.
\end{aligned} \tag{3.18}$$

$$\begin{aligned}
& \left(\sum_{\beta} \frac{\phi^{n+1,m+1} \rho_{\beta}^{n+1,m+1} S_{\beta,h}^{n+1,m}}{\Delta t}, w_h \right)_E + \left(\nabla \cdot z_{t,h}^{n+1,\tilde{m}}, w_h \right)_E \\
& = (q_t^{n+1,m}, w_h)_E + \left(\sum_{\beta} \frac{(\phi \rho_{\beta} S_{\beta,h})^n}{\Delta t}, w_h \right)_E \quad \forall w_h \in W_h
\end{aligned} \tag{3.19}$$

The saturation update problem then reads: Given $S_{w,h}^{n+1,m}$, $p_{w,h}^{n+1,m+1} \in W_h$ and $z_{w,h}^{n+1,m+1} \in V_h$, find $S_{w,h}^{n+1,m+1}$ such that,

$$\begin{aligned} & \left(\frac{\phi^{n+1,m+1} \rho_w^{n+1,m+1} S_{w,h}^{n+1,m+1}}{\Delta t}, w_h \right)_E + \left(\nabla \cdot z_{w,h}^{n+1,\tilde{m}}, w_h \right)_E \\ & = (q_w^{n+1,m}, w_h)_E + \left(\frac{(\phi \rho_w S_{w,h})^n}{\Delta t}, w_h \right)_E \quad \forall w_h \in W_h \end{aligned} \quad (3.20)$$

The superscript \tilde{m} describes quantities containing both $p_w^{n+1,m+1}$ and saturation $S_w^{n+1,m}$ where the mobilities λ s are given by,

$$\lambda_t^{n+1,\tilde{m}} = \sum_{\beta} \lambda_{\beta}^{n+1,\tilde{m}} = \sum_{\beta} \rho_{\beta}^{n+1,m+1} \frac{k_{r\beta}^{n+1,m}}{\nu_{\beta}}. \quad (3.21)$$

An updated oil saturation is then obtained from the saturation constraint as,

$$S_{o,h}^{n+1,m+1} = 1 - S_{w,h}^{n+1,m+1}. \quad (3.22)$$

3.4.2 Formulation II

Please note that compared to formulation I, formulation II cannot be classified into pressure and concentration equations as of yet. This serves as another important distinction between the two and would be clarified later in the linearization section. Since relative permeabilities ($k_{r\beta}$) become zero at residual and irreducible saturations an expanded mixed form is employed to avoid inverting zero. An intermediate phase flux (\tilde{z}_{β}) is defined which is related to the phase fluxes as,

$$z_{\beta} = \frac{k_{r\beta} \rho_{\beta}}{\nu_{\beta}} \tilde{z}_{\beta}. \quad (3.23)$$

The discrete, expanded mixed variational problem similar to formulation I reads: Given $N_{\beta,h}^n$, $p_{w,h}^n$, $N_{\beta,h}^{n+1,m}$ and $p_{w,h}^{n+1,m} \in W_h$ and $z_{\beta,h}^{n+1,m} \in V_h$, find $p_{w,h}^{n+1,m+1} \in W_h$ and $z_{\beta,h}^{n+1,m+1} \in V_h$, where $\beta = o, w$, such that,

$$\begin{aligned} \langle K^{-1} \tilde{z}_{\beta,h}^{n+1,m+1}, v_h \rangle_{Q,E} - (p_{w,h}^{n+1,m+1}, \nabla \cdot v_h)_E \\ = (p_{c\beta}^{n+1,m}, \nabla \cdot v_h)_E + (\rho_{\beta}^{n+1,m+1} g \nabla d, v_h)_E \\ - \int_{\partial E \cap \partial \Omega} p_{c\beta} v_h \cdot n - \int_{\partial E \cap \partial \Omega} p_{w,h} v_h \cdot n \quad \forall v_h \in V_h, \end{aligned} \quad (3.24)$$

$$(z_{\beta,h}, v_h)_E = \left(\frac{k_{r\beta} \rho_{\beta}}{\nu_{\beta}} \tilde{z}_{\beta,h}, v_h \right)_E = (\lambda_{\beta} \tilde{z}_{\beta,h}, v_h)_E, \quad (3.25)$$

$$\begin{aligned} \left(\frac{\phi^{n+1,m+1} N_{\beta,h}^{n+1,m+1}}{\Delta t}, w_h \right)_E + (\nabla \cdot z_{\beta,h}^{n+1,m+1}, w_h)_E \\ = (q_t^{n+1,m}, w_h)_E + \left(\frac{(\phi N_{\beta,h})^n}{\Delta t}, w_h \right)_E \quad \forall w_h \in W_h. \end{aligned} \quad (3.26)$$

Similar to the previous formulation the superscript \tilde{m} describe quantities containing both $p_w^{n+1,m+1}$ and $N_{\beta}^{n+1,m}$. Further the saturation constraint can be rewritten as,

$$\frac{N_{o,h}}{\rho_o} + \frac{N_{w,h}}{\rho_w} = 1. \quad (3.27)$$

The explicit concentration update problem is: Given $N_{\beta,h}^{n+1,m}$, $p_{w,h}^{n+1,m+1} \in W_h$ and $z_{\beta,h}^{n+1,\tilde{m}} \in V_h$, find $N_{\beta,h}^{n+1,m+1}$, where $\beta = o, w$, such that:

$$\begin{aligned} \left(\frac{\phi^{n+1,m+1} N_{\beta,h}^{n+1,m+1}}{\Delta t}, w_h \right)_E + (\nabla \cdot z_{\beta,h}^{n+1,\tilde{m}}, w_h)_E \\ = (q_{\beta}^{n+1,m}, w_h)_E + \left(\frac{(\phi N_{\beta,h})^n}{\Delta t}, w_h \right)_E \quad \forall w_h \in W_h. \end{aligned} \quad (3.28)$$

3.5 Linearization

In this section we apply an inexact Newton method to linearize the implicit system of equations corresponding to the two formulations presented above. The Newton step iterate is represented by superscript ‘k’. For the sake of convenience we drop time iterate ‘n’ in the description below. All terms are evaluated at time ‘n+1’ unless stated explicitly otherwise.

3.5.1 Formulation I

$$\left\langle \frac{K^{-1}}{\lambda_t^{\tilde{m},k}} \delta z_{t,h}^k, v_h \right\rangle_{Q,E} - (\delta p_{w,h}^k, \nabla \cdot v_h)_E = -R_1 \quad (3.29)$$

$$\left(\sum_{\beta} \left(c_r p_{w,SC} \rho_{\beta}^{m+1,k} + \phi^{m+1,k} c_{\beta} \rho_{\beta}^{m+1,k} \right) \frac{S_{\beta,h}^m}{\Delta t} \delta p_{w,h}^k, w_h \right)_E + (\nabla \cdot \delta z_{t,h}^k, w_h)_E = -R_2 \quad (3.30)$$

$$\begin{aligned} R_1 = & \left\langle \frac{K^{-1}}{\lambda_t^{\tilde{m},k}} z_{t,h}^{\tilde{m},k}, v_h \right\rangle_{Q,E} - (p_{w,h}^{m+1,k}, \nabla \cdot v_h)_E - \left\{ \left(\left[\frac{\lambda_w}{\lambda_t} \right]^{\tilde{m},k} p_{cw}^m, \nabla \cdot v_h \right)_E \right. \\ & + \left(\sum_{\beta} \left[\frac{\lambda_{\beta}}{\lambda_t} \right]^{\tilde{m},k} \rho_{\beta}^{m+1,k} g \nabla d, v_h \right)_E - \int_{\partial E \cap \partial \Omega} \left[\frac{\lambda_w}{\lambda_t} \right]^{\tilde{m},k} p_{cw} v_h \cdot n \\ & \left. - \int_{\partial E \cap \partial \Omega} p_{w,h} v_h \cdot n \right\} \end{aligned} \quad (3.31a)$$

$$\begin{aligned} R_2 = & \left(\sum_{\beta} \frac{\phi^{m+1,k} N_{\beta,h}^{m+1,k}}{\Delta t}, w_h \right)_E + (\nabla \cdot z_{\beta,h}^{m+1,k}, w_h)_E \\ & - \left\{ (q_t^{n+1,m}, w_h)_E + \left(\sum_{\beta} \frac{(\phi \rho_{\beta} S_{\beta})^n}{\Delta t}, w_h \right)_E \right\} \end{aligned} \quad (3.31b)$$

Eliminating $\delta z_{t,h}$ from Eqns. (3.29) and (3.30) results in a linear system of equations in $\delta p_{w,h}$.

$$(B^T A^{-1} B + C) \delta p_{w,h}^k = B^T A^{-1} R_1 - R_2. \quad (3.32)$$

3.5.2 Formulation II

$$\left\langle \frac{K^{-1}}{\lambda_\beta^{m,k}} \delta \tilde{z}_{\beta,h}^k, v_h \right\rangle_{Q,E} - (\delta p_{w,h}^k, \nabla \cdot v_h)_E = -R_{1\beta} \quad (3.33)$$

$$(\delta z_{\beta,h}^k, v_h)_E - (\lambda_\beta \delta \tilde{z}_{\beta,h}^k, w_h)_E = -R_{2\beta} \quad (3.34)$$

$$\begin{aligned} & \left(\left(c_r p_{w,SC} \rho_\beta^{m+1,k} + \phi^{m+1,k} c_\beta \rho_\beta^{m+1,k} \right) \frac{N_{\beta,h}^m}{\Delta t} \delta p_{w,h}^k, w_h \right)_E + \left(\phi^{m+1,k} \rho_\beta^{m+1,k} \frac{\delta N_{\beta,h}^k}{\Delta t}, w_h \right)_E \\ & + (\nabla \cdot \delta z_\beta^k, w_h)_E = -R_{3\beta} \end{aligned} \quad (3.35)$$

$$- \sum_\beta \frac{c_\beta N_{\beta,h}^{m+1,k}}{\rho_\beta^{m+1,k}} \delta p_{w,h}^k + \sum_\beta \frac{1}{\rho_{\beta,h}^{m+1,k}} \delta N_{\beta,h}^k = -R_{4\beta} \quad (3.36)$$

Thus forming a linear system of equations. Eliminating $\delta z_{\beta,h}$, $\delta \tilde{z}_{\beta,h}$, $\delta N_{\beta,h}$ from Eqns. (3.33)-(3.36) gives a linear system of equations in $\delta p_{w,h}$.

Now that we have laid the groundwork for the two formulations it is important to discuss some of the distinguishing features between the two. Firstly, where the former has only two unknowns (p_w and S_w) the latter has three unknowns (p_w , N_w and N_o). Secondly, the second formulation differs in the use of the saturation constraint to form an implicit pressure system. This is in contrast to the first formulation where the sum of the two mass conservation equations is used. Thus first formulation satisfies the volume constraint

explicitly compared to the second formulation where the mass conservation equations are satisfied explicitly.

The two formulations are equivalent for fluid systems where densities are strong functions of pressure and are weak functions of saturation or concentrations. However if density is strongly dependent on both pressure and saturation then the second formulation is more appropriate. Therefore, in this work, we use the first approach for two-phase slightly and incompressible flows. Although not presented here the second approach is more suitable for a black oil system where the oil phase density changes substantially with the amount of dissolved gas. The second approach is also used for studying an equation of state, fully compressible, three-phase compositional flow and will be presented later.

3.6 Results

In this section, we present two numerical experiments for two-phase slightly compressible flow using formulation I. The first example simulates capillary end effects seen in core-flooding experiments in the absence of pressure gradient applied across a core. The second experiment shows spontaneous capillary imbibition and consequent saturation distribution inside the core balancing capillary and gravity forces. Figures 3.2 and 5.8 show the relative permeability and capillary pressure curves during these numerical experiments. Table 3.1 provides the associated rock and fluid property information. The simulations were carried out for a period of four days. Figure 3.4 shows the

| | | | |
|------------|--------------------------|-------------------|-------------------------|
| ϕ | 0.2 | $K_x = K_y = K_z$ | 50 mD |
| c_w | 1.E-7 psi ⁻¹ | c_o | 1.E-4 psi ⁻¹ |
| ρ_w | 62.4 lbm/ft ³ | ρ_o | 56 lbm/ft ³ |
| ν_w | 1 cP | ν_o | 2 cP |
| S_w^0 | 0.2 | P_w^0 | 1000 psi |
| S_{wirr} | 0.1 | S_{or} | 0.2 |

Table 3.1: Rock and fluid property information

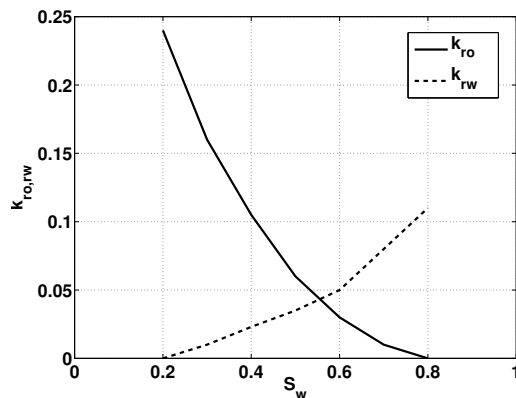


Figure 3.2: Oil and water phase relative permeability curves

cylindrical core represented using general hexahedral elements.

3.6.1 Capillary End Effect

This numerical experiment simulates spontaneous capillary imbibition of water phase at the two non-curved, circular cross sections of the cylindrical core. The curved surface is assumed to be no-flow to mimic conditions during core flooding experiments. Further a Dirichlet boundary condition of 1000 psi (same as initial condition) and $S_w = 1$ is assumed. Due to horizontal flow

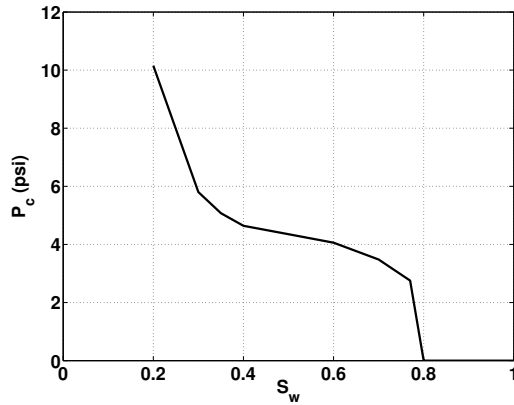


Figure 3.3: Rock matrix capillary pressure curve

through the core, gravity is assumed to be negligible and hence set to zero for this simulation. The capillary pressure decreases from positive values to zero as we move from the centre of the core toward the circular opening. This results in a spontaneous imbibition of water phase in the absence of a pressure gradient across the core. Figures 3.5 and 3.6 show pressure and saturation distributions, respectively after 2 and 4 days. The saturation distribution approaches an equilibrium after large time as the the phase fluid fluxes approach zero in the limit.

3.6.2 Capillary and Gravity Equilibrium

In this example, we use the same setup as describe before. The core is kept vertical with the gravity acting in the downward direction. Further the top circular cross-section is assumed to be no-flow in addition to the curved surface of the cylindrical core. A Dirichlet boundary condition is assumed

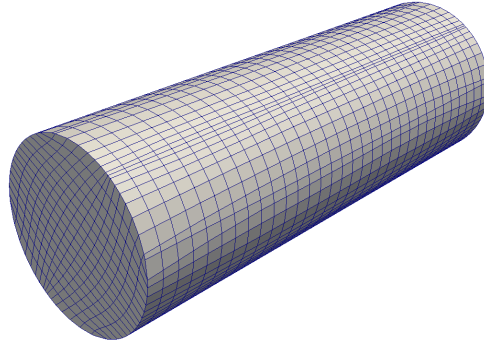


Figure 3.4: Cylindrical core

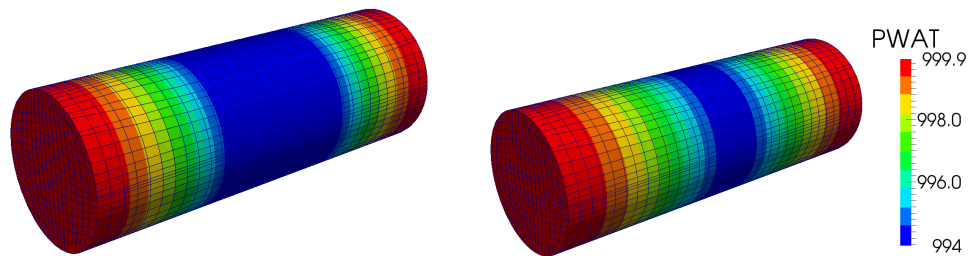


Figure 3.5: Water phase pressure distribution after 2 (left) and 4 (right) days

at the bottom circular cross-section. Under these conditions water rises up the core from the bottom due to capillary imbibition. The gravity acts against water imbibition and an equilibrium water saturation distribution is achieved where gravity and capillary forces balance each other. Figures 3.7, 3.8 and 3.9 show water phase pressure, oil phase pressure and water saturation distributions, respectively after 0 and 4 days.

The numerical experiments show that complex surfaces can be cap-

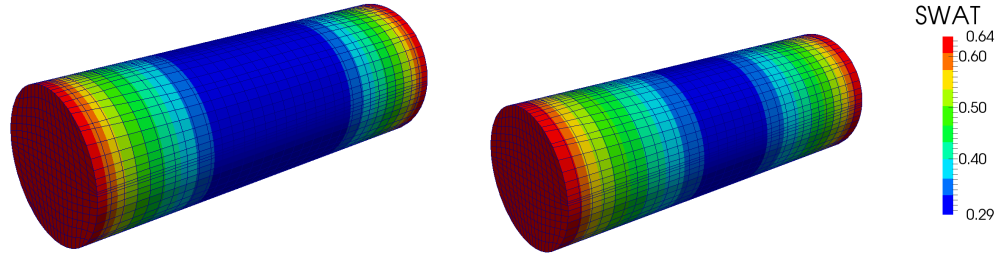


Figure 3.6: Water saturation distribution after 2 (left) and 4 (right) days

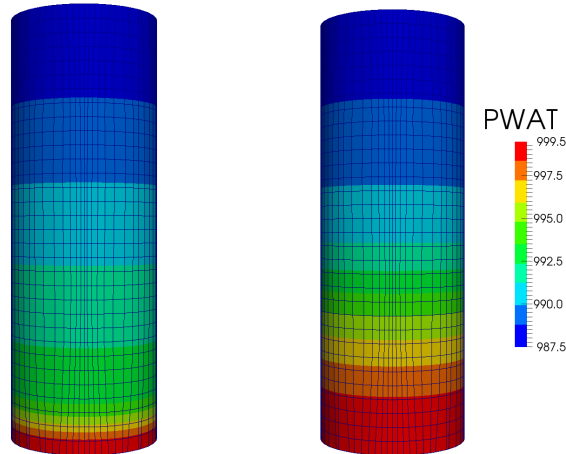


Figure 3.7: Water phase pressure distribution after 0 (left) and 4 (right) days

tured using general hexahedral elements. Further relative permeability, capillary pressure and gravity features associated with the two phase flow problem are accurately represented. The MFMFE scheme for solving two-phase flow problem presented here serves as a precursor to the more involved flow models in the following chapters. In the next chapter, we discuss a compositional flow formulation which is similar to formulation II described above.

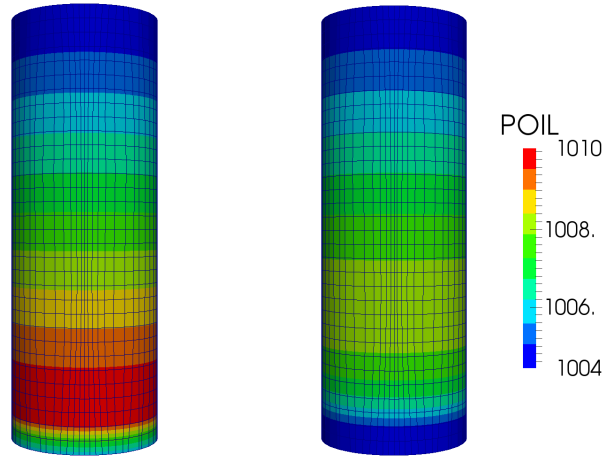


Figure 3.8: Oil phase pressure distribution after 0 (left) and 2 (right) days

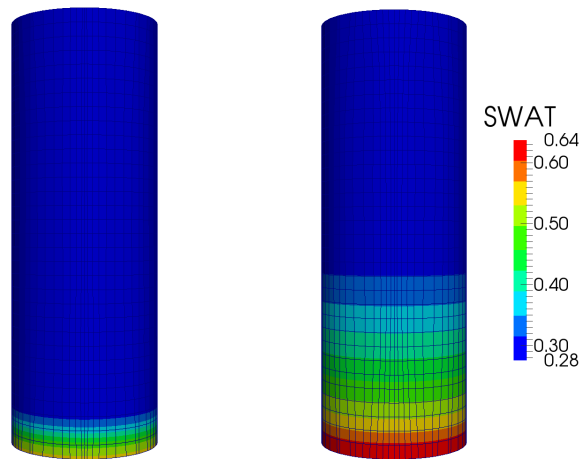


Figure 3.9: Water phase saturation distribution after 20 (left) and 2 (right) days

Chapter 4

Compositional Flow

4.1 Introduction

Compositional flow modeling has been used for simulating CO₂ sequestration, ground water remediation and contaminant plume migration. In the oil and gas industry it is widely used for evaluating gas flooding scenarios as a tertiary recovery process. The gas flooding targets achieving either direct or multi-contact miscibility, of the displacing and displaced fluids, to counter adverse mobilities to maximize recovery. A number of variants of the above process exist, based upon economical considerations, such as gas slug injection along with a chase fluid or water alternating gas (WAG). The modeling involves solving a system of non-linear equations, invoking a local equilibrium assumption, including an equation of state. This combined with partial differential equations representing mass conservation represent a differential algebraic system which is known for its numerical difficulties. An extensive amount of literature is available which elaborate on different model formulations and solution algorithms to address this problem.

This work has been partly presented at the ECMOR XIV conference (Singh and Wheeler (2014a)) and published as an ICES report (Singh and Wheeler (2014b)). The research is done primarily by Gurpreet Singh under the supervision of Prof. Mary F. Wheeler.

Some of the earliest expositions in compositional flow modeling were carried out by Roebuck et al. (1969) using a fully implicit solution scheme. Coats (1980) later presented another implicit formulation where the transmissibility terms (relative permeabilities) were treated implicitly during the construction of Jacobian matrix. A similar formulation with explicit transmissibility terms (relative permeabilities) was presented in Young and Stephenson (1983). These schemes were later categorized as primary variable switching (PVS) due to change of primary variables associated with phase appearance and disappearance. Here a phase is assumed to be present only if the phase saturations lie between 0 and 1. A local criteria based upon saturation pressure test is employed to test the stability of single phase grid-blocks. Lauser et al. (2011) pointed out some of the issues which may arise due to primary variable switching for near critical conditions. This was addressed by the latter using non-linear complimentary condition defined such that negativity of phase-compositions imply that the phase is not present.

A sequential solution scheme was presented by Acs et al. (1985) and Chang (1990) for solving compositional flow equations. An implicit pressure equation, with explicit treatment of transmissibility terms, is formed using volume balance assuming pore volume is equal to fluid volume. This is followed by an explicit concentration update. The approach was later named implicit pressure explicit concentration scheme on the lines of the well known implicit pressure explicit saturation (IMPES) scheme. Please note that the implicit or explicit treatment implies Newton iteration or time lagging terms to construct

an approximation of the exact Jacobian. Watts (1986) also presented an extension of the IMPES scheme for compositional flow following Acs et al. in the construction of a pressure equation based upon a volume balance or constraint. Once the pressure equation is solved the total fluxes are evaluated. A system of implicit saturation equations are then solved with implicit saturations. This is followed by phase flux evaluation and then component transport.

So far the sequential solution approaches discussed above march forward in time assuming the pressure and saturation equations are decoupled. Sun and Firoozabadi (2009) discuss a coupled IMPEC scheme where iterations are performed between implicit pressure equation and explicit concentration updates, for a given time-step, until a desired tolerance is achieved. The implicit pressure and saturation equations are discretized using mixed finite element (MFE) and linear, discontinuous-Galerkin (DG) scheme, respectively. In this work, we employ a similar iteratively coupled IMPEC solution scheme presented by Thomas (2009) while using a multipoint flux mixed finite element (MFME) method and lowest order DG for discretizing the pressure and saturation equations, respectively. This provides accurate and locally mass conservative fluxes and eliminates grid orientation effects owing to gradient in pressure. The MFME discretization also utilizes a full permeability tensor. We also differ in the use of a logically rectangular grid with general hexahedral elements. These elements lower the number of unknowns when compared to tetrahedral meshes. Further, the general hexahedral elements capture complex reservoir geometries without requiring substantial adjustment of associ-

ated petrophysical properties. This also allows for capturing of non-planar fractures (Singh et al. (2014b)) as a future prospect for compositional flow modeling in fractured poroelastic reservoirs.

It is also imperative to discuss some of the restrictions placed on phase-behavior modeling owing to a choice of solution algorithms discussed before. The Rachford-Rice (RR) (Rachford and Rice (1952)) equations allows a better treatment of the non-linearities presented by the phase behavior model. The constant-K flash represented by RR equations can be easily reformulated as a constrained optimization problem (Michelsen (1994)). The objective function for this minimization problem is known to be convex and therefore robust solution schemes can be utilized (Okuno et al. (2010)). However, the model formulations used in Lauser et al. (2011); Coats (1980) cannot take advantage of this due to the restrictive choice of primary unknowns. Furthermore, for implicit solution schemes, phase appearance and disappearance due to near critical fluid phase behavior poses significant problems. For primary variable switching (PVS) schemes this can introduce oscillations due to frequent changes in the rank of the Jacobian. Whereas, for complementarity condition based method the Jacobian can become ill-conditioned or rank deficient. The IMPEC schemes circumvent these issues at the cost of relatively expensive but robust phase-behavior calculations based upon successive substitution as opposed to fully implicit solution algorithms.

In the sections below, we begin by describing the compositional model formulation along with boundary, initial and closure conditions. This is fol-

lowed by a description of the hydrocarbon phase behavior model based upon the local equilibrium assumption. Please note that the aqueous phase is assumed to be slightly compressible. For the sake of brevity, we skip directly to the fully discrete formulation where a weak formulation of the problem is presented along with the associated finite element spaces and quadrature rules. We also briefly discuss the linearization choices leading to the construction of the implicit pressure equation. Finally, we present a number of numerical results comprising of verification and benchmarking results along with a comparison between TPFA (two-point flux approximation) and MFME schemes. A synthetic field case where gas flooding is used as a tertiary recovery process further demonstrates the model capabilities for complex cases.

4.2 Model Formulation

We first present a continuum description of the compositional flow model. The general mass balance equation can be written in the differential form (also referred to as the strong form) and is given by Eqn. (4.1),

$$\frac{\partial W_{i\beta}}{\partial t} + \nabla \cdot F_{i\beta} - R_{i\beta} - r_{mi\beta} = 0. \quad (4.1)$$

Where, $W_{i\beta}$ is the concentration of component i in phase β , $F_{i\beta}$ the flux of component i in phase β , $R_{i\beta}$ the rate of generation/destruction of component i in phase β owing to reactive changes and $r_{mi\beta}$ the rate of increase/decrease component i in phase β owing to phase changes. The mass balance equation

(4.1) can be expressed in an expanded form given by,

$$\frac{\partial(\epsilon_\beta \rho_\beta \xi_{i\beta})}{\partial t} + \nabla \cdot (\rho_\beta \xi_{i\beta} z_\beta - \epsilon_\beta D_{i\beta} \cdot \nabla (\rho_\beta \xi_{i\beta})) = \epsilon_\beta r_{i\beta} + r_{mi\beta}. \quad (4.2)$$

Here, ϵ_β is the volume occupied by phase β , ρ_β the density of phase β , $\xi_{i\beta}$ the fraction of component i in phase β and $D_{i\beta}$ the dispersion tensor. Please note that the equations outlined in this section can have either a mass or molar basis. For the purpose of simplicity, a number of assumptions were made as stipulated below:

1. Rock-fluid interactions are neglected i.e., no sorption processes are considered.
2. Non-reactive flow.

Applying these assumptions to Eqn. (4.2), we obtain Eqn. (4.3).

$$\frac{\partial(\phi S_\beta \rho_\beta \xi_{i\beta})}{\partial t} + \nabla \cdot (\rho_\beta \xi_{i\beta} z_\beta - \phi S_\beta D_{i\beta} \cdot \nabla (\rho_\beta \xi_{i\beta})) = q_{i\beta} + r_{mi\beta} \quad (4.3)$$

4.2.1 Component conservation equations

Summing eqn. (4.3) over the total number of phases (N_p) and noting that $\sum_\beta r_{mi\beta} = 0$ results in eqn. (4.4).

$$\frac{\partial}{\partial t} \left(\sum_\beta \phi S_\beta \rho_\beta \xi_{i\beta} \right) + \nabla \cdot \sum_\beta (\rho_\beta \xi_{i\beta} z_\beta - \phi S_\beta D_{i\beta} \cdot \nabla (\rho_\beta \xi_{i\beta})) = \sum_\beta q_{i\beta} \quad (4.4)$$

The phase fluxes (z_β) are given by Darcy's law,

$$z_\beta = -K \frac{k_{r\beta}}{\nu_\beta} (\nabla p_\beta - \rho_\beta g). \quad (4.5)$$

Here, S_β is the saturation of phase β (ratio of volume of phase β to pore volume), ϕ the porosity (ratio of pore volume to bulk volume), $q_{i\beta}$ the rate of injection of component i in phase β (mass/mole/volume basis), and u_β the Darcy flux of phase β . Also let, $N_i = \sum_\beta \rho_\beta S_\beta \xi_{i\beta}$ and $q_i = \sum_\beta q_{i\beta}$ then the component conservation equations can be written as,

$$\frac{\partial}{\partial t} (\phi N_i) + \nabla \cdot F_i - \nabla \cdot \left(\sum_\beta \phi S_\beta D_{i\beta} (\nabla \rho_\beta \xi_{i\beta}) \right) = q_i. \quad (4.6)$$

We define component flux F_i as,

$$F_i = -K \sum_\beta \rho_\beta \xi_{i\beta} \frac{k_{r\beta}}{\nu_\beta} (\nabla p_\beta - \rho_\beta g), \quad (4.7a)$$

$$F_i = -K \left(\sum_\beta \rho_\beta \xi_{i\beta} \frac{k_{r\beta}}{\nu_\beta} (\nabla p_{\text{ref}} - \rho_\beta g) + \sum_{\beta \neq \text{ref}} \rho_\beta \xi_{i\beta} \frac{k_{r\beta}}{\nu_\beta} \nabla p_{c\beta} \right). \quad (4.7b)$$

4.2.2 Boundary and initial conditions

For simplicity of model description we assume no flow external boundary condition everywhere ($\partial\Omega^N = \partial\Omega$). However, this is by no means restrictive and more general boundary conditions can be also be treated.

$$z_\beta \cdot n = 0 \text{ on } \partial\Omega^N \quad (4.8)$$

The initial condition is as follows,

$$p_{\text{ref}} = p^0, \quad (4.9a)$$

$$N_i = N_i^0. \quad (4.9b)$$

4.2.3 Closure and constraints

Assuming the water component ($i=1$) is present only in the water phase, the phase saturations S_β are calculated as follows:

$$\begin{aligned} S_w &= \frac{N_w}{\rho_w}, \\ S_o &= \frac{(1 - \zeta)}{\rho_o} \sum_{i=2}^{N_c} N_i, \\ S_g &= \frac{\zeta}{\rho_g} \sum_{i=2}^{N_c} N_i. \end{aligned} \quad (4.10)$$

Where, ζ is the mole fraction of the hydrocarbon gas phase, and o , w and g represent the hydrocarbon oil, water and hydrocarbon gas phases, respectively.

A saturation constraint exist on phase saturation given by,

$$\sum_{\beta} S_\beta = 1. \quad (4.11)$$

The capillary pressure is a monotonic and continuous function of reference phase saturation (S_{ref}). The relative permeabilities are continuous functions of reference phase saturation (S_{ref}). A more general table based capillary pressure and relative permeability curve description has also been implemented.

$$p_{c\beta} = p_\beta - p_{\text{ref}} \quad (4.12)$$

Further, a slightly compressible and cubic equation of states are used for water and hydrocarbon phases, respectively.

$$\rho_w = \rho_{w,0} \exp [C_w (p_{\text{ref}} + p_{cw} - p_{\text{ref,std}})] \quad (4.13a)$$

$$\rho_\beta = \frac{p_\beta}{Z_\beta RT}, \beta \neq w \quad (4.13b)$$

Here, ρ_β is the molar density of phase β including water. The porous rock matrix is assumed to be compressible, with C_r as the rock compressibility, satisfying the following relationship,

$$\phi = \phi_0 [1 + C_r(p_{\text{ref}} - p_{\text{ref,std}})]. \quad (4.14)$$

4.3 Hydrocarbon Phase Behavior Model

The phase behavior modeling for hydrocarbon phases is based upon a local equilibrium assumption. The equilibrium component concentrations are then calculated point wise given a pressure (p_{ref}), temperature (T) and overall mole fraction (ξ_i). A normalization of component concentrations N_i give overall component mole fractions ξ_i .

$$\xi_i = \frac{N_i}{\sum_{i=2}^{N_c} N_i} \quad (4.15)$$

Let, $\xi_{i\beta}$ be the mole fraction of component i in phase β and ζ the normalized moles of gas phase, then from mass balance we have,

$$\zeta \xi_{ig} + (1 - \zeta) \xi_{io} = \xi_i, \quad (4.16a)$$

$$\sum_{i=2}^{N_c} \xi_{io} = 1, \quad (4.16b)$$

$$\sum_{i=2}^{N_c} \xi_{ig} = 1. \quad (4.16c)$$

The partitioning coefficient K_i^{par} of a component i between hydrocarbon phases is given by,

$$K_i^{\text{par}} = \frac{\xi_{ig}}{\xi_{io}}. \quad (4.17)$$

Rearranging the above equations we have,

$$\xi_{io} = \frac{\xi_i}{1 + (K_i^{\text{par}} - 1)\zeta}, \quad (4.18a)$$

$$\xi_{ig} = \frac{K_i^{\text{par}} \xi_i}{1 + (K_i^{\text{par}} - 1)\zeta}. \quad (4.18b)$$

The Rachford-Rice equation is given by,

$$f = \sum_{i=2}^{N_c} \frac{(K_i^{\text{par}} - 1)\xi_i}{1 + (K_i^{\text{par}} - 1)\zeta} = 0. \quad (4.19)$$

At equilibrium, the fugacities of a component i are equal in all the phases given by the iso-fugacity criteria (4.20).

$$g = \ln(\Phi_{io}) - \ln(\Phi_{ig}) - \ln K_i^{\text{par}} = 0. \quad (4.20)$$

Where the fugacity of component i in phase β is given by,

$$\begin{aligned} \ln(\Phi_{i\beta}) = & -C_i + \frac{B_i}{B_\beta}(\bar{Z}_\beta - 1) - \ln(\bar{Z}_\beta - B_\beta) \\ & - \frac{A_\beta}{2\sqrt{2}B_\beta} \left(\frac{2\sum_{j=2}^{N_c} \xi_{j\beta} A_{ij}}{A_\beta} - \frac{B_i}{B_\beta} \right) \ln \left(\frac{\bar{Z}_\beta + (1 + \sqrt{2})B_\beta}{\bar{Z}_\beta + (1 - \sqrt{2})B_\beta} \right). \end{aligned} \quad (4.21)$$

For a given pressure (P^*), temperature (T) and composition (\vec{z}) equations (4.19) and(4.20) can be linearized in terms of $\ln K_i$ and ζ .

$$\begin{pmatrix} \partial f / \partial \ln K^{\text{par}} & \partial f / \partial \zeta \\ \partial g / \partial \ln K^{\text{par}} & \partial g / \partial \zeta \end{pmatrix} \begin{pmatrix} \delta \ln K^{\text{par}} \\ \delta \zeta \end{pmatrix} = \begin{pmatrix} -R_1 \\ -R_2 \end{pmatrix} \quad (4.22)$$

Eliminating $\delta\zeta$ from the linear system,

$$\left(\frac{\partial f}{\partial \ln K^{\text{par}}} - \frac{\partial f}{\partial \zeta} \left(\frac{\partial g}{\partial \zeta} \right)^{-1} \frac{\partial g}{\partial \ln K^{\text{par}}} \right) \delta \ln K^{\text{par}} = -R_1 + \frac{\partial f}{\partial \zeta} \left(\frac{\partial g}{\partial \zeta} \right)^{-1} R_2. \quad (4.23)$$

Since the system under consideration is highly non-linear with multiple solutions we must either provide good initial guesses or constraint the system appropriately so as to get a unique solution. The phase behavior model relies upon providing a good initial estimates for $\ln K_i^{\text{par}}$ and consequently ζ based upon heuristics. The Wilson's equation (4.24) is an empirical correlation which provides initial guesses for K_i^{par} s.

$$K_i^{\text{par}} = \frac{1}{p_{ri}} \exp \left[5.37(1 + \omega_i) \left(1 - \frac{1}{T_{ri}} \right) \right] \quad (4.24)$$

Using these partitioning coefficients (K_i^{par}) and the given composition (ξ_i) equation (4.19) is then solved to get an initial estimate for ζ . We use three different ways of determining phase stability and consequently the compositions of unstable phases using iso-fugacity flash calculations. The three methods differ either in the calculation of initial estimates of K_i^{par} s or the determination of phase stability (negative flash vs. tangent plane distance). However, the primary unknowns and equations for the three methodologies are the same as presented in this section.

For non-polar molecules (hydrocarbon) Peng-Robinson cubic equation (B.1) of state empirically correlates pressure, temperature and molar volume. The values of Z_β are calculated using this cubic equation of state, given in the appendix. For given pressure, temperature, composition (\vec{n}), partitioning

coefficients (\vec{K}^{par}) and vapor fraction (ζ), the cubic equation of state provides three values of Z_β . A unique solution is obtained by selecting the root which has the minimum Gibb's free energy given by,

$$\left. \frac{\partial G}{\partial n_i} \right|_{\beta, T, P} = \nu_{i\beta} = \nu_i^o + RT \ln \Phi_{i\beta}, \quad (4.25a)$$

$$dG|_{\beta, T, P} = \sum_{i=2}^{N_c} \left. \frac{\partial G}{\partial n_i} \right|_{\beta, T, P} dn_i = h(Z_\beta). \quad (4.25b)$$

Where ν_i^o represents the reference state and is a different constant for each component. Amongst the three roots of the cubic EOS, Z_β corresponding to the minimum $dG|_{\beta, T, P}$ is chosen. The cubic EOS, or alternatively Z_β , is not a part of the Jacobian (Eqn. (4.22)) due to the restriction placed by minimum Gibb's free energy constraint. The algorithm for flash iteration can be outlined as follows:

1. Calculate an initial estimate of K_i^{par} s from Wilson's correlation (4.24).
2. For a given P, T, \vec{z} and K_i^{par} s calculated above, solve the Rachford-Rice equation (4.19) for ζ .
3. Calculate $\xi_{i\beta}$ from (4.18).
4. Evaluate Z_β using equation (B.1).
5. Evaluate residuals of fugacity equations (4.20), stop if convergence tolerance is achieved.
6. If tolerance is not achieved, solve (4.23) for new values of K_i^{par} s.

7. Stop if K_i^{par} is trivial i.e., $K_i^{\text{par}} = 1$.

8. Return to 1.

4.4 Fully Discrete Formulation

We now consider the fully discrete variational formulation of the compositional flow model. The variables are taken at the most recent time iterate level everywhere except whenever explicitly indicated by index n. An iteratively coupled implicit pressure explicit concentration (IMPEC) approach is used to solve equations in pressure (p_{ref}) and concentration (N_i) variables. The pressure and concentration equations are discretized in time using backward and forward Euler schemes, respectively. Figure 4.1 shows a flow chart of the iteratively coupled IMPEC scheme used in this work. The corresponding iterate level is represented by the index k. The discrete variational problem, similar to the one described in the single phase flow chapter, for reservoir pressure then reads: Given $N_{i,h}^k \in W_h$, find $F_{i,h}^{k+1} \in V_h$ and $p_{\text{ref},h}^{k+1} \in W_h$ such that,

$$\begin{aligned}
& \left\langle \frac{1}{\Lambda_{i,h}^{\bar{k}}} K^{-1} F_{i,h}^{k+1}, v_h \right\rangle_{Q,E} - (p_{\text{ref},h}^{k+1}, \nabla \cdot v_h)_E \\
&= - \int_{\partial E \cap \partial \Omega} p_{\text{ref}} v_h \cdot n - \left(\frac{1}{\Lambda_{i,h}^{\bar{k}}} \sum_{\beta \neq \text{ref}} \rho_{\beta,h}^{\bar{k}} \xi_{i\beta,h}^{\bar{k}} \lambda_{\beta,h}^{\bar{k}} \nabla p_{c\beta,h}^{\bar{k}}, v_h \right)_E \\
&+ \left(\frac{1}{\Lambda_{i,h}^{\bar{k}}} \sum_{\beta} (\rho_{\beta,h}^2)^{\bar{k}} \xi_{i\beta,h}^{\bar{k}} g, v_h \right)_E,
\end{aligned} \tag{4.26}$$

$$\left(\frac{\phi_h^{k+1} N_{i,h}^k}{\Delta t}, w_h \right)_E + (\nabla \cdot F_{i,h}^{k+1}, w_h)_E - \left(\nabla \cdot \sum_{\beta} \left\{ \phi_h^{k+1} S_{\beta,h}^{\tilde{k}} D_{i\beta,h} \cdot \nabla \left(\rho_{\beta,h}^{\tilde{k}} \xi_{i\beta,h}^{\tilde{k}} \right) \right\}, w_h \right)_E = \left(q_{i,h}^{\tilde{k}}, w_h \right) + \left(\frac{\phi_h^n N_i^n}{\Delta t}, w_h \right)_E. \quad (4.27)$$

Here, \tilde{k} is used to represent iterate level for quantities which depend on both pressure and concentrations such that p_{ref}^{k+1} and N_i^k . The discrete variational problem for the concentration update is: Given $p_{\text{ref},h}^{k+1} \in W_h$, $F_{i,h}^{k+1} \in V_h$ and $N_{i,h}^k \in W_h$, find $N_{i,h}^{k+1} \in W_h$ such that,

$$\left(\frac{\phi_h^{k+1} N_{i,h}^{k+1}}{\Delta t}, w_h \right)_E + (\nabla \cdot F_{i,h}^{k+1}, w_h)_E - \left(\nabla \cdot \sum_{\beta} \left\{ \phi_h^{k+1} S_{\beta,h}^{\tilde{k}} D_{i\beta,h} \cdot \nabla \left(\rho_{\beta,h}^{\tilde{k}} \xi_{i\beta,h}^{\tilde{k}} \right) \right\}, w_h \right)_E = \left(q_{i,h}^{\tilde{k}}, w_h \right) + \left(\frac{\phi_h^n N_i^n}{\Delta t}, w_h \right)_E. \quad (4.28)$$

Please note that a description of algebraic equations associated with the implicit pressure (Eqn. (4.27)) and explicit concentration (Eqn. (4.28)) systems is omitted to avoid redundancy. The reader is referred to earlier sections on compositional and phase behavior model formulations for necessary relations.

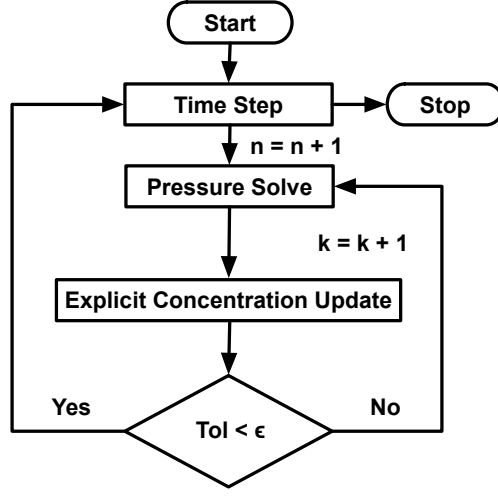


Figure 4.1: Iteratively coupled implicit pressure explicit concentration (IM-PEC) scheme.

4.4.1 Treatment of diffusion/dispersion

The diffusion-dispersion tensor is the sum of molecular diffusion and hydrodynamic dispersion given by:

$$D_{i\beta} = D_{i\beta}^{\text{mol}} + D_{i\beta}^{\text{hyd}}, \quad (4.29a)$$

$$D_{i\beta}^{\text{mol}} = \tau_{\beta} d_{m,i\beta} I, \quad (4.29b)$$

$$D_{i\beta}^{\text{hyd}} = d_{t,\beta} |z_{\beta}| I + (d_{l,\beta} - d_{t,\beta}) z_{\beta} z_{\beta}^T / |z_{\beta}|. \quad (4.29c)$$

Here τ_{β} is the tortuosity of phase β , $d_{m,i\beta}$, $d_{l,\beta}$, $d_{t,\beta}$ are the molecular, longitudinal and transverse dispersion coefficients, respectively. We define the diffusive/dispersive flux as:

$$J_{i\beta} = \phi S_\beta D_{i\beta} \rho_\beta \cdot \nabla (\xi_{i\beta}), \quad (4.30)$$

$$\left\langle \frac{1}{\phi \rho_\beta S_\beta} D_{i\beta}^{-1} J_{i\beta}, v_h \right\rangle_{Q,E} - (\xi_{i\beta}, \nabla \cdot v_h)_E = - \int_{\partial E \cap \partial \Omega} \xi_{i\beta} v_h \cdot n. \quad (4.31)$$

The diffusion-dispersion tensor is evaluated locally for each corner-point similar to the permeability tensor. The molecular diffusion ($D_{i\beta}^{\text{mol}}$) is evaluated using cell-centered values of $d_{m,i\beta}$. Further, the hydrodynamic dispersion tensor ($D_{i\beta}^{\text{hyd}}$) is calculated using the three flux degrees of freedom associated with each corner-point.

4.5 Linearization

A Newton method is applied to form a linear system of equations followed by elimination of component concentrations and fluxes resulting in a implicit pressure system. Once the pressures are evaluated an explicit update of N_c component concentrations is performed (IMPEC). The three phase saturations are calculated using equations (4.10) independently. Linearizing the above system of equations,

$$\left\langle \frac{1}{\Lambda_{i,h}} K^{-1} \delta F_{i,h}, v_h \right\rangle_{Q,E} - (\delta p_{\text{ref},h}, \nabla \cdot v_h)_E = -R_{3i}, \quad (4.32)$$

$$\begin{aligned} \left(\frac{\phi_h^{n+1,k} \delta N_{i,h}}{\Delta t}, w_h \right)_E + \left(\frac{N_{i,h}^{n+1,k}}{\Delta t} \frac{\partial \phi}{\partial p_{\text{ref},h}} \delta p_{\text{ref},h}, w_h \right)_E \\ + (\nabla \cdot \delta F_{i,h}, w_h)_E = -R_{4i}. \end{aligned} \quad (4.33)$$

The local mass matrix and right hand side for component i can be written as,

$$\begin{pmatrix} A_i & B & 0 \\ B^T & C_i & D_i \end{pmatrix} \begin{pmatrix} \delta F_i \\ \delta p_{\text{ref}} \\ \delta N_i \end{pmatrix} = \begin{pmatrix} -R_{3i} \\ -R_{4i} \end{pmatrix}. \quad (4.34)$$

Please note that C contains contribution from $\frac{\partial \phi}{\partial p_{\text{ref}}}$ and D contains $\frac{\partial \rho_\beta}{\partial p_{\text{ref}}}$ indirectly through N. We then eliminate δF_i in favor of cell centered quantities δp_{ref} and δN_i . The saturation constraint, iso-fugacity criteria and RR equation can be linearized in terms of the unknowns p_{ref} , N_i , K_i^{par} and ζ using equations (4.15) and (4.18) as,

$$\begin{aligned} \sum_{\beta} \frac{\partial S_{\beta}}{\partial p_{\text{ref}}} \delta p_{\text{ref}} + \sum_{\beta} \sum_i \frac{\partial S_{\beta}}{\partial N_i} \delta N_i + \sum_{\beta} \sum_i \frac{\partial S_{\beta}}{\partial \ln K_i^{\text{par}}} \delta \ln K_i^{\text{par}} + \sum_{\beta} \frac{\partial S_{\beta}}{\partial \zeta} \delta \zeta \\ = 1 - \sum_{\beta} S_{\beta} = -R_5, \end{aligned} \quad (4.35)$$

$$\Phi_{i\beta} = \Phi_{i\beta}(p_{\text{ref}}, \xi_{i\beta}) = \Phi_{i\beta}(p_{\text{ref}}, \xi_i, K_i^{\text{par}}) = \Phi_{i\beta}(p_{\text{ref}}, N_i, K_i^{\text{par}}), \quad (4.36)$$

$$\begin{aligned} \frac{\partial \ln \Phi_{io}}{\partial p_{\text{ref}}} \delta p_{\text{ref}} + \sum_{k=2}^{N_c} \frac{\partial \ln \Phi_{io}}{\partial N_k} \delta N_k + \sum_{k=2}^{N_c} \frac{\partial \ln \Phi_{io}}{\partial \ln K_k^{\text{par}}} \delta \ln K_k^{\text{par}} + \frac{\partial \ln \Phi_{io}}{\partial \zeta} \delta \zeta \\ - \left(\frac{\partial \ln \Phi_{ig}}{\partial p_{\text{ref}}} \delta p_{\text{ref}} + \sum_{k=2}^{N_c} \frac{\partial \ln \Phi_{ig}}{\partial N_k} \delta N_k + \sum_{k=2}^{N_c} \frac{\partial \ln \Phi_{ig}}{\partial \ln K_k^{\text{par}}} \delta \ln K_k^{\text{par}} + \frac{\partial \ln \Phi_{ig}}{\partial \zeta} \delta \zeta \right) \\ - \frac{\partial \ln K_i^{\text{par}}}{\partial \ln K_k^{\text{par}}} \delta \ln K_k^{\text{par}} = -R_{6i}. \end{aligned} \quad (4.37)$$

The above equations can also be written in the matrix form as,

$$\begin{pmatrix} E & F & G & H \\ I & J & K & L \\ 0 & N & O & P \end{pmatrix} \begin{pmatrix} \delta p_{\text{ref}} \\ \delta N \\ \delta \ln K^{\text{par}} \\ \delta \zeta \end{pmatrix} = \begin{pmatrix} -R_5 \\ -R_6 \\ -R_7 \end{pmatrix}. \quad (4.38)$$

We then construct the pressure equation by further eliminating δN and $\delta \ln K^{\text{par}}$. Eliminating δF , δN and $\delta \ln K^{\text{par}}$ from the above linear system of equations

results in an implicit pressure system. Note that the diffusion is handled explicitly for both the implicit pressure solve and the concentration update. The values of phase compressibilities (Z_β) are Newton iteration lagged and are evaluated explicitly given pressure P , temperature T and component concentrations N_i s. The derivatives of Z_β with respect to P and N_i are therefore set to zero in the Jacobian. The Z_β contribution is accounted for in the residual term. A more rigorous treatment would be to expand the Jacobian in terms of Z_β as well. However, the minimum Gibbs free energy constraint (for a unique Z_β) given by equation (4.25) is difficult to utilize.

4.6 Results

In this section, we present numerical experiments to verify and demonstrate the capabilities of MFME discretization scheme for compositional flow modeling. We begin with a verification case where a comparison is made between TPFA and MFME discretization schemes for matching conditions. This is followed by another numerical experiment where we use a checkerboard pattern permeability field to demonstrate better fluid front resolution for MFME scheme. Finally, we present a synthetic Frio field example where CH_4 is injected to achieve multi-contact miscible flooding.

4.6.1 Verification and benchmarking

Here we present a comparison between TPFA and MFME discretizations with a diagonal permeability tensor. A quarter five spot pattern with 3

components (C_1 , C_6 and C_{20}) in addition to the water component. Both the injection (bottom left corner, Figure 4.2) and production (top right corner, Figure 4.2) wells are bottom hole pressure specified with a pressure specification of 1200 and 900 psi, respectively. The injection composition is kept constant at 100% C_1 with reservoir and grid block dimensions of 1000ft \times 1000ft \times 20ft and 20ft \times 20ft \times 20ft, respectively. The initial reservoir pressures and water saturations are 1000 psi and 0.2, respectively. The gas saturation profiles as

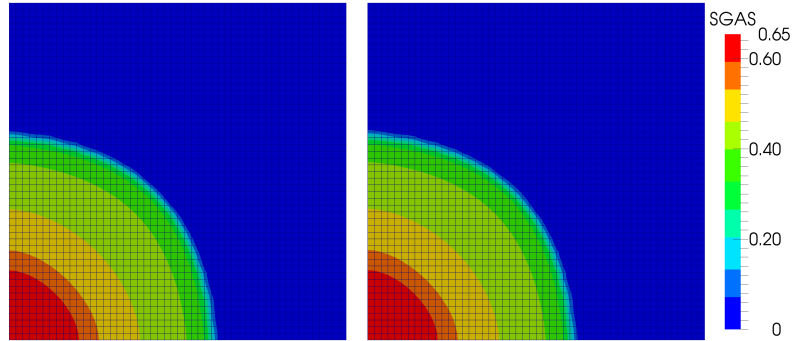


Figure 4.2: Gas saturation profile after 500 days using TPFA (left) and MFME (right) discretizations.

the end of 500 days for the two schemes are shown in Figure 4.2. A homogeneous, isotropic and diagonal permeability tensor field of 50 mD was assumed with a homogeneous porosity field of 0.3. The temperature was kept constant at 160 F. Figure 4.3 shows variation of component concentrations along the line joining injector and producer for both TPFA (circle) and MFME (solid line) discretizations.

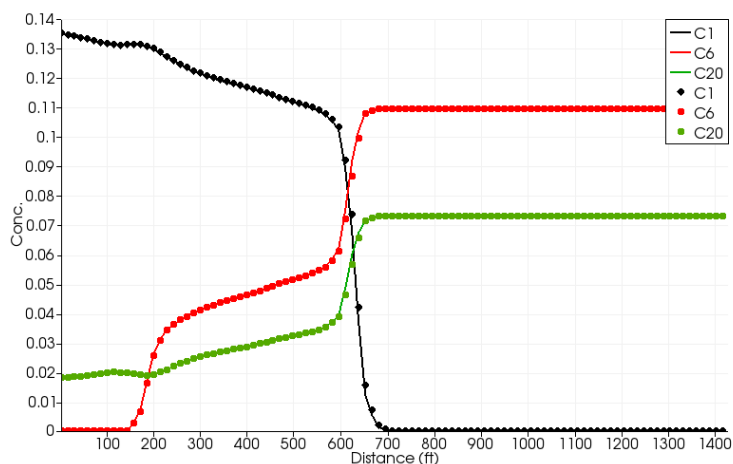


Figure 4.3: Component concentrations along the injector-producer line after 500 days for MFMFE (solid line) and TPFA (circles) schemes

4.6.2 Full permeability tensor test

This numerical experiment demonstrates the differences in saturation profiles between MFMFE and TPFA discretization due to the use of a full permeability tensor. Two bottom hole pressure specified wells are used with the injector (Fig. 4.4, bottom left corner) at 2200 psi and producer (Fig. 4.4, top right corner) at 900 psi. A homogenous, isotropic, diagonal permeability tensor of 100mD is assumed for the TPFA scheme. For the MFMFE scheme a homogeneous, full permeability tensor with 100mD diagonal and 50mD off-diagonal values is used. Other fluid and reservoir properties are kept the same as in the previous example. The reservoir and grid block dimensions for the numerical simulation are 1000ft \times 1000ft \times 20ft and 100ft \times 100ft \times 20ft, respectively.

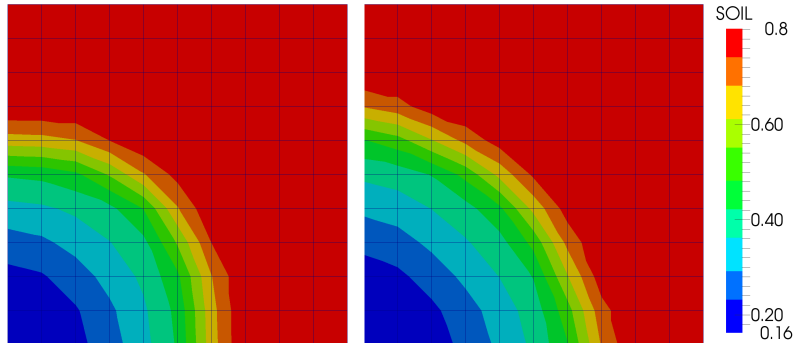


Figure 4.4: Oil saturation profiles after 50 days for MFMFEE (left) and TPFA (right) discretizations.

Figure 4.4 shows oil saturation profile for the two schemes after 50 days. As can be see, the oil saturation front for the TPFA scheme has a larger radius of curvature compared to the MFMFEE scheme.

4.6.3 Checker-board pattern test

In this example, we demonstrate the diagonal flow capability of the MFMFEE scheme. The reservoir and fluid property information is kept the same as the previous example differing only in permeability values. A checker-board permeability field, as shown in figure 4.5 (left), is taken with values of 1mD (blue) and 100mD (red) to exaggerate the effects. The injection (bottom left corner) and production (top right corner) wells are bottom hole pressure specified with a pressure specification of 2200 and 900 psi, respectively. Additionally, small off diagonal permeability values of 0.5mD were taken to construct a full permeability tensor for the MFMFEE scheme.

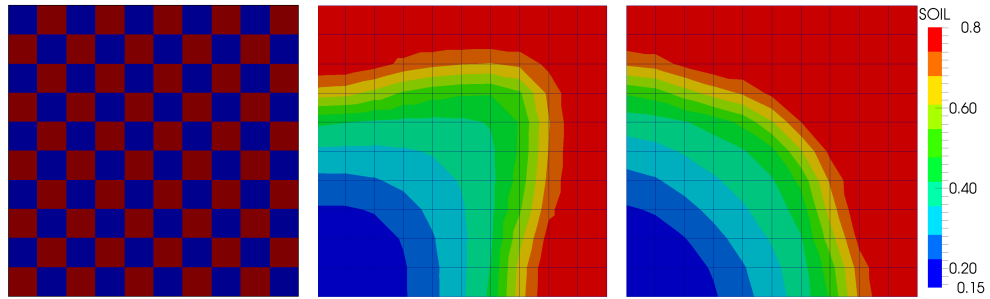


Figure 4.5: Permeability field (left) and gas saturation profiles after 3000 days for MFMFE (middle) and TPFA (right) discretizations.

Figure 4.5 also shows the oil saturation profiles for the two discretization schemes after 3000 days. The saturation profile on the left indicates a faster breakthrough of the injected gas compared to the right. The MFMFE scheme is able to identify the high permeability diagonal path and is therefore able to better resolve pressure and saturations at the fluid front.

4.6.4 Frio field test case

In this example, we present a synthetic field case using a section of Frio field geometry information to demonstrate some of the model capabilities. Note that the general hexahedral elements allow us to capture reservoir geometry accurately without requiring substantial changes in the available petrophysical data. We consider six hydrocarbon components (C_1 , C_3 , C_6 , C_{10} , C_{15} and C_{20}) in addition to water forming the fluid composition. The fluid system can be at most three phases at given location, depending upon phase behavior calculations, including water, oil and gas phases. The initial

hydrocarbon composition in the reservoir is taken to be 5% C_3 , 40% C_6 , 5% C_{10} , 10% C_{15} and 40% C_{20} with an initial reservoir pressure of 2000 psi. Further, the water saturation (S_w) at time $t = 0$ is taken to be 0.2. A total of 8 bottom hole pressure specified wells were considered comprising of 3 production and 5 injection wells. The permeability and porosity fields are shown to be around typical values of 50 mD and 0.2, respectively. The injection composition was kept constant at 100% C_1 during the entire simulation run spanning 1000 days. An isothermal reservoir condition was assumed at a temperature of 160 F.

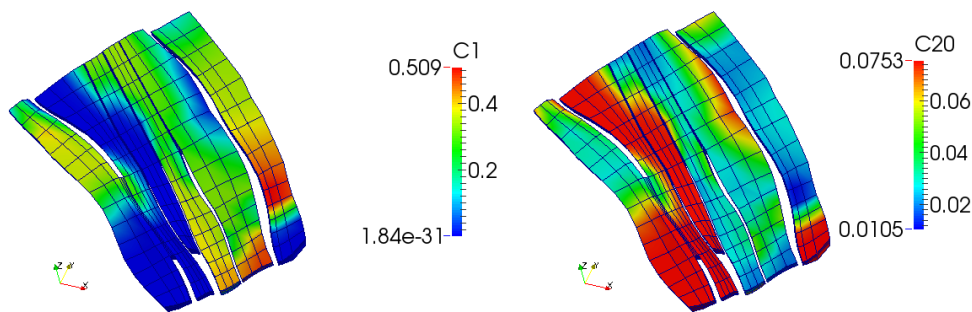


Figure 4.6: Concentration profiles for lightest (C_1) and heaviest (C_{20}) components after 1000 days.

A multi-contact miscible (MCM) flood is achieved at the given reservoir pressure and temperature conditions. Figure 4.6 shows the concentration profiles for the lightest and heaviest hydrocarbon components after 1000 days. Further, figure 4.7 shows the gas and oil saturation profiles after 1000 days.

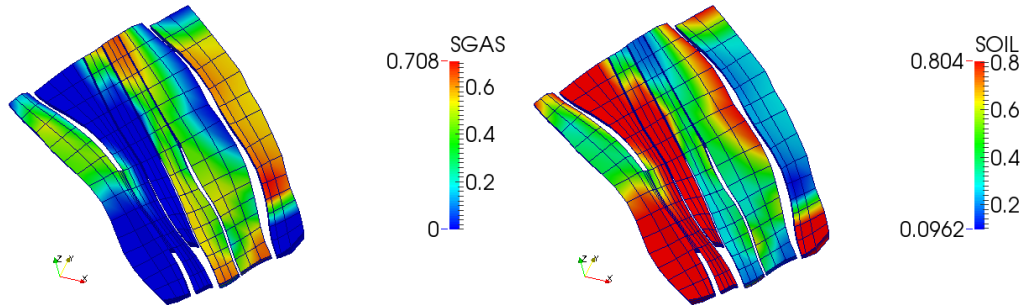


Figure 4.7: Saturation profiles for gas (left) and oil (right) phases after 1000 days.

4.6.5 Brugge field CO₂ flooding

In this example, we use CO₂ gas flooding (Peters et al. (2009); Chen et al. (2010)) as the tertiary mechanism for recovering hydrocarbons. The complex reservoir geometry is captured using $9 \times 48 \times 139$ general hexahedral elements and then discretized using a MFME scheme. A constant temperature of 160 F is specified assuming an isothermal reservoir condition. The initial hydrocarbon composition is 40% (C_6) and 60% (C_{20}) with an initial reservoir pressure of 1500 psi. The permeability and porosity fields are shown in Figures 4.11 and 4.12.

An injected gas composition of 100% CO₂ is further specified. Fig. shows the Brugge field geometry with 30 bottom-hole pressure specified wells with 10 injectors at 3000 psi and 20 producers at 1000 psi. The porous rock matrix is assumed to be water wet as reflected by the relative permeability

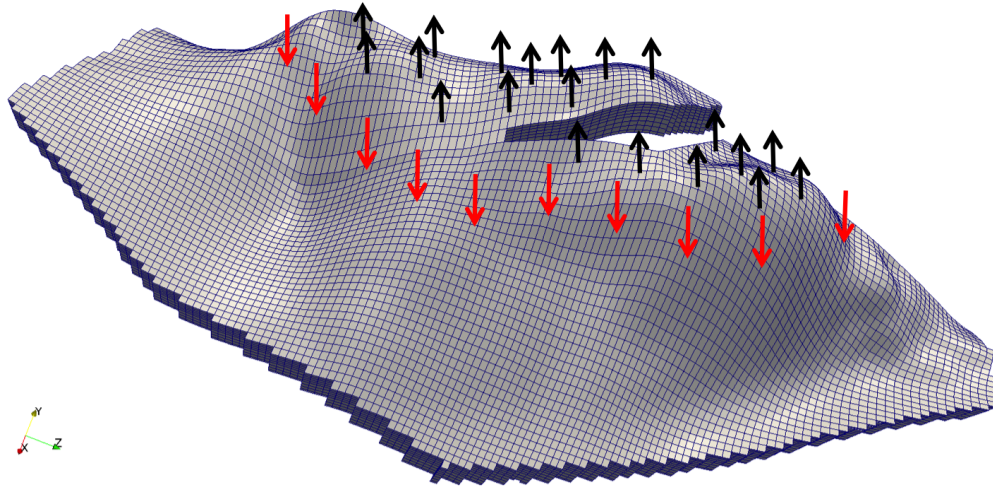


Figure 4.8: Brugge field geometry with well locations.

and capillary pressure curves in Figs. 4.9 and 4.10 ,respectively. A constant extrapolation is used, wherever necessary, for saturation values less than 0.2. Fig. 4.13 shows the oil and gas saturation profile after 1000 days whereas Fig. 4.14 shows the pressure distribution and concentration profiles for light (CO_2), intermediate (C_6) and heavy (C_{20}) components. A multi-contact miscible flood is achieved with miscibility occurring at the tail end of the injected gas front.

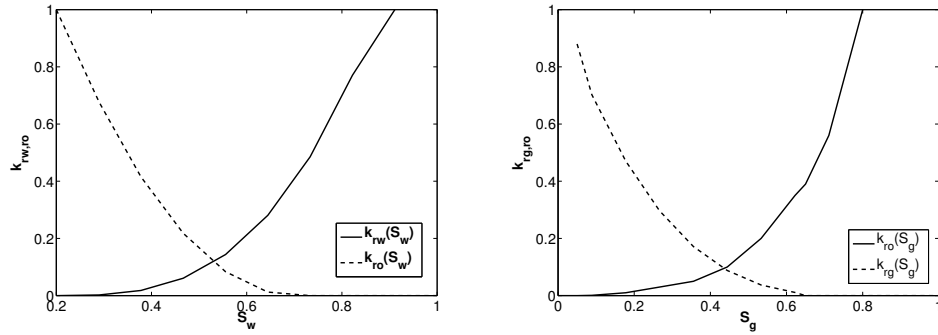


Figure 4.9: Water, oil and gas relative permeabilities.

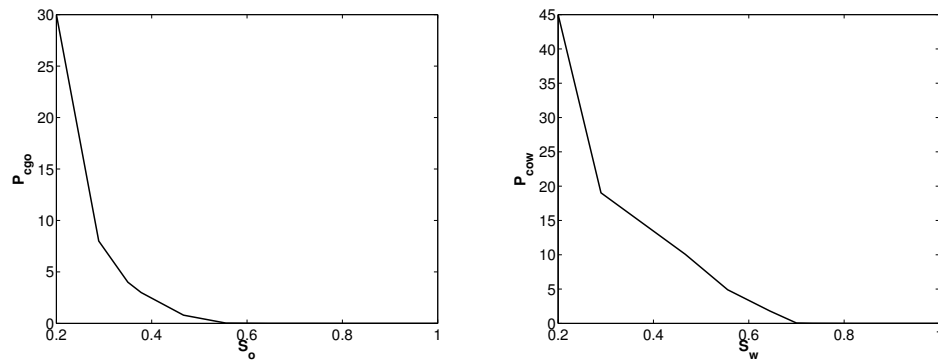


Figure 4.10: Capillary pressure curves.

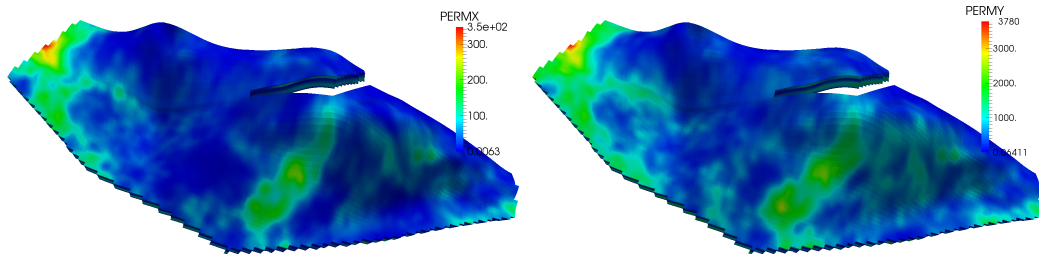


Figure 4.11: X (left) and Y (right) direction permeability fields.

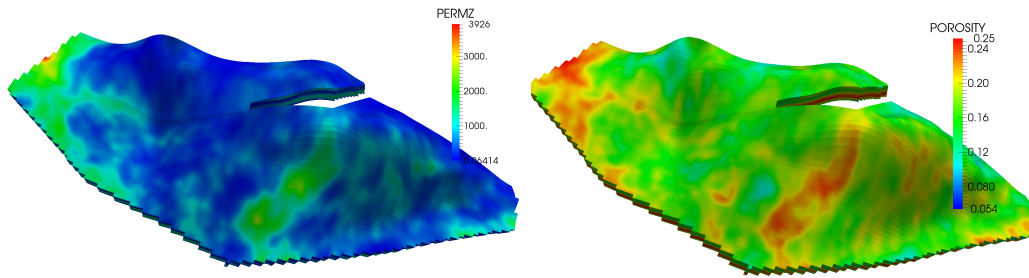


Figure 4.12: Z direction permeability (left) and porosity (right) fields.

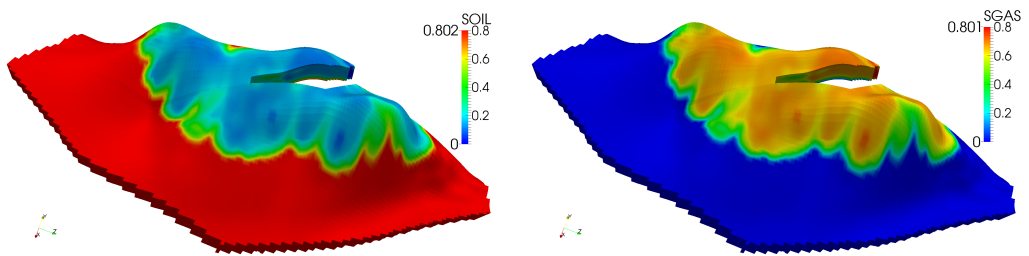


Figure 4.13: Oil and gas saturation profiles after 1000 days.

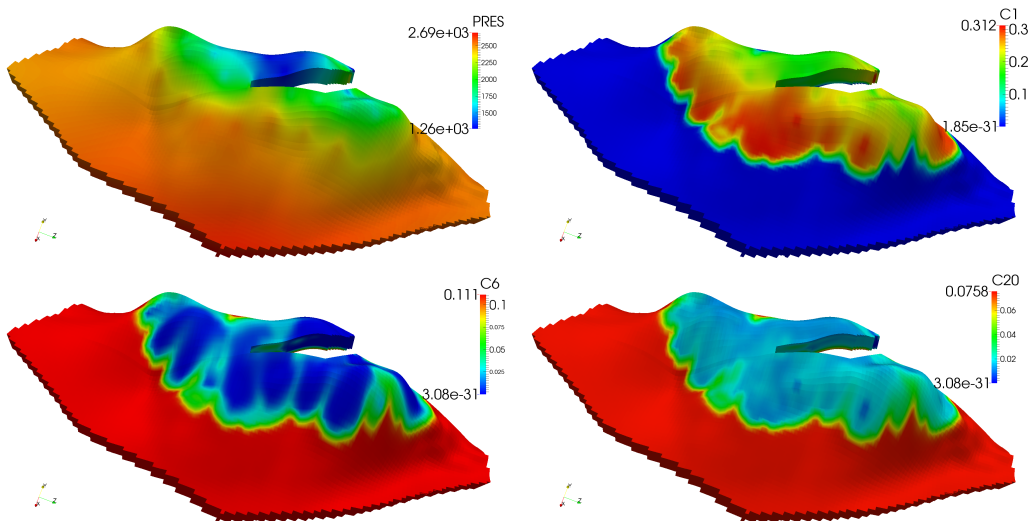


Figure 4.14: Pressure and concentration profiles after 1000 days.

Chapter 5

Coupled Two-Phase Reservoir Fracture Flow and Geomechanics Model

Multiphase flows in fractured reservoirs are of immense importance for energy security. The recovery of hydrocarbons in a reservoir is strongly dependent on the fractures, both natural and artificial. To model these processes, it is imperative to have a reliable model that captures the effects of these fractures with high accuracy. Moreover, the geometric complexities of the fractures require sophisticated numerical approaches. Further the pore pressure from the flow may also cause geomechanical effects. These effects are more pronounced when the fractures are present. The geomechanical effects and multiphase flows in a fractured porous medium are modeled by coupled nonlinear system of differential equations. Additionally, we need to account properly for reservoir heterogeneities due to discontinuous rock properties. This manifests in the form of discontinuous changes in absolute permeability, relative permeability and capillary pressure curves. The simulation of this system presents

This work has been partly presented at the SPE Hydraulic Fracturing Technology conference (Singh et al. (2014b)) and also published as an ICES report (Singh et al. (2014c)). The research is done primarily by Gurpreet Singh under the supervision of Prof. Mary F. Wheeler with the help of constant inputs, suggestions and improvements by Drs. Gergina Pencheva, Kundan Kumar, Thomas Wick and Benjamin Ganis.

important challenges from both modeling and computational points of view.

In this work, we perform a quantitative and qualitative study of these effects and describe a numerical approach for solving this problem. Our approach offers high accuracy and fidelity in capturing the physics of the problem. The model consists of two parts: geomechanics and flow equations. The flow equations in fractured reservoirs have been a subject of intensive study by several authors. Our approach fully resolves the flow by considering separate equations for the fractures and reservoirs which are coupled together. As we shall see later in this section (see **Fig 5.2**), this resolution of fracture flow is important as a crude approximation may lead to unacceptable errors. The fracture flow model is formulated by reducing a higher dimensional (\mathbb{R}^d) model to a lower dimensional (\mathbb{R}^{d-1}) manifold by averaging procedure. The derivation of this reduction procedure has been undertaken by Martin et al. (2005) and Frih et al. (2008) for Darcy and Forchheimer flows. The reduction leads to a set of equations defined for both fractures and reservoirs with fractures acting as interfaces inside the reservoirs. The purview of these studies is however limited to single phase flow accounting for permeability heterogeneity at the reservoir-fracture interface. We will follow a similar approach here for multiphase flows.

We begin by reviewing some of the work that is relevant to our presented approach. Hoteit and Firoozabadi (2008a) present a introduction of different finite volume and finite element based discretizations for such problems. A mixed finite element for multiphase, reservoir-fracture flow model

was proposed by Hoteit and Firoozabadi (2005, 2006) assuming a cross-flow equilibrium across reservoir-fracture interface. This assumption was later removed (Hoteit and Firoozabadi (2008b)) by considering additional degrees of freedom at the interface. Here, they consider a hybrid mixed method to solve an implicit pressure equation along with a higher order discontinuous Galerkin method with a slope limiter for an explicit saturation update following an IMPES (implicit pressure explicit saturation) scheme. Further, Grillo et al. (2010) discuss density driven flows where fractures are represented as 2 and 3-dimensional manifolds assuming a multi-component, single-phase flow system. A finite-volume based numerical discretization is used, with each fracture having two degrees of freedom. Our method is inspired by Hoteit and Firoozabadi (2008a) and uses mixed finite element methods and an IMPES solution scheme. We differ in the usage of a multipoint flux scheme based upon an appropriate choice of finite element spaces and quadrature rule (Ingram et al. (2010), Wheeler and Yotov (2006), Arbogast et al. (1997), Wheeler et al. (2011c)). This approach provides flexibilities in capturing the complex geometric features of fractures.

Earlier, a finite-volume based approach was presented by Bastian et al. (2000) and Monteagudo and Firoozabadi (2004) on unstructured grids. The reservoir-fracture interfaces have only one pressure and saturation degree of freedom and thus jumps in these quantities cannot be considered, thereby assuming a cross-flow equilibrium. Their model takes into account capillary pressure discontinuity due to rock heterogeneity. However, saturation calcula-

tion at the interface requires inversion of capillary pressure, which may pose problems if the capillary pressure curve is either identically zero or has a small gradient. Monteagudo and Firoozabadi (2007) address this issue by using two different formulations based upon threshold values requiring calibration. More recently, a coupled flow in a fractured-reservoir models is considered in Al-Hinai et al. (2013) where different discretization schemes were utilized inside the fracture (mimetic finite difference) and reservoir (mixed finite element) in the absence of capillary pressure and time invariant fracture permeabilities.

The geomechanical effects in the reservoir are accounted for by considering an elastic deformable medium. The theoretical groundwork for one-dimensional flow in a deformable porous medium was first developed by Terzaghi (1943). This was later extended to a general theory of three-dimensional consolidation for anisotropic and heterogeneous materials by Biot in his subsequent works (Biot (1941a,d, 1955a)). For the coupling of multiphase flow and geomechanics, Settari and Walters (2001) categorize the various schemes as decoupled and explicit, iterative and fully coupled. An explicit or loose coupling has lower computational time with little control on solution accuracy. Further, a time-step size guidance is often required for the geomechanics solve, which is empirical or heuristic in nature (Dean et al. (2006)). On the other hand, a fully implicit method is both accurate and stable, however solving the implicit system of equations results in a complex nonlinear system requiring suitable linearization schemes and specialized linear solvers for convergence. In this work, we apply an iterative coupling scheme based on fixed stress splitting

for which convergence analysis has been presented by Mikelic and Wheeler (2012); Mikelic et al. (2014); Kim et al. (2012). The analysis shows that the iterative scheme converges geometrically. An iterative coupling approach combines the advantages of both methods while maintaining numerical solution accuracy, fast convergence, and ease of implementation in existing legacy flow simulators.

The poroelastic models rely upon pore-pressure to account for changes in material stress. Accuracy of flow models, especially in capturing sharp pressure changes across a reservoir-fracture interface, plays a pivotal role when poroelastic behavior of reservoir and fracture mechanics comes into play. For a single phase flow, Ganis et al. (2013) presents a coupled flow model fractures in a poroelastic medium. The multipoint flux mixed finite element method (MFMFE) used in this work is defined for general hexahedral grids with non-planar edges. This allows non-planar fracture geometry to be captured. A detailed numerical analysis for single phase reservoir-fracture flow coupling presented here can be found in Girault et al. (2013).

There are several novelties in this work. We use hexahedral grids with an MFMFE scheme which allows non-planar fractures and an accurate computation of a locally mass-conservative flow profile. Secondly, we resolve the flow equations for both the fractures and reservoir in a coupled manner. This is achieved by assuming a lubrication equation (Reynolds (1886)) inside the fractures and multiphase Darcy law for the reservoir. Thirdly, the fixed stress splitting scheme for the geomechanics effects in a reservoir has been extended

to include fractures where the permeabilities of the fracture are functions of the deformations. Furthermore, our numerical results have been compared with physical core-scale experiments and benchmark problems demonstrating the capabilities of our approach.

We begin with a simplified 2D example to qualitatively outline some of the differences between conventional modeling techniques and the approach presented here. This is followed by a reservoir-fracture flow and geomechanics model formulation with a brief description of conservation and constitutive equations along with the required closure conditions. We then discuss a choice of boundary, interface and initial conditions used to describe the problem. Next in the algorithm and discretization section we briefly outline the spatial and temporal discretization schemes used for flow and mechanics as well as the iterative schemes used to couple the various systems of equations. Finally, in the results section we present five numerical experiments including a comparison with experimental lab results to confirm the validity of our model and to further demonstrate the features and long-term prediction capabilities.

5.1 An Illustrative Example

In this section, we motivate this work by emphasizing the need to fully resolve the fracture geometry. The following simplified example underlines the need for a detailed modeling. This will be achieved by considering and comparing different approaches for fractured reservoir flow modeling. A reservoir domain of size 10 ft \times 10 ft is considered with bottom-hole pressure specified

injection (520 psi) and production (500 psi) wells located at diagonally opposite ends. Further, a homogeneous and isotropic reservoir permeability of 5 mD and porosity of 0.2 are assumed.

Fig. 5.2 shows saturation profiles for three approaches: (1) an average permeability representation (1st row, 1st column), where the dotted red region has been assigned higher average permeability of 5×10^6 mD assuming the fracture goes through those blocks, (2) a meshed-in representation where the fracture itself is gridded (1st row, 2nd column) and has a permeability value of 5×10^{10} mD, and finally, (3) the interface approach presented in this work (1st row, 3rd column) where the fracture is represented as a lower dimensional manifold shown by the red dotted line. Further, the capillary pressure is taken to be identically zero everywhere. The relative permeability curves are shown in Fig. 5.1.

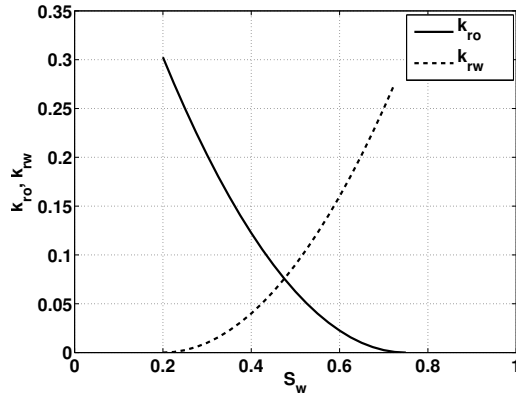


Figure 5.1: Oil and water phase relative permeability curves for reservoir and fracture.

The fracture aperture is chosen such that the fracture conductivity is same as high permeability for the meshed in approach. Note that an actual fracture width of 1 mm is used for the interface approach when compared to the meshed-in approach where the grid-block width normal to the fracture surface is 1cm. The saturation profiles at $t = 50$ and 100 days (2nd and 3rd row in Fig. 5.2) shows differences in sweep pattern for the different approaches.

The averaging approach mobilizes additional fluid resulting in overestimation of recoveries. The meshed-in approach, although more accurate, poses a few challenges. A mesh refinement is required to capture the fracture, which may not always be possible. Furthermore, a time-step size restriction due to an order of magnitude difference between fracture and reservoir grid block sizes is observed. A relatively large fracture width (1cm) has been chosen due to time-step size restriction imposed by CFL (Courant-Friedrichs-Lewy) condition. The interface approach overcomes these issues while preserving the physics. Fig. 5.2 (2nd row 3rd column) shows fluid entering fracture at one end and leaving at the other end without mobilizing additional fluid in between. In the numerical results section, we further elaborate on the merits and the limitations of the averaging approach. We also show that the orientation and location of fractures are important parameters in determining the choice of fracture modeling.

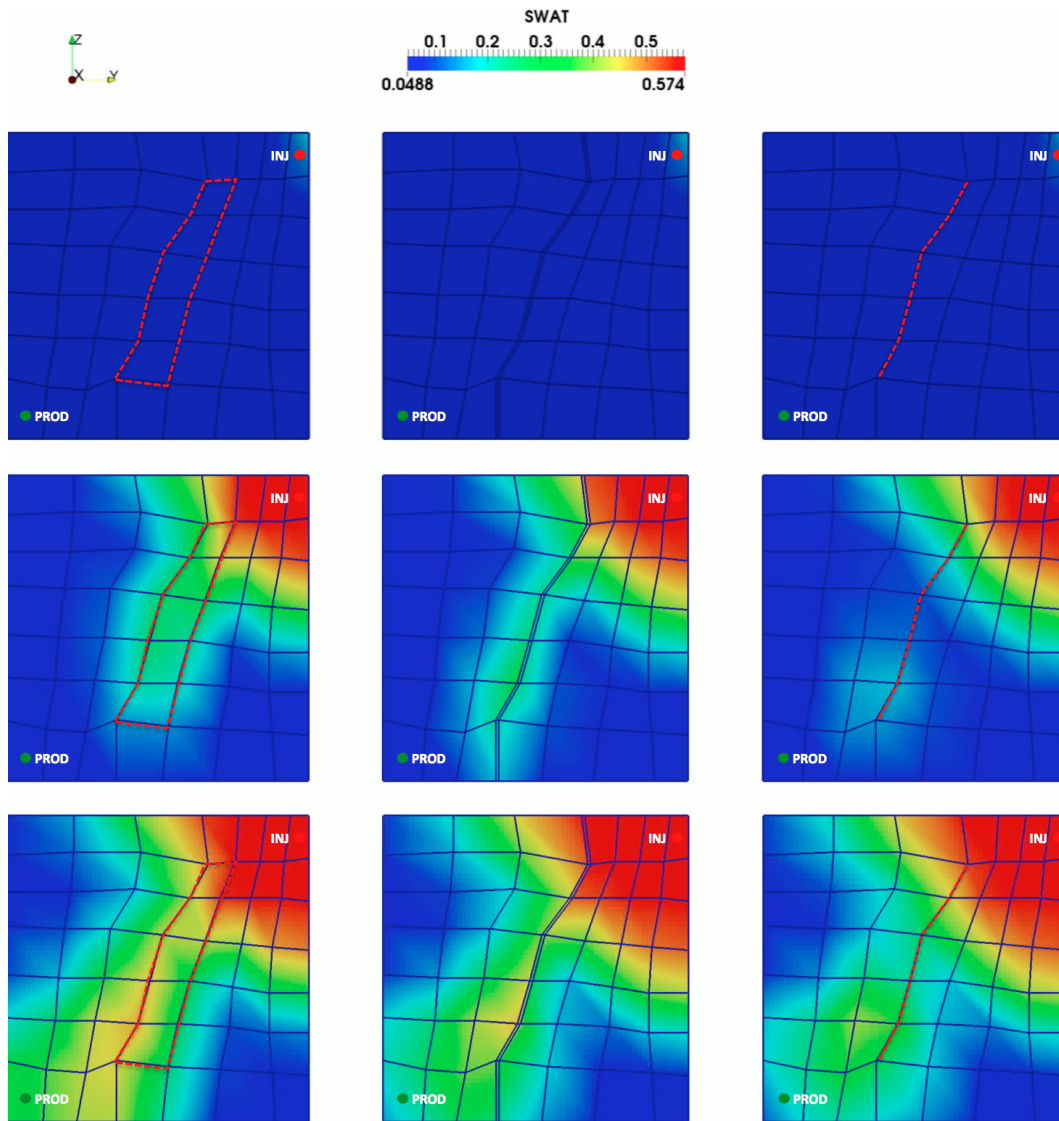


Figure 5.2: Saturation profiles for averaging, meshed-in and interface approaches (left to right) for time $t = 0, 50$ and 100 days (top to bottom).

5.2 Model Formulation

In this section, we provide a brief description of the fractured reservoir flow and geomechanics model where fractures are treated as lower dimensional manifolds in (\mathbb{R}^{d-1}) in a reservoir domain $\Omega \in \mathbb{R}^d$, ($d = 2$ or 3). The model has two components: two-phase flow and mechanics. The modeling equations are defined separately in the reservoir and on the fracture surfaces along with the associated interface conditions. For the flow model, a slightly compressible, two-phase, locally mass conservative Darcy flow is assumed for the reservoir domain and a lubrication equation for the fractures. We further assume oil and water are the two phases denoted by subscripts o and w , respectively. A schematic of a fractured reservoir is shown in Fig. 5.3. Note that the fracture geometry is not necessarily planar and as explained later, our numerical method allows for non-planar geometries.

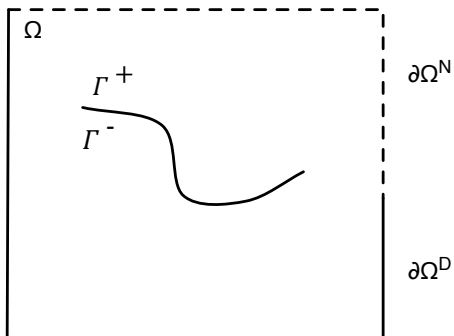


Figure 5.3: Schematic of a fractured reservoir flow model.

We treat the fracture as a pressure specified internal boundary in the reservoir domain and provide the jump in flux across this interface as a leakage

term to the fracture. The fracture pressure is also treated as an internal traction boundary condition for the reservoir geomechanics. The resulting jump in displacements (fracture width or aperture) is used to calculate fracture permeability. For the model description, we consider a fractured reservoir domain (Ω) where the fracture is represented as an interface (Γ) with two surfaces (Γ^\pm), as shown in Fig. 5.3. Here $\partial\Omega^N$ and $\partial\Omega^D$ represent the Neumann and Dirichlet parts, respectively of the external boundary of the reservoir domain Ω .

5.2.1 Equations in the reservoir ($\Omega \setminus \Gamma$)

We begin by describing the flow equations everywhere except for the fracture interface Γ .

5.2.1.1 Flow equations

The mass-conservation equation for the phase β reads,

$$\frac{\partial}{\partial t} (\phi^* S_\beta \rho_\beta) + \nabla \cdot \mathbf{z}_\beta = q_\beta. \quad (5.1)$$

Here, ϕ^* is the fluid fraction, S_β the saturation, ρ_β the density, \mathbf{z}_β the flux of phase $\beta = o$ (oil phase), w (water phase). The source/sink term q_β is treated using an appropriate well model (Peaceman (1978)). The Darcy equation relates the flux \mathbf{z}_β to the gradient of the phase pressure and is given by

$$\mathbf{z}_\beta = -\mathbf{K} \rho_\beta \frac{k_{r\beta}}{\nu_\beta} (\nabla p_\beta - \rho_\beta \mathbf{g}). \quad (5.2)$$

In the above, \mathbf{K} is a full tensor absolute permeability, $k_{r\beta}$ the relative permeability, and ν_β the viscosity of phase β . The second term in the parenthesis models the effect of gravity.

5.2.1.2 Mechanics

The displacement \mathbf{u} of the porous medium is described by the quasi-static poroelastic equations. Eqn. (5.3) represents the momentum conservation (force balance) and Eqn. (5.4) the constitutive equation relating stress ($\boldsymbol{\sigma}^{por}$) and displacements (\mathbf{u}):

$$-\nabla \cdot \boldsymbol{\sigma}^{por}(\mathbf{u}, p_{ref}) = \mathbf{f}, \quad (5.3a)$$

$$\mathbf{f} = \left[\rho_s(1 - \phi^*) + \phi^* \sum_{\beta} \rho_{\beta} S_{\beta} \right] \mathbf{g}, \quad (5.3b)$$

$$\phi^* = \phi_o + \alpha \nabla \cdot \mathbf{u} + \frac{1}{M} p_{ref}. \quad (5.3c)$$

$$\boldsymbol{\sigma}^{por}(\mathbf{u}, p_{ref}) = \boldsymbol{\sigma}(\mathbf{u}) - \alpha p_{ref} \mathbf{I}, \quad (5.4a)$$

$$\boldsymbol{\sigma}(\mathbf{u}) = \lambda(\nabla \cdot \mathbf{u}) \mathbf{I} + 2\mu \boldsymbol{\varepsilon}(\mathbf{u}), \quad (5.4b)$$

$$\boldsymbol{\varepsilon}(\mathbf{u}) = \frac{1}{2}(\nabla \mathbf{u} + \nabla \mathbf{u}^T). \quad (5.4c)$$

Here, $\boldsymbol{\sigma}^{por}$ is the Cauchy stress tensor, $\boldsymbol{\varepsilon}$ the strain tensor, \mathbf{f} the body force, ρ_s density of the solid matrix, \mathbf{g} acceleration due to gravity, α the Biot coefficient, p_{ref} the reference phase pressure, \mathbf{I} the identity matrix, ϕ_o the reference porosity, μ and λ are Lamé parameters.

5.2.2 Equations in the fracture (Γ)

A lubrication equation is assumed as the constitutive relation between fracture fluxes (\mathbf{z}_β^Γ) and gradient of fracture pressure (p^Γ). Here, the fracture gradient ($\bar{\nabla}$) and divergence ($\bar{\nabla} \cdot$) operators are defined on a lower dimensional space (\mathbb{R}^{d-1}). Eqns. (5.5) and (5.6) represent the mass conservation and Darcy's law for the phase ' β ' in the fracture domain:

$$\frac{\partial}{\partial t} (\mathcal{W} S_\beta^\Gamma \rho_\beta^\Gamma) + \mathcal{W} \bar{\nabla} \cdot \mathbf{z}_\beta^\Gamma = q_\beta^\Gamma + q_{l\beta}, \quad (5.5)$$

$$\mathbf{z}_\beta^\Gamma = -\mathbf{K}^\Gamma \rho_\beta^\Gamma \frac{k_{r\beta}}{\nu_\beta} (\bar{\nabla} p_\beta^\Gamma - \rho_\beta^\Gamma \mathbf{g}). \quad (5.6)$$

Here, $q_{l\beta}$ is the fracture leakage term as defined below. The absolute permeability \mathbf{K}^Γ is given by Eqn. (5.7) where (\mathcal{W}) is the fracture width,

$$\mathbf{K}^\Gamma = \frac{\mathcal{W}^2}{12}. \quad (5.7)$$

5.2.3 Closure conditions

A slightly compressible, equation of state relating fluid densities and pressures is assumed (Eqn. (5.8)) for both reservoir and fracture. Further, the capillary pressure and saturation constraints are given by Eqns. (5.9) and (5.10), respectively. For simplicity of notation we let $\star = \Omega \setminus \Gamma$ or Γ and for a given function $f^{\Omega \setminus \Gamma}$ to be equal to f . Thus, we have

$$\rho_\beta^\star = \rho_{\beta 0} \exp [c_\beta (p_{\text{ref}}^\star + p_{c\beta}^\star - p_0)], \quad (5.8)$$

$$p_{c\beta}^\star(S_\beta^\star) = p_o^\star - p_w^\star, \quad (5.9)$$

$$S_w^* + S_o^* = 1. \quad (5.10)$$

Here, c_β is the fluid compressibility, $p_{c\beta}$ the capillary pressure for the fluid phase β and S_{ref} the reference phase saturation. The relative permeabilities are continuous functions of reference phase saturation (S_{ref}) for both reservoir and fracture. A more general table based capillary pressure and relative permeability curve description has also been implemented.

5.2.4 Boundary, interface and initial conditions

For the sake of simplicity, we consider no-flow or pressure specified external boundary conditions for the reservoir domain (Ω);

$$\mathbf{z}_\beta \cdot \mathbf{n} = 0 \text{ on } \partial\Omega^N. \quad (5.11)$$

For saturations, we specify Dirichlet boundary conditions on $\partial\Omega^D$. However, the choice is not restrictive and is used for convenience. That is,

$$\begin{aligned} p_{\text{ref}} &= p^D \text{ on } \partial\Omega^D, \\ S_{\text{ref}} &= S^D \text{ on } \partial\Omega^D. \end{aligned} \quad (5.12)$$

Furthermore, the proposed model assumes a pressure-specified internal boundary condition (Eqn. (5.13)) given by,

$$p_{\text{ref}} = p^D \text{ on } \Gamma^\pm. \quad (5.13)$$

Assuming capillary pressure functions are monotone functions whenever uniformly non-zero and therefore invertible, three modeling choices are considered.

5.2.4.1 Case I

p_c is identically equal to zero everywhere:

$$S_{\text{ref}} = S^D \quad \text{on } \Gamma^\pm. \quad (5.14)$$

5.2.4.2 Case II

p_c is strictly greater than zero everywhere:

$$\begin{aligned} S_{\text{ref}}^- &= (p_{c,\text{ref}}^-)^{-1}(p_{c,\text{ref}}^\Gamma(S_{\text{ref}}^\Gamma)) \quad \text{on } \Gamma^- , \\ S_{\text{ref}}^+ &= (p_{c,\text{ref}}^+)^{-1}(p_{c,\text{ref}}^\Gamma(S_{\text{ref}}^\Gamma)) \quad \text{on } \Gamma^+ . \end{aligned} \quad (5.15)$$

5.2.4.3 Case III

p_c is strictly greater than zero in the reservoir and identically equal to zero in the fracture:

$$\begin{aligned} S_{\text{ref}}^- &= (p_{c,\text{ref}}^-)^{-1}(0) \quad \text{on } \Gamma^- , \\ S_{\text{ref}}^+ &= (p_{c,\text{ref}}^+)^{-1}(0) \quad \text{on } \Gamma^+ . \end{aligned} \quad (5.16)$$

Here $(p_{c\beta}^\pm)^{-1}$ is the inverse of capillary pressure on top and bottom (or left and right) surfaces of the fracture. Note that fluid mass exchange between reservoir and fracture is accounted for by the leakage term ' $q_{l\beta}$ ' in Eqn. (5.5). Assuming the two fracture surfaces have the same normal, a jump in reservoir fluxes and displacements across the fracture interface (Γ^\pm) is provided as a leakage (source term) and fracture width, respectively to the fracture mass conservation:

$$q_{l\beta} = [\mathbf{z}_\beta \cdot \mathbf{n}]^\Gamma = \mathbf{z}_\beta \cdot \mathbf{n}|_{\Gamma^-} - \mathbf{z}_\beta \cdot \mathbf{n}|_{\Gamma^+}, \quad (5.17a)$$

$$\mathcal{W} = [\mathbf{u} \cdot \mathbf{n}]^\Gamma = \mathbf{u} \cdot \mathbf{n}|_{\Gamma^-} - \mathbf{u} \cdot \mathbf{n}|_{\Gamma^+}. \quad (5.17b)$$

The geomechanics boundary conditions are given by

$$(\boldsymbol{\sigma}^{\text{por}}(\mathbf{u}, p)\mathbf{n})_{\Gamma^\pm} = -p_{\text{ref}}^\Gamma \mathbf{n}, \quad (5.18a)$$

$$[\boldsymbol{\sigma}^{\text{por}}(\mathbf{u}, p)\mathbf{n}]_\Gamma = 0, \quad (5.18b)$$

$$\mathbf{u} = 0 \text{ on } \partial\Omega_s^D, \quad (5.18c)$$

$$\boldsymbol{\sigma}^{\text{por}}\mathbf{n} = \boldsymbol{\sigma}^N \text{ on } \partial\Omega_s^N, \quad (5.18d)$$

where $\partial\Omega_s$ are the external boundaries. The initial conditions at time $t = 0$ are as follows:

$$p_{\text{ref}} = p^0, \quad (5.19)$$

$$S_{\text{ref}} = S^0, \quad (5.20)$$

$$\mathbf{u} = \mathbf{u}^0. \quad (5.21)$$

5.3 Solution Algorithm and Discretization

A fixed stress iterative coupling scheme, Settari and Walters (2001); Mikelić and Wheeler (2012), is employed as shown in Fig. 5.4. Here we iterate between the flow solution assuming a fixed stress field and the mechanics solution assuming fixed pressure and saturation fields. For the reservoir geomechanics equations, a continuous Galerkin (CG) finite element method used for spatial discretization. The mechanics solve provides a jump in displacements across the fracture interface (fracture width) which is used to calculate

the fracture permeability (Eqn. 5.7). The fracture pressure from the reservoir-fracture flow solve is then treated as a traction boundary condition for the mechanics solve. Iterations are performed until a desired tolerance ϵ_1 is achieved. Please note that the fracture widths vary both spatially and temporally. Our formulation has been extended to propagating fracture based on a phase field approach Wick et al. (2013); Mikelić et al. (2014a); Wheeler et al. (2014b)

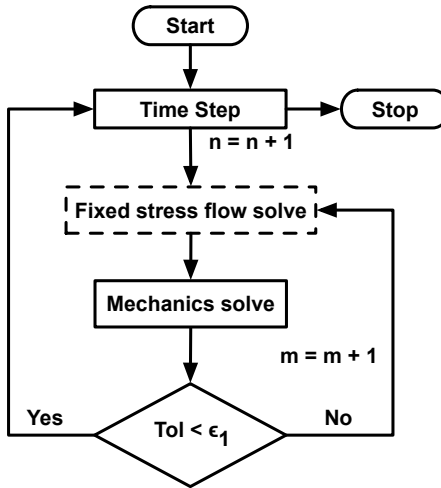


Figure 5.4: Fixed stress flow and mechanics coupling

The MFMFE method, developed by Wheeler and Yotov (2006) for general hexahedra, is used for spatial discretization of reservoir and fracture flow equations. Mixed finite element methods are preferred over other variational formulations due to their local mass conservation and improved flux approximation properties which includes diagonal flow across a grid-block. A 9 and 27 point pressure stencil is formed for logically rectangular 2D and 3D grids, respectively.

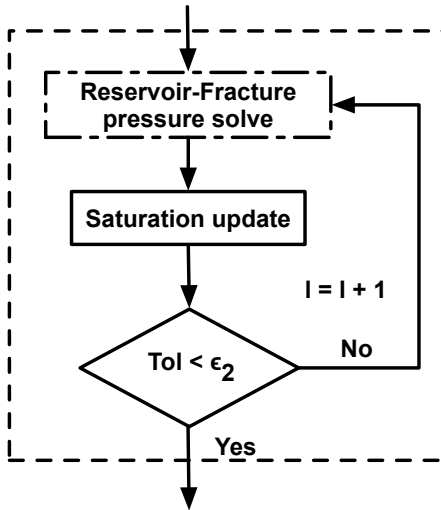


Figure 5.5: Iteratively coupled IMPES scheme

The flow equations are solved using an iteratively-coupled IMPES scheme as shown in Fig. 5.5. The reference phase pressure is solved implicitly by solving the total mass conservation equation with a backward Euler time discretization assuming the reference phase saturations are given. This is followed by an explicit update of reference phase saturations using a forward Euler time discretization for the phase mass conservation equation. The solution algorithm allows for smaller saturation time-step sizes than pressure time-steps. Further, the Courant-Frederichs-Lewy (CFL) condition on the explicit saturation updates are then obeyed using different time-step sizes for the reservoir and the fracture. The fluid property data for intermediate saturation time steps are calculated by linear interpolation of pressure. The demarcation of reservoir and fracture as separate domains allows for special treatment of

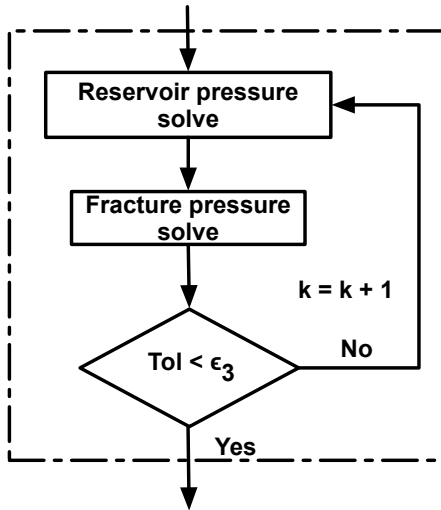


Figure 5.6: Iteratively coupled reservoir and fracture pressure solve

computationally challenging regions. Please note that since the pressures are solved implicitly, there are no restrictions on the pressure time-step size. A tolerance of ϵ_2 determines convergence of the iterative scheme.

We finally turn our attention to the non-linear, reservoir-fracture flow system. The reservoir pressure solve provides a jump in fluxes across the fracture interface. These in turn act as source/sink terms for the fracture pressure solve. The resulting fracture pressure is then treated as a pressure specified internal boundary for the reservoir domain. We couple the reservoir and fracture pressure solves by iterating between the two implicit systems until a desired tolerance ϵ_3 is reached. Fig. 5.6 provides an outline of the coupled reservoir-fracture flow model used in this work.

5.4 Iterative Coupling

In this section, we discuss the solution algorithm for the model formulation described before. A number of iterative coupling schemes can be devised based upon decoupling choice such as time or iteration lagging certain terms. We restrict ourselves to two such choices, namely the implicit and explicit schemes. The fixed stress iterative coupling (explicit coupling) of reservoir flow and geomechanics, in the absence of fracture, is known to be convergent (Mikelic and Wheeler (2012)) in the presence of a stabilization term. A similar stabilization term allows an explicit coupling of reservoir fracture pressure equations to be convergent. However, the numerical scheme was found to be very sensitive to the value of this term and therefore the numerical test, later in the results section, are based upon the implicit coupling approach.

5.4.1 Reservoir and fracture pressure coupling

The implicit coupling scheme is found to be strictly convergent for slightly compressible flow, with convergence rates dependent on the ratio of fluid compressibilities to time step size. Please note that the terms implicit and explicit are used here only to differentiate the two formulations in the sense described below. It is by no means indicative of the strict definitions associated with these two terms and is utilized to represent an implicit or explicit treatment of leakage term and internal boundary condition. Before we delve into further details, it is important to discuss some of the indices we use for representing the iterates in our numerical formulation. In the sections

below and thereafter, k is the reservoir-fracture pressure coupling iterate, l the reservoir-fracture pressure and saturation coupling iterate, m flow and mechanics coupling iterate and n the time iterate. Please note that \tilde{g} , $g = k, l$ superscript is used below to represent quantities which contain terms at both g and $g + 1$ level iterate.

5.4.1.1 Explicit coupling

The term explicit here represents an explicit treatment of the jump in fluxes $z_\beta \cdot n$ and leakage terms q_β^l for the reservoir and fracture pressure equations, respectively. A coupling is then achieved by iterating between the non-linear reservoir and fracture pressure equations, for given saturation and fracture width distributions, until a desired tolerance is achieved. A stabilization term γ_f is added to achieve convergence as will be shown in the description below. However, the numerical scheme is extremely sensitive to the values of this stabilization.

Pressure equation in $\Omega \setminus \Gamma$

$$\begin{aligned} & \sum_{\beta} \left(\frac{\phi^{*m,n+1} S_{\beta}^{l,m+1,n+1} \rho_{\beta}^{k+1,\tilde{l},m+1,n} - (\phi^* \rho_{\beta} S_{\beta})^n}{\Delta t} \right) + \gamma_{mr} p_{\text{ref}}^{m+1,n+1} \\ & + \sum_{\beta} \nabla \cdot \mathbf{z}_{\beta}^{k+1,\tilde{l},m+1,n+1} = \sum_{\beta} q_{\beta}^{k+1,\tilde{l},m+1,n+1} + \gamma_{mr} p_{\text{ref}}^{m,n+1} \end{aligned} \quad (5.22a)$$

$$\mathbf{z}_\beta^{k+1, \tilde{l}, m+1, n+1} = -\mathbf{K} \rho_\beta^{k+1, \tilde{l}, m+1, n+1} \frac{k_{r\beta}^{l, m+1, n+1}}{\nu_\beta} \left(\nabla p_{\text{ref}}^{k+1, l+1, m+1, n+1} + \nabla p_{c\beta}^{l, m+1, n+1} - \rho_\beta^{k+1, \tilde{l}, m+1, n+1} \mathbf{g} \right) \quad (5.22b)$$

$$\phi^{*m, n+1} = \phi_o + \alpha \nabla \cdot \mathbf{u}^{m, n+1} + \frac{1}{M} p_{\text{ref}}^{m, n+1} \quad (5.22c)$$

$$\rho_\beta^{k+1, \tilde{l}, m+1, n+1} = \rho_{\beta o} \left[1 + c_\beta (p_{\text{ref}}^{k+1, l+1, m+1, n+1} + p_{c\beta}^{l, m+1, n+1} - p_o) \right] \quad (5.22d)$$

Interface conditions

$$p_{\text{ref}}^{k+1, l+1, m+1, n+1} = p_{\text{ref}}^{\Gamma k, l+1, m+1, n+1} \text{ on } \Gamma^\pm \quad (5.23a)$$

$$q_{l\beta}^{k+1, \tilde{l}, m+1, n+1} = [\mathbf{z}_\beta \cdot \mathbf{n}]^{\Gamma \tilde{k}, \tilde{l}, m+1, n+1} \quad (5.23b)$$

$$\mathcal{W}^{m, n+1} = [\mathbf{u} \cdot \mathbf{n}]^{m, n+1} \quad (5.23c)$$

Pressure equation in Γ

$$\begin{aligned} & \sum_\beta \left(\frac{\mathcal{W}^{m, n+1} S_\beta^{\Gamma l, m+1, n+1} \rho_\beta^{\Gamma k+1, \tilde{l}, m+1, n} - (\mathcal{W} S_\beta^\Gamma \rho_\beta^\Gamma)^n}{\Delta t} \right) + \gamma_f p_{\text{ref}}^{\Gamma k+1, l+1, m+1, n+1} \\ & + \gamma_{mf} p_{\text{ref}}^{m+1, n+1} + \sum_\beta \mathcal{W} \bar{\nabla} \cdot \mathbf{z}_\beta^{\Gamma k+1, \tilde{l}, \tilde{m}, n+1} = \sum_\beta \left(q_\beta^{\Gamma k+1, \tilde{l}, m+1, n+1} + q_{l\beta}^{k+1, \tilde{l}, m+1, n+1} \right) \\ & + \gamma_f p_{\text{ref}}^{\Gamma k, l+1, m+1, n+1} + \gamma_{mf} p_{\text{ref}}^{m, n+1} \end{aligned} \quad (5.24a)$$

$$\mathbf{z}_\beta^{\Gamma k+1, \tilde{l}, \tilde{m}, n+1} = - \left(\frac{\mathcal{W}^2}{12} \right)^{m, n+1} \rho_\beta^{\Gamma k+1, \tilde{l}, m+1, n+1} \frac{k_{r\beta}^{\Gamma l, m+1, n+1}}{\nu_\beta} \left(\nabla p_{\text{ref}}^{\Gamma k+1, l+1, m+1, n+1} + \nabla p_{c\beta}^{\Gamma l, m+1, n+1} - \rho_\beta^{\Gamma k+1, \tilde{l}, m+1, n+1} \mathbf{g} \right) \quad (5.24b)$$

$$\rho_\beta^{\Gamma k+1, \tilde{l}, m+1, n+1} = \rho_{\beta 0} \left[1 + c_\beta (p_{\text{ref}}^{\Gamma k+1, l+1, m+1, n+1} + p_{c\beta}^{\Gamma l, m+1, n+1} - p_0) \right] \quad (5.24c)$$

5.4.1.2 Implicit Coupling

Contrary to explicit coupling an implicit treatment of jump in fluxes and leakage term results in an implicit coupling scheme. Iterations between the linearized reservoir and fracture pressure systems are performed until a desired linear tolerance is achieved. This is followed by a Newton update and will be described later in the linearization section.

Pressure equation in $\Omega \setminus \Gamma$

$$\begin{aligned} & \sum_{\beta} \left(\frac{\phi^{*m, n+1} S_{\beta}^{l, m+1, n+1} \rho_{\beta}^{k+1, \tilde{l}, m+1, n} - (\phi^* \rho_{\beta} S_{\beta})^n}{\Delta t} \right) + \gamma_{mr} p_{\text{ref}}^{m+1, n+1} \\ & + \sum_{\beta} \nabla \cdot \mathbf{z}_{\beta}^{k+1, \tilde{l}, m+1, n+1} = \sum_{\beta} q_{\beta}^{k+1, \tilde{l}, m+1, n+1} + \gamma_{mr} p_{\text{ref}}^{m, n+1} \end{aligned} \quad (5.25a)$$

$$\begin{aligned} \mathbf{z}_{\beta}^{k+1, \tilde{l}, m+1, n+1} = & -\mathbf{K} \rho_{\beta}^{k+1, \tilde{l}, m+1, n+1} \frac{k_{r\beta}^{l, m+1, n+1}}{\nu_{\beta}} \left(\nabla p_{\text{ref}}^{k+1, l+1, m+1, n+1} \right. \\ & \left. + \nabla p_{c\beta}^{l, m+1, n+1} - \rho_{\beta}^{k+1, \tilde{l}, m+1, n+1} \mathbf{g} \right) \end{aligned} \quad (5.25b)$$

$$\phi^{*m, n+1} = \phi_o + \alpha \nabla \cdot \mathbf{u}^{m, n+1} + \frac{1}{M} p_{\text{ref}}^{m, n+1} \quad (5.25c)$$

$$\rho_{\beta}^{k+1, \tilde{l}, m+1, n+1} = \rho_{\beta 0} \left[1 + c_{\beta} (p_{\text{ref}}^{k+1, l+1, m+1, n+1} + p_{c\beta}^{l, m+1, n+1} - p_0) \right] \quad (5.25d)$$

Interface conditions

$$p_{\text{ref}}^{k+1, l+1, m+1, n+1} = p_{\text{ref}}^{\Gamma k+1, l+1, m+1, n+1} \text{ on } \Gamma^{\pm} \quad (5.26a)$$

$$q_{l\beta}^{k+1, \tilde{l}, m+1, n+1} = [\mathbf{z}_\beta \cdot \mathbf{n}]^{\Gamma k+1, \tilde{l}, m+1, n+1} \quad (5.26b)$$

$$\mathcal{W}^{m, n+1} = [\mathbf{u} \cdot \mathbf{n}]^{m, n+1} \quad (5.26c)$$

Pressure equation in Γ

$$\begin{aligned} & \sum_{\beta} \left(\frac{\mathcal{W}^{m, n+1} S_{\beta}^{\Gamma l, m+1, n+1} \rho_{\beta}^{\Gamma k+1, \tilde{l}, m+1, n} - (\mathcal{W} S_{\beta}^{\Gamma} \rho_{\beta}^{\Gamma})^n}{\Delta t} \right) + \gamma_{mf} p_{\text{ref}}^{\Gamma m+1, n+1} \\ & + \sum_{\beta} \mathcal{W} \bar{\nabla} \cdot \mathbf{z}_{\beta}^{\Gamma k+1, \tilde{l}, \tilde{m}, n+1} = \sum_{\beta} \left(q_{\beta}^{\Gamma k+1, \tilde{l}, m+1, n+1} + q_{l\beta}^{k+1, \tilde{l}, m+1, n+1} \right) + \gamma_{mf} p_{\text{ref}}^{\Gamma m, n+1} \end{aligned} \quad (5.27a)$$

$$\begin{aligned} \mathbf{z}_{\beta}^{\Gamma k+1, \tilde{l}, \tilde{m}, n+1} = - \left(\frac{\mathcal{W}^2}{12} \right)^{m, n+1} & \rho_{\beta}^{\Gamma k+1, \tilde{l}, m+1, n+1} \frac{k_{r\beta}^{\Gamma l, m+1, n+1}}{\nu_{\beta}} \left(\nabla p_{\text{ref}}^{\Gamma k+1, l+1, m+1, n+1} \right. \\ & \left. + \nabla p_{c\beta}^{\Gamma l, m+1, n+1} - \rho_{\beta}^{\Gamma k+1, \tilde{l}, m+1, n+1} \mathbf{g} \right) \end{aligned} \quad (5.27b)$$

$$\rho_{\beta}^{\Gamma k+1, \tilde{l}, m+1, n+1} = \rho_{\beta 0} \left[1 + c_{\beta} (p_{\text{ref}}^{\Gamma k+1, l+1, m+1, n+1} + p_{c\beta}^{\Gamma l, m+1, n+1} - p_0) \right] \quad (5.27c)$$

5.4.2 Pressure and saturation coupling

A number of saturation timesteps are taken in order to alleviate time-step size constraint imposed by the CFL criteria. The residual calculation and convergence criteria is different from when compared to a fully implicit method given in appendix. The iterative coupling steps decrease as the number of saturation timesteps are increased, which is consistent with the expected behavior. Please note that the saturation timestep is different from the pressure

timestep represented by iterates ‘l’ and ‘n’, respectively. The residual calculation for multiple saturation timesteps utilize interpolated fluxes as opposed to residuals based upon fluxes at timestep ‘n+1’.

Saturation equation in $\Omega \setminus \Gamma$

$$\frac{\partial}{\partial t} \phi^* S_{\text{ref}} \rho_{\text{ref}} + \nabla \cdot \mathbf{z}_{\text{ref}} = q_{\text{ref}} \quad (5.28)$$

$$\frac{\left(\phi^{m,n+1} S_{\text{ref}}^{l+1,m+1,n+1} \rho_{\text{ref}}^{\tilde{l},m+1,n+1} \right) - \left(\phi^* S_{\text{ref}} \rho_{\text{ref}} \right)^n}{\Delta t} + \nabla \cdot \mathbf{z}_{\text{ref}}^{\tilde{l},m+1,n+1} = q_{\text{ref}}^{\tilde{l},m+1,n+1} \quad (5.29a)$$

$$\mathbf{z}_{\text{ref}}^{\tilde{l},m+1,n+1} = -\mathbf{K} \rho_{\text{ref}}^{\tilde{l},m+1,n+1} \frac{k_{\text{rref}}^{l,m+1,n+1}}{\nu_{\text{ref}}} \left(\nabla p_{\text{ref}}^{l+1,m+1,n+1} + \nabla p_{\text{cref}}^{l,m+1,n+1} - \rho_{\text{ref}}^{\tilde{l},m+1,n+1} \mathbf{g} \right) \quad (5.29b)$$

$$\rho_{\text{ref}}^{\tilde{l},m+1,n+1} = \rho_{\text{ref}0} \left[1 + c_{\text{ref}} (p_{\text{ref}}^{l+1,m+1,n+1} + p_{\text{cref}}^{l,m+1,n+1} - p_0) \right] \quad (5.29c)$$

$$a^{0,m+1,n+1} = a^{m,n+1}, \quad a = p_{\text{ref}}, \mathbf{u}$$

$$a^{0,0,n+1} = a^n \quad (5.30)$$

$$b^{0,n+1} = b^n, \quad b = S_{\text{ref}}$$

Saturation equation in Γ

$$\frac{\partial}{\partial t} \mathcal{W} S_{\text{ref}}^{\Gamma} \rho_{\text{ref}}^{\Gamma} + \mathcal{W} \bar{\nabla} \cdot \mathbf{z}_{\text{ref}}^{\Gamma} = q_{\text{ref}}^{\Gamma} + q_{\text{lref}} \quad (5.31)$$

$$\begin{aligned}
& \frac{\left(\mathcal{W}^{m,n+1} S_{\text{ref}}^{\Gamma l+1,m+1,n+1} \rho_{\text{ref}}^{\tilde{\Gamma} l,m+1,n+1} \right) - \left(\mathcal{W} S_{\text{ref}}^{\Gamma} \rho_{\text{ref}}^{\Gamma} \right)^n}{\Delta t} + w^{m,n+1} \bar{\nabla} \cdot \mathbf{z}_{\text{ref}}^{\tilde{\Gamma} l,m+1,n+1} \\
& = (q_{\text{ref}} + q_{l\text{ref}})^{\tilde{\Gamma} l,m+1,n+1}
\end{aligned} \tag{5.32a}$$

$$\begin{aligned}
\mathbf{z}_{\text{ref}}^{\tilde{\Gamma} l,m+1,n+1} = & -\mathbf{K}^{\Gamma} \rho_{\text{ref}}^{\tilde{\Gamma} l,m+1,n+1} \frac{k_{r\text{ref}}^{\Gamma l,m+1,n+1}}{\nu_{\text{ref}}} \left(\nabla p_{\text{ref}}^{\Gamma l+1,m+1,n+1} \right. \\
& \left. + \nabla p_{\text{cref}}^{\Gamma l,m+1,n+1} - \rho_{\text{ref}}^{\tilde{\Gamma} l,m+1,n+1} \mathbf{g} \right)
\end{aligned} \tag{5.32b}$$

$$\rho_{\text{ref}}^{\tilde{\Gamma} l,m+1,n+1} = \rho_{\text{ref}0} \left[1 + c_{\text{ref}} (p_{\text{ref}}^{\Gamma l+1,m+1,n+1} + p_{\text{cref}}^{\Gamma l,m+1,n+1} - p_0) \right] \tag{5.32c}$$

5.4.3 Flow and mechanics coupling

An iterative coupling between the fracture reservoir flow and geomechanics can be achieved similar to reservoir and geomechanics coupling, in the absence of fractures, in four ways: (1) Drained and (2) un-drained where the mechanics problem is solved first or (3) fixed strain and (4) fixed stress schemes where the flow precedes the mechanics problem. In this work, we rely on fixed stress scheme which has been shown to be stable and convergent (contraction mapping) for iterative coupling by Kim et al. (2011); Mikelic and Wheeler (2012)

$$-\nabla \cdot \boldsymbol{\sigma}^{\text{por}}(\mathbf{u}^{m+1,n+1}, p_{\text{ref}}^{m+1,n+1}) = f^{\tilde{m},n+1} \tag{5.33}$$

$$\mathbf{f}^{\tilde{m},n+1} = \left[\rho_s (1 - \phi^{*\tilde{m},n+1}) + \phi^{*\tilde{m},n+1} \sum_{\beta} \rho_{\beta}^{m+1,n+1} S_{\beta}^{m+1,n+1} \right] \mathbf{g} \tag{5.34}$$

$$\boldsymbol{\sigma}^{\text{por}}(\mathbf{u}^{m+1,n+1}, p_{\text{ref}}^{m+1,n+1}) = \boldsymbol{\sigma}(\mathbf{u}^{m+1,n+1}) - \alpha p_{\text{ref}}^{m+1,n+1} \mathbf{I} \quad (5.35)$$

$$\phi^{*\tilde{n},n+1} = \phi_o + \alpha \nabla \cdot \mathbf{u}^{m+1,n+1} + \frac{1}{M} p_{\text{ref}}^{m,n+1} \quad (5.36)$$

Interface conditions

$$(\boldsymbol{\sigma}^{\text{por},m+1}(\mathbf{u}^{m+1}, p_{\text{ref}}^{m+1})\mathbf{n})_{\Gamma^\pm} = -p_{\text{ref}}^{\Gamma m+1} \mathbf{n} \quad (5.37)$$

5.5 Fully Discrete Formulation

We utilize a multipoint flux mixed finite element method to construct a fully discrete form of the coupled fractured reservoir and mechanics problem described earlier. In this section, we only discuss the implicit scheme for the reservoir and fracture pressure equation coupling. The quantities in the discrete variational formulation are all in \mathbb{R}^3 along with ∇ and $\nabla \cdot$ operators, hence \mathcal{W} acts as a scaling factor. Also note that the stabilization term $(\gamma_{mr/f})$ for the contraction mapping of flow and mechanics coupling, as described in section 5.4, are omitted here for the sake of convenience of description. Further, the time index ‘n’ is dropped and invoked whenever necessary. The discrete variational formulation for the reservoir pressure reads: Given $p_{\text{ref},h}^{\Gamma k,l+1,m+1} \in W_h^\Gamma$, $S_{\text{ref},h}^{\Gamma l,m+1} \in W_h^\Gamma$ and $S_{\text{ref},h}^{l,m+1} \in W_h$, find $\mathbf{z}_{t,h}^{k+1,l+1,m+1} \in V_h$ and $p_{\text{ref},h}^{k+1,l+1,m+1} \in$

W_h , such that

$$\begin{aligned}
& \left\langle \frac{1}{\tilde{\lambda}_{t,h}^{k+1,\tilde{l},m+1}} \mathbf{K}^{-1} \mathbf{z}_{t,h}^{k+1,l+1,m+1}, \mathbf{v}_h \right\rangle_{Q,E} - \left(p_{\text{ref},h}^{k+1,l+1,m+1}, \nabla \cdot \mathbf{v}_h \right)_E \\
&= - \int_{\Theta} p_{\text{ref},h} \mathbf{v}_h \cdot \mathbf{n} - \sum_{\beta \neq \text{ref}} \int_{\Theta} \frac{\tilde{\lambda}_{\beta,h}}{\tilde{\lambda}_{t,h}} p_{c\beta,h} \mathbf{v}_h \cdot \mathbf{n} \\
&+ \left(\sum_{\beta \neq \text{ref}} \left[\frac{\tilde{\lambda}_{\beta,h}}{\tilde{\lambda}_{t,h}} \right]^{k+1,\tilde{l},m+1} p_{c\beta,h}^{n+1,k}, \nabla \cdot \mathbf{v}_h \right)_E \\
&- \left(\sum_{\beta} \left[\frac{\tilde{\lambda}_{\beta,h}}{\tilde{\lambda}_{t,h}} \right]^{k+1,\tilde{l},m+1} \rho_{\beta}^{n+1,k+1} g, \mathbf{v}_h \right)_E \quad \forall \mathbf{v}_h \in V_h,
\end{aligned} \tag{5.38}$$

where, $\Theta \in (\partial E \cap \Gamma) \cup (\partial E \cap \partial \Omega)$.

$$\begin{aligned}
& \left(\frac{1}{\Delta t} \sum_{\beta} \left(\phi^{*m} S_{\beta,h}^{l,m+1} \rho_{\beta,h}^{k+1,\tilde{l},m+1} \right), w_h \right)_E + \left(\nabla \cdot \mathbf{z}_{t,h}^{k+1,\tilde{l},m+1}, w_h \right)_E \\
&= \left(\frac{1}{\Delta t} \sum_{\beta} \left(\phi^* S_{\beta,h} \rho_{\beta,h} \right)^n, w_h \right)_E + \sum_{\beta} \left(q_{\beta,h}^{k+1,\tilde{l},m+1}, w_h \right)_E \quad \forall w_h \in W_h
\end{aligned} \tag{5.39}$$

The pressure continuity on $\partial E \cap \Gamma$ is given by,

$$p_{\text{ref},h}^{k+1,l+1,m+1} \mathbf{v}_h \cdot \mathbf{n} = p_{\text{ref},h}^{\Gamma k,l+1,m+1} \mathbf{v}_h^{\Gamma} \cdot \mathbf{n} \tag{5.40}$$

The jump in flux on $\partial E \cap \Gamma$ is given by,

$$\left(q_{l\beta,h}^{k+1,\tilde{l},m+1}, w_h^{\Gamma} \right) = [\mathbf{z}_{\beta,h} \mathbf{v}_h \cdot \mathbf{n}]^{k+1,\tilde{l},m+1} \tag{5.41}$$

$$q_{l\beta,h}^{k+1,\tilde{l},m+1} = \mathbf{z}_{\beta,h}^{k+1,\tilde{l},m+1} \cdot \mathbf{n} \Big|_{\Gamma^+} - \mathbf{z}_{\beta,h}^{k+1,\tilde{l},m+1} \cdot \mathbf{n} \Big|_{\Gamma^-} \tag{5.42a}$$

$$\begin{aligned}
q_{l\beta,h}^{k+1,\tilde{l},m+1} &= c_{1\beta}^{k+1,\tilde{l},m+1} p_{1h}^{k+1} + c_{2\beta}^{k+1,\tilde{l},m+1} p_{1h}^{\Gamma k+1} \\
&+ c_{3\beta}^{k+1,\tilde{l},m+1} p_{2h}^{k+1} + c_{4\beta}^{k+1,\tilde{l},m+1} p_{2h}^{\Gamma k+1}
\end{aligned} \tag{5.42b}$$

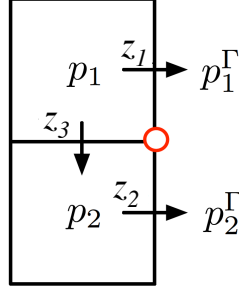


Figure 5.7: Coupling pressure and velocity degrees for a corner point

Here, $c_i = c_i(p_{\text{ref}}, S_{\text{ref}})$. The velocity and pressure degrees of freedom are coupled (Fig. 5.7) due to the multipoint flux scheme and are related as follows,

$$A \begin{pmatrix} z_1 \\ z_2 \\ z_3 \end{pmatrix} = \begin{pmatrix} p_1 - p_1^\Gamma \\ p_2 - p_2^\Gamma \\ p_1 - p_2 \end{pmatrix} \quad (5.43)$$

The jump in displacements on $\partial E \cap \Gamma$ gives the fracture width as,

$$\mathcal{W}_h^m = [\mathbf{u}_h^m \mathbf{r}_h \cdot \mathbf{n}] \quad (5.44)$$

Similarly, the discrete variational formulation for the fracture pressure equation reads: Given $\mathbf{u}_h^m \in R_h$, $\mathbf{z}_{\beta,h}^{k+1,l+1,m+1} \in V_h$ and $S_{\text{ref},h}^{l,m+1} \in W_h$, find $\mathbf{z}_h^{\Gamma k+1,l+1,m+1} \in V_h^\Gamma$ and $p_{\text{ref},h}^{\Gamma k+1,l+1,m+1} \in W_h^\Gamma$, such that

$$\begin{aligned} & \left\langle \frac{1}{\tilde{\lambda}_{t,h}^{\Gamma k+1,\tilde{l},m+1}} (\mathbf{K}^\Gamma)^{-1} \mathbf{z}_{t,h}^{\Gamma k+1,l+1,m+1}, \mathbf{v}_h^\Gamma \right\rangle_{Q,E^\Gamma} - \left(p_{\text{ref},h}^{\Gamma k+1,l+1,m+1}, \nabla \cdot \mathbf{v}_h^\Gamma \right)_{E^\Gamma} \\ &= \left(\sum_{\beta \neq \text{ref}} \left[\frac{\tilde{\lambda}_{\beta,h}}{\tilde{\lambda}_{t,h}} \right]^{\Gamma k+1,\tilde{l},m+1} p_{c\beta,h}^{\Gamma l,m+1}, \nabla \cdot \mathbf{v}_h^\Gamma \right)_{E^\Gamma} \\ & - \left(\sum_{\beta} \left[\frac{\tilde{\lambda}_{\beta,h}}{\tilde{\lambda}_{t,h}} \right]^{\Gamma k+1,\tilde{l},m+1} \rho_{\beta,h}^{\Gamma k+1,\tilde{l},m+1} g, \mathbf{v}_h^\Gamma \right)_{E^\Gamma} \quad \forall \mathbf{v}_h^\Gamma \in V_h^\Gamma \end{aligned} \quad (5.45)$$

$$\begin{aligned}
& \left(\frac{1}{\Delta t} \sum_{\beta} \left(\mathcal{W}_h^m S_{\beta,h}^{\Gamma l,m+1} \rho_{\beta,h}^{\Gamma k+1, \tilde{l}, m+1} \right), w_h^{\Gamma} \right)_E + \left(\mathcal{W}_h^m \nabla \cdot \mathbf{z}_{t,h}^{\Gamma k+1, \tilde{l}, m+1}, w_h^{\Gamma} \right)_E \\
&= \left(\frac{\mathcal{W}_h^m}{\Delta t} \sum_{\beta} \left(S_{\beta,h}^{\Gamma} \rho_{\beta,h}^{\Gamma} \right)^n, w_h^{\Gamma} \right)_E + \sum_{\beta} \left((q_{\beta,h}^{\Gamma} + q_{l\beta,h})^{k+1, \tilde{l}, m+1}, w_h^{\Gamma} \right)_E \quad \forall w_h^{\Gamma} \in W_h^{\Gamma}
\end{aligned} \tag{5.46}$$

The saturation equation is solved using lowest order DG once the water-phase fluxes are evaluated for a given pressure. The weak formulation for the reservoir saturation equation reads: Given $p_{\text{ref},h}^{l+1,m+1} \in W_h$, $\mathbf{z}_{\text{ref},h}^{l+1,m+1} \in V_h$, $S_{\text{ref},h}^{l,m+1} \in W_h$ and $\mathbf{u}_h^m \in R_h$ find $S_{\text{ref},h}^{l+1,m+1} \in W_h$, such that

$$\begin{aligned}
\left(S_{\text{ref},h}^{l+1,m+1}, w_h \right)_E &= \frac{\Delta t}{\phi^{*m} \rho_{\text{ref},h}^{\tilde{l}, m+1}} \left[\left(\frac{(\phi^* S_{\text{ref},h} \rho_{w,h})^n}{\Delta t}, w_h \right)_E \right. \\
&\quad \left. + \left((q_{\text{ref},h} + q_{l\text{ref},h})^{\tilde{l}, m+1}, w_h \right)_E - \left(\nabla \cdot \mathbf{z}_{\text{ref},h}^{l+1,m+1}, w_h \right)_E \right]
\end{aligned} \tag{5.47}$$

The weak formulation of the fracture saturation equation reads: Given $p_{\text{ref},h}^{\Gamma l+1,m+1} \in W_h^{\Gamma}$, $\mathbf{z}_{\text{ref},h}^{\Gamma l+1,m+1} \in V_h^{\Gamma}$ and $S_{\text{ref},h}^{\Gamma l,m+1} \in W_h^{\Gamma}$ find $S_{\text{ref},h}^{\Gamma l+1,m+1} \in W_h^{\Gamma}$, such that

$$\begin{aligned}
\left(S_{\text{ref},h}^{\Gamma l+1,m+1}, w_h^{\Gamma} \right)_{E^{\Gamma}} &= \frac{\Delta t}{\mathcal{W}_h^m \rho_{\text{ref},h}^{\Gamma \tilde{l}, m+1}} \left[\left(\frac{(\mathcal{W}_h S_{\text{ref},h}^{\Gamma} \rho_{w,h}^{\Gamma})^n}{\Delta t}, w_h^{\Gamma} \right)_{E^{\Gamma}} \right. \\
&\quad \left. + \left((q_{\text{ref},h}^{\Gamma} + q_{l\text{ref},h}^{\Gamma})^{\tilde{l}, m+1}, w_h^{\Gamma} \right)_{E^{\Gamma}} - \left(\mathcal{W}_h^m \nabla \cdot \mathbf{z}_{\text{ref},h}^{\Gamma l+1,m+1}, w_h^{\Gamma} \right)_{E^{\Gamma}} \right]
\end{aligned} \tag{5.48}$$

The discrete variational formulation for the reservoir geomechanics equations (5.3) reads: Given $p_{\text{ref},h}^{m+1} \in W_h$, $p_{\text{ref},h}^{\Gamma m+1} \in W_h^{\Gamma}$, $S_{\text{ref},h}^{m+1} \in W_h$ and, $S_{\text{ref},h}^{\Gamma m+1} \in W_h^{\Gamma}$ find $\mathbf{u}_h^{m+1} \in R_h$ such that,

$$\begin{aligned}
\int_E \boldsymbol{\sigma}(\mathbf{u}_h) : \boldsymbol{\varepsilon}(\mathbf{v}_h)_E - (\alpha p_{\text{ref},h}, \nabla \cdot \mathbf{v}_h) &= (\mathbf{f}_h, \mathbf{v}_h)_E + \int_{\partial E} \mathbf{g}_s^N \cdot \mathbf{v}_h \\
&\quad - \int_E \boldsymbol{\sigma}_{0,h} : \boldsymbol{\varepsilon}(\mathbf{u}_h) - (\alpha p_{0,h}, \nabla \cdot \mathbf{v}_h)
\end{aligned} \tag{5.49a}$$

$$\int_E \boldsymbol{\sigma}(\mathbf{u}_h) : \boldsymbol{\varepsilon}(\mathbf{v}_h)_E = (\lambda \nabla \cdot \mathbf{u}_h, \nabla \cdot \mathbf{v}_h) + (2\mu \boldsymbol{\varepsilon}(\mathbf{u}_h), \boldsymbol{\varepsilon}(\mathbf{v}_h)) \quad (5.49b)$$

The traction boundary condition for the fracture is then given by,

$$\mathbf{g}_s^N \cdot \mathbf{v}_h = -p_{\text{ref},h}^\Gamma \mathbf{n} \cdot \mathbf{v}_h \Big|_{\partial E \cap \partial E^\Gamma \neq \emptyset} \quad (5.50)$$

Note that the external boundary conditions are omitted in the weak formulation presented above to avoid a tedious description.

5.6 Linearization

In this section, we use an inexact Newton method to linearize pressure equations associated with reservoir and fracture domains. Since the poroelastic equations for reservoir geomechanics are linear we omit its discussion here. The computation of an exact Jacobian is tedious and computationally expensive. We therefore rely on an inexact Newton method, with density terms in the flux are Newton-iteration lagged, to form a linear system of equations in reservoir and fracture pressures and fluxes. The residuals are not altered and thus the final solution remains unchanged.

5.6.1 Explicit Coupling

The linearized reservoir flow system can be written as,

$$\begin{pmatrix} A_r & B \\ B^T & C_r \end{pmatrix} \begin{pmatrix} \delta z_{tr} \\ \delta p_{\text{ref}} \end{pmatrix} = - \begin{pmatrix} R_{1r} \\ R_{2r} \end{pmatrix} \quad (5.51)$$

Eliminating δz_t in favor of δp_{ref} in Eqn.(5.51),

$$(B_r^T A_r^{-1} B_r + C_r) \delta p_{\text{ref}} = -R_{2r} + B_r^T A_r^{-1} R_{1r}. \quad (5.52)$$

Similarly, the linearized fracture flow system is,

$$\begin{pmatrix} A_f & B_f \\ B_f^T & (C_f + \tilde{C}_f) \end{pmatrix} \begin{pmatrix} \partial z_{tf}^\Gamma \\ \delta p_{ref}^\Gamma \end{pmatrix} = - \begin{pmatrix} R_{1f} \\ R_{2f} + \tilde{C}_f (p_{ref}^\Gamma)^k \end{pmatrix} \quad (5.53)$$

Here, $\tilde{C}_f = \text{Diag}(\gamma_f)$ and $(p_{ref}^\Gamma)^k$ reservoir fracture coupling iteration lagged, fracture pressure vector of size R_{2f} . Further, eliminating z_t^Γ in favor of p_{ref}^Γ in Eqn.(5.53),

$$(B_f^T A_f^{-1} B_f + C_f) \delta p_{ref}^\Gamma = -R_{2f} + B_f^T A_f^{-1} R_{1f} \quad (5.54)$$

Iterations between the reservoir and fracture Newton systems are performed conducted until a desired tolerance is achieved.

5.6.2 Implicit coupling

The linearized system of equations for the implicitly coupled reservoir-fracture flow can be written as,

$$\begin{pmatrix} A_r & B_r & 0 & L \\ B_r^T & C_r & 0 & 0 \\ 0 & 0 & A_f & B_f \\ L^T & 0 & B_f^T & C_f \end{pmatrix} \begin{pmatrix} \delta z_{tr} \\ \delta p_{ref} \\ \delta z_{tf} \\ \delta p_{ref}^\Gamma \end{pmatrix} = - \begin{pmatrix} R_{1r} \\ R_{2r} \\ R_{1f} \\ R_{2f} \end{pmatrix}. \quad (5.55)$$

The right hand side terms $R_{ir/fs}$ can be evaluated similar to those presented in the previous chapters. Eliminating δz_{tr} and δz_{tf} results in a linear system of equation in δp_{ref} and δp_{ref}^Γ .

$$(C_r - B_r^T A_r^{-1} B_r) \delta p_{ref} - B_r^T A_r^{-1} L \delta p_{ref}^\Gamma = B_r^T A_r^{-1} R_{1r} - R_{2r} \quad (5.56)$$

$$\begin{aligned} (C_f - B_f^T A_f^{-1} B_f - L^T A_r^{-1} L) \delta p_{ref}^\Gamma - L^T A_r^{-1} B_r \delta p_{ref} \\ = B_f^T A_f^{-1} R_{1f} + L^T A_r^{-1} R_{1r} - R_{2f} \end{aligned} \quad (5.57)$$

An important point to note here is that the third term in the coefficient of δp_{ref}^Γ in Eqn. (5.57) appears only for an implicitly coupled reservoir fracture flow system. The presence of this term makes the linear system in δp_{ref} and δp_{ref}^Γ strictly diagonally dominant.

$$\begin{pmatrix} D_{rr} & D_{rf} \\ D_{fr} & D_{ff} \end{pmatrix} \begin{pmatrix} \delta p_{ref} \\ \delta p_{ref}^\Gamma \end{pmatrix} = - \begin{pmatrix} R_3 \\ R_4 \end{pmatrix}. \quad (5.58)$$

A block Gauss-Siedel method is used to solve this resulting linear system of equations which is known to be convergent for strictly diagonally dominant matrices. The rate of convergence is dependent on the strength of the diagonal terms. It can be easily seen from Eqn. (5.55) this is in turn in dependent on two ratios:(1) saturation weighted fluid compressibilities to time step and (2) fracture to reservoir absolute permeabilities. The block Gauss-Siedel method, with j as the linear iterate, can be written as,

$$D_{rr} (\delta p_{ref})^{j+1} = -R_3 - D_{rf} (\delta p_{ref}^\Gamma)^j \quad (5.59a)$$

$$D_{ff} (\delta p_{ref}^\Gamma)^{j+1} = -R_4 - D_{fr} (\delta p_{ref})^{j+1} \quad (5.59b)$$

5.7 Results

In this section, we consider a number of numerical experiments to demonstrate our modeling and computational approaches. We begin with validation of the coupled reservoir-fracture flow model by comparing with physical experimental results for spontaneous imbibition of the wetting phase. The second numerical experiment studies the significance of fracture orientations

for recovery processes in a reservoir. An injection scenario for a multi-stage hydraulic fracture is shown in the third example. The fourth example demonstrates stress field reorientations for injection and production from a hydraulic fracture. Finally, a field case for Frio (Juntunen and Wheeler (2012)) is presented showing long term production from a fractured reservoir with multiple injection and production wells. The numerical experiments have been conducted for both lab scale as well as field scale. Please note that the fracture aperture (or width) is time invariant and varies spatially from 1 mm - 3 mm along the fracture length in all numerical experiments except example 4. For the couple flow and mechanics the above is used as an initial guess since fracture widths vary spatially and temporally and are solved as a part of the system of equations.

5.7.1 Capillary imbibition in a fractured core

We compare the results of our numerical model to experimental data, given by Karpyn (2005), for a fractured Berea sandstone core. The core is initially saturated only with water ($S_w = 1.0$) followed by a primary drainage until an irreducible water saturation of ($S_{w_{irr}} = 0.25$) is achieved. This is followed by a secondary spontaneous capillary imbibition of water, without imposing a pressure gradient across the core until an equilibrium saturation is achieved.

The numerical experiment aims to simulate the secondary imbibition process which is then compared with experimental values of average satura-

| | | | |
|------------|--------------------------|-------------------|-------------------------|
| ϕ | 0.178 | $K_x = K_y = K_z$ | 68 mD |
| c_w | 1.E-7 psi ⁻¹ | c_o | 1.E-4 psi ⁻¹ |
| ρ_w | 62.4 lbm/ft ³ | ρ_o | 56 lbm/ft ³ |
| ν_w | 1 cP | ν_o | 2 cP |
| S_w^0 | 0.2 | P_w^0 | 1000 psi |
| S_{wirr} | 0.1 | S_{or} | 0.2 |

Table 5.1: Capillary imbibition: rock and fluid property information

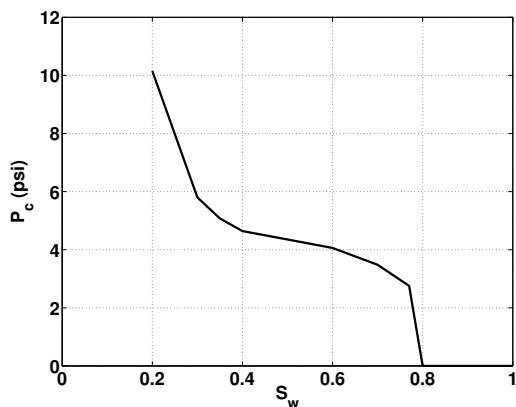


Figure 5.8: Rock matrix capillary pressure curve

tion and saturation profiles for validation purposes. The relative permeability curves for the fracture are chosen to be linear functions of water saturation. This is in agreement with a zero capillary pressure assumption in the fracture implying no preference of the fracture domain towards a specific fluid phase. The capillary pressure and relative permeability curves for the matrix and fracture are shown in Figs. 5.8 thru 5.10. Further a no-flow boundary condition is assumed everywhere except the bottom surface which is open to flow in accord with the experiments.

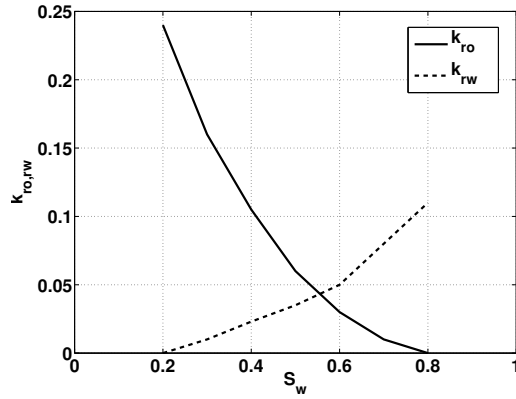


Figure 5.9: Rock matrix relative permeability curve

Table 5.1 provides fluid and rock property information for the core. This example demonstrates that the model can be used to simulate both core-scale and later field-scale scenarios while accurately capturing the physics. The cleaned Berea core is conventionally water wet as can be seen in the matrix relative permeability and capillary pressure curves. Figs. 5.11 and 5.12 show experimental saturation profiles obtained using digital radiography and numerical results at different time instances, respectively. Furthermore, the fracture width varies spatially for an accurate depiction of fracture flow. The saturation profiles and average saturations are in good agreement with experimental values. The differences in curvatures between experimental and numerical saturation profiles is attributed to the core holder properties. The numerical simulation does not take into account the wetting characteristics of the core holder.

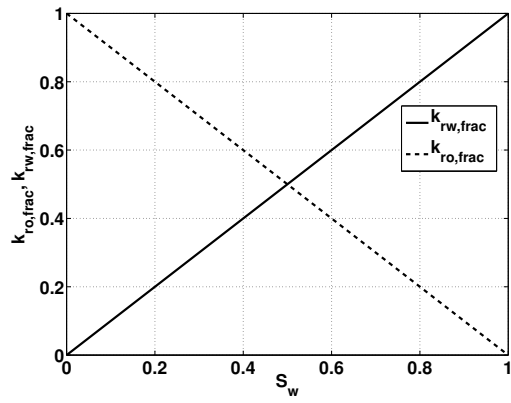


Figure 5.10: Fracture relative permeability curve

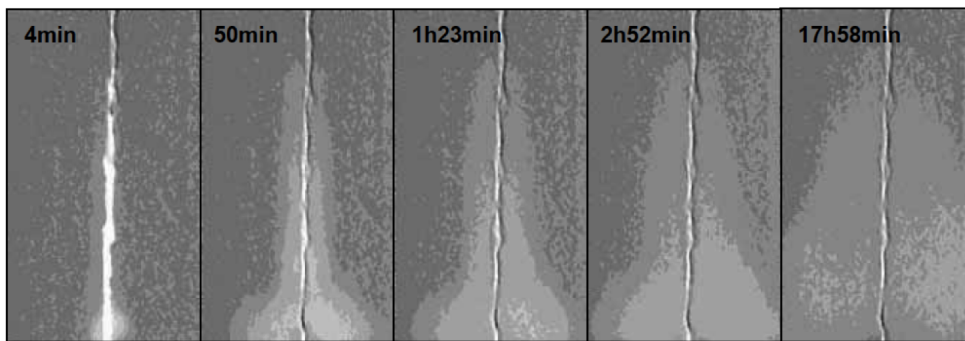


Figure 5.11: Experimental saturation profiles from Karpyn (2005) using digital radiography at different times

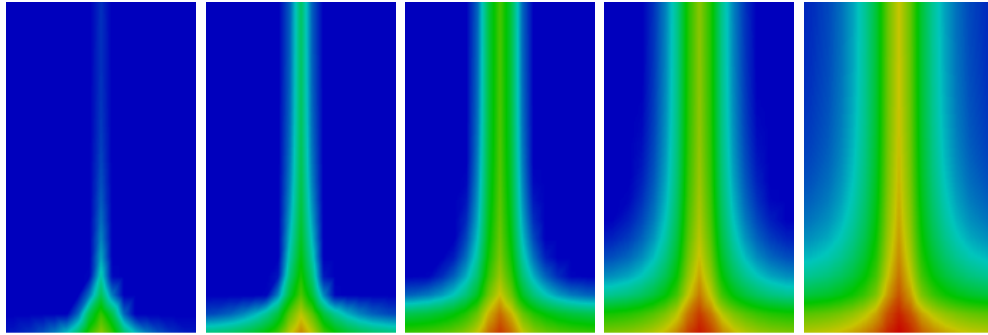


Figure 5.12: Numerical saturation profiles (left to right)

5.7.2 Discrete natural fractures

In the introduction section, we presented a single fracture example to motivate a detailed interface based modeling approach. In the introduction, we presented an example (Fig. 5.2) where the saturation front channeled through the fracture thereby reducing sweep area. Here, we present a similar case with two discrete fractures in a reservoir domain of size $10 \text{ ft} \times 10 \text{ ft}$ (approximately) with bottom-hole pressure specified injection (520 psi) and production (500 psi) wells located at diagonally opposite ends. The reservoir and fluid property data along with initial and boundary conditions remain unchanged.

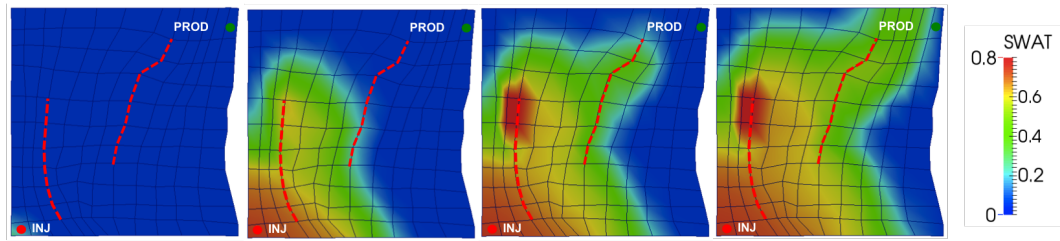


Figure 5.13: Saturation profiles at $t = 1, 100, 150$ and 200 days (left to right).

The fracture closer to the injector (Fig. 5.13) acts as a shield against the fluid front preventing it from channeling through the other fracture thereby improving sweep area. Thus a fracture can enhance or deteriorate sweep based upon its orientation to the fluid front. This example shows the impact of accurately capturing non-planar fracture geometries and their orientation with respect to the reservoir as well as each other. We also infer that fractures orthogonal to the line joining injector and producer will increase recovery efficiency. On the other hand, a fracture parallel to this line will be detrimental to the recovery of hydrocarbons due to poor sweep efficiency and therefore early breakthrough. It is interesting to note that the former type can be represented using a permeability averaging based approach without significant loss of accuracy. However, the latter still requires a high resolution modeling approach to maintain accuracy. Exploiting the cheaper computational cost of averaging and incorporating this in our detailed modeling will be addressed elsewhere. The insights from this example can be used for studying field scale fractured-reservoirs and as an assistive tool during various planning and developmental stages.

5.7.3 Multi-stage hydraulic fracture

A three-stage hydraulic fracture with fracture aperture varying along the length is considered. In this example, we stress on the interaction between hydraulic fractures and their consequent impact on injectivity enhancement. Fig. 5.14 gives a schematic of the problem description. We consider a reservoir domain of size $200 \text{ ft} \times 600 \text{ ft} \times 300 \text{ ft}$ with three hydraulic fractures (shaded green) connected to a bottom-hole pressure specified (1000 psi) injection well (shaded blue). A no-flow boundary condition is assumed everywhere except for a part of external boundary (shaded red) where pressure has been specified (400 psi) to show the effect of boundary conditions on injectivity.

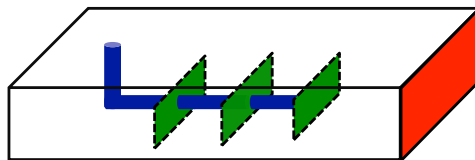


Figure 5.14: Schematic of a three-stage hydraulic fracture connected to a wellbore.

Note that the fracture geometry is non-planar and the depiction in Fig. 5.14 is a simple representation. The fracture half-lengths are approximately 50 ft with apertures varying from 3mm at the center to 1 mm towards the edges. Table 6.1 provides the reservoir and fluid property data along with the initial conditions. Fig. 5.15 shows the pressure (top) and saturation (bottom) at three time instances. The pressure profile remains almost invariant with time, however saturation profile indicates differences in injectivities from the three

| | | | |
|----------|--------------------------|-------------------|-------------------------|
| ϕ | 0.2 | $K_x = K_y = K_z$ | 50 mD |
| c_w | 1.E-6 psi ⁻¹ | c_o | 1.E-4 psi ⁻¹ |
| ρ_w | 62.4 lbm/ft ³ | ρ_o | 56 lbm/ft ³ |
| ν_w | 1 cP | ν_o | 2 cP |
| S_w^0 | 0.2 | P_w^0 | 800 psi |

Table 5.2: Multi-stage hydraulic fractures: reservoir and fluid properties

fractures. These differences arise due to a combined effect of proximity to other hydraulic fractures and the external boundary conditions. The fracture closest to the pressure specified boundary (least shielded) exhibits maximum injectivity whereas the one farthest (most shielded) contributes the least.

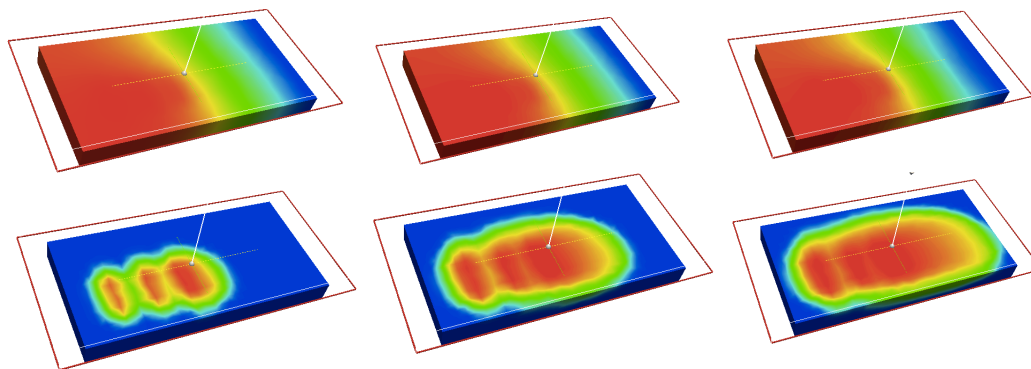


Figure 5.15: Pressure (top) and saturation (bottom) profiles at $t = 1, 2$ and 6 days (from left to right).

A detailed analysis indicates that an optimal fracture spacing which maximizes injectivity can be achieved while minimizing screening effects for the current setting. It is also seen that decreasing fracture half-lengths as the proximity to pressure boundary increases leads to similar results.

5.7.4 Coupled flow and mechanics

In this example, we demonstrate the effect of fracture on the stress field similar to stress field reorientation studies presented by Roussel and Sharma (2009). A reservoir domain of size 250 ft \times 250 ft with a single fracture of half-length 25 ft is assumed with fracture apertures varying during injection and production stages from 0.01 ft to 0.05 ft. The Youngs modulus, Poissons ratio and max and minimum stress values are taken to be 7.3×10^6 psi, 0.2, 6400 and 6300 psi respectively. The initial pressure for the injection and production cases is 500 psi and 5000 psi, respectively. A fracture pressure specification of 5000 psi and 2000 psi was assumed for injection and production cases, respectively with no flow external boundary conditions. We enforce a zero tangential displacement condition at the midpoints of the domain edges to avoid rigid body motion. The reservoir property data is given in Table 2 and is same as in the previous example. Fig. 5.16 shows a schematic of the problem description.

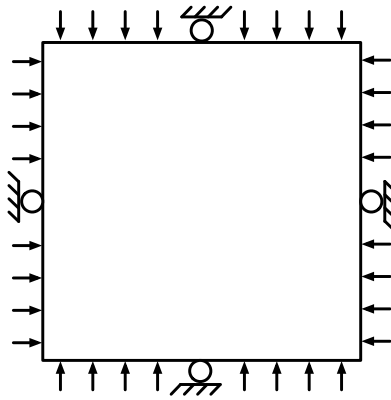


Figure 5.16: Problem description.

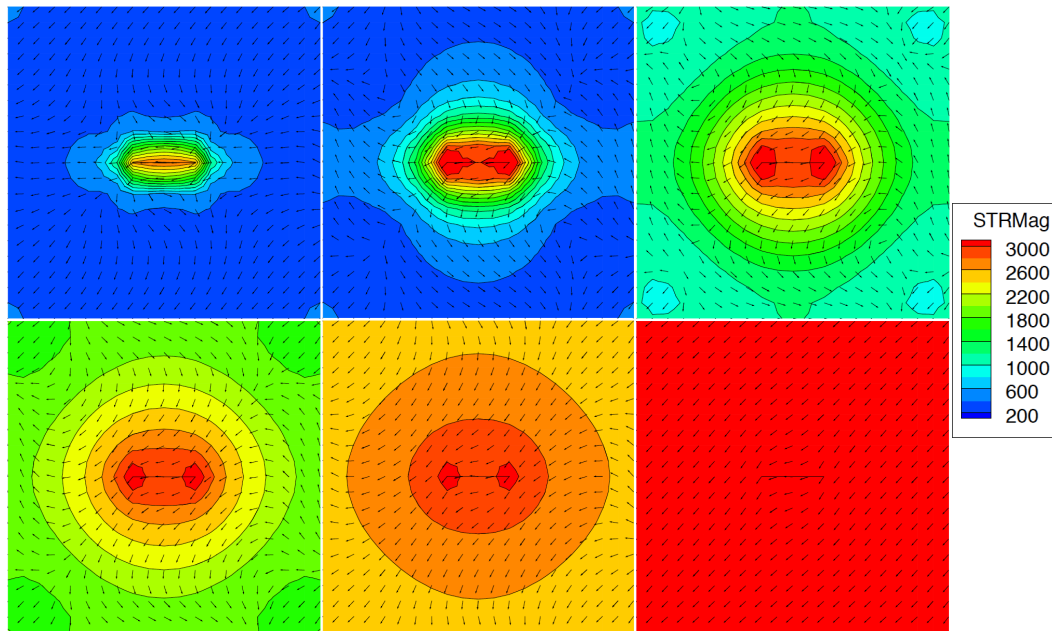


Figure 5.17: Stress magnitude (contour, psi) and principal stress direction (vector) for a single fracture injection case for $t = 0.02, 0.2, 2.0$ days(top row, from left to right) and $t = 3.7, 6.4$ and 20 days (bottom row, from left to right).

Figs. 5.17 and 5.18 show variations of principal stress directions and magnitude contours for a single fracture injection and production cases, respectively. It is observed that the principal stress directions around the fracture do not vary significantly for the injection case. However, the changes away from the fracture are primarily due to boundary conditions. Note that we solve on a full domain compared to the quarter domain problem presented by Roussel and Sharma (2009) owing to symmetry arguments. On the other hand, a stress field re-orientation occurs around the fracture very early for the production case. This is strongly influenced by the difference between initial pressure and

bottom-hole pressure.

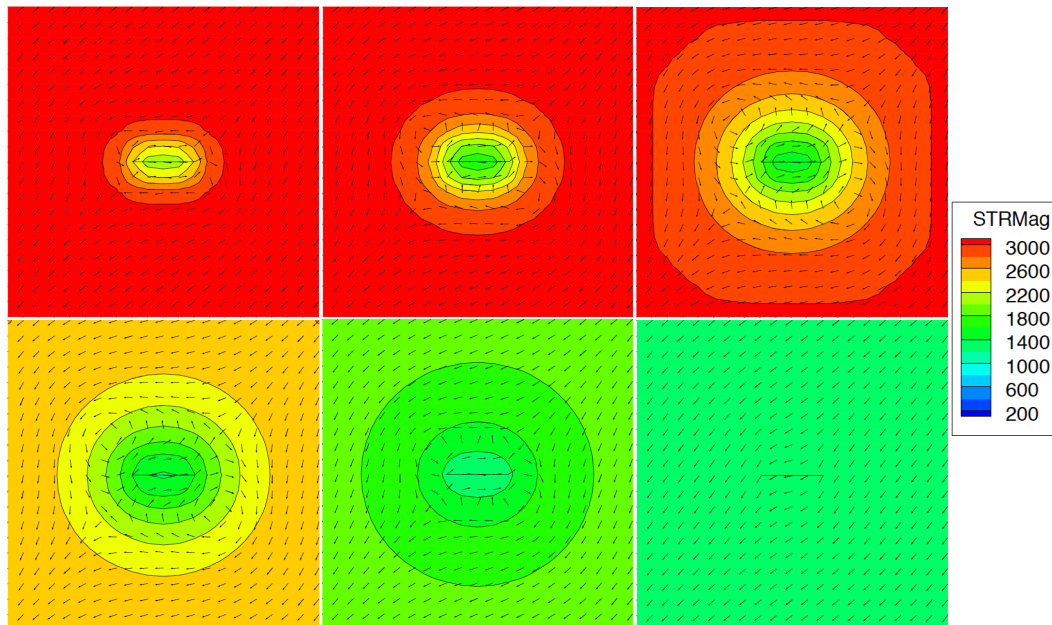


Figure 5.18: Stress magnitude (contour, psi) and principal stress direction (vector) for a single fracture production case for $t = 0.02, 0.1, 6.0$ days (top row, left to right) and $t = 2.5, 7.5$ and 20 days (bottom row, left to right).

5.7.5 Frio field case with natural fractures

In this example, we show an extension to field scale fractured reservoirs. Fig. 5.19 shows a section of Frio field (Juntunen and Wheeler (2012)) with discrete natural fractures (shaded orange) with 9 pressure-specified wells: 6 injectors (4000 psi) and 3 producers (2000 psi). The MFMFE discretization allows for accurate representation of reservoir as well as fracture geometries. The reservoir dimensions are approximately $8000 \text{ ft} \times 7000 \text{ ft} \times 2000 \text{ ft}$ owing to the complex geometry. A uniform fracture aperture of 0.003 ft is assumed for

the three fractures. Table 5.3 lists the reservoir and fluid property information.

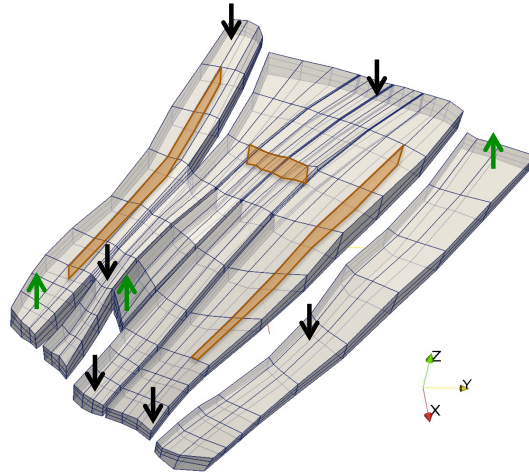


Figure 5.19: Frio field case with discrete fractures (shaded orange).

A deliberate choice of isotropic and homogeneous permeability field is made in order to accentuate the presence of fractures. Fig. 5.20 shows the pressure and saturation profiles after 800 days. We make two important observations: (1) the two longer fractures (along the reservoir length) are detrimental to recovery since the injected fluid shoots through and reduces sweep area, and (2) the shorter fracture (along the reservoir breadth) acts as a screen or shield to the fluid front and increases sweep area. Thus, well placement in a fractured reservoir requires additional considerations as opposed to reservoirs with no fractures.

The use of explicit flow models for fractures (hydraulic and natural) provide us with an accurate depiction of flow fields. The coupled flow model, presented here, captures pressure contrast between the reservoir and fracture

| | | | |
|--------------|--------------------------|-------------------|-------------------------|
| ϕ | 0.2 | $K_x = K_y = K_z$ | 50 mD |
| c_w | 1.E-7 psi ⁻¹ | c_o | 1.E-4 psi ⁻¹ |
| ρ_w | 62.4 lbm/ft ³ | ρ_o | 56 lbm/ft ³ |
| ν_w | 1 cP | ν_o | 2 cP |
| $S_{w,init}$ | 0.2 | $P_{w,init}$ | 3000 psi |

Table 5.3: Frio with fractures: reservoir and fluid properties

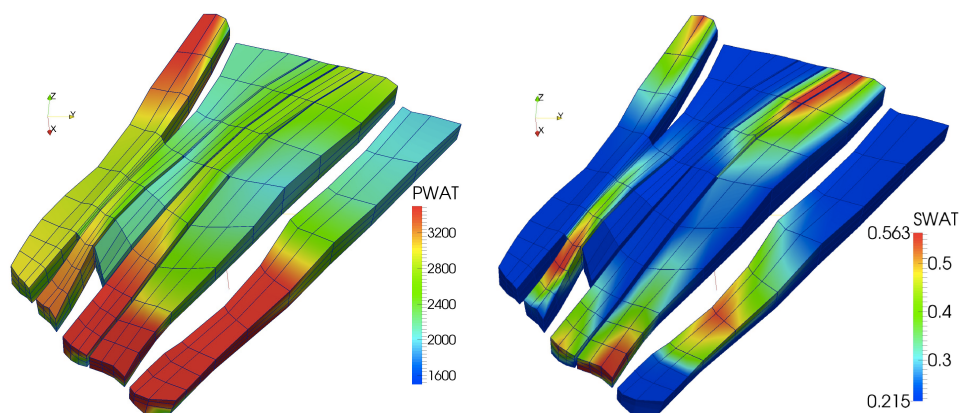


Figure 5.20: Pressure (left) and saturation (right) profiles after 2.2 years.

owing to the order of magnitude differences in permeability (or conductivity) values. The model also utilizes different capillary pressure curves for reservoir and fracture domains. Thus spontaneous capillary imbibition mechanism can be studied as an alternative mechanism of recovery in water wet, oil shales and tight formations. Furthermore, general hexahedral grids allows representation of non-planar fractures without requiring substantial changes in the petrophysical properties of the adjacent reservoir. Finally, the model captures sharp changes in pressure across the fracture which provides a better trac-

tion boundary condition for the coupled geomechanics model. The stress and displacement fields in a poroelastic reservoir due fluid pressure changes are therefore accurately represented.

5.8 Nomenclature

| | | |
|--------------------------|---|--|
| Γ | = | fracture domain |
| Ω | = | reservoir domain |
| $\partial\Omega^{N,D}$ | = | reservoir flow boundary |
| $\partial\Omega_s^{N,D}$ | = | reservoir mechanics boundary |
| ϕ^* | = | porosity |
| ϕ_o | = | reference porosity |
| ref | = | reference phase |
| β | = | oil (o) or water (w) phase |
| S_β | = | saturation of phase ' β ' |
| p_β | = | pressure of phase ' β ' |
| $p_{c\beta}$ | = | capillary pressure of phase ' β ' |
| ρ_β | = | density of phase ' β ' |
| $\rho_{\beta o}$ | = | reference density of phase ' β ' |
| \mathbf{z}_β | = | Darcy flux of phase ' β ' |
| \mathbf{z}_t | = | total flux |
| ν_β | = | viscosity of phase ' β ' |
| c_β | = | compressibility of phase ' β ' |
| k_β | = | relative permeability of phase ' β ' |
| q_β | = | source or sink term for phase ' β ' |

| | | |
|-----------------------------|---|---|
| $q_{l\beta}$ | = | fracture leakage term for phase ' β ' |
| \mathbf{K} | = | absolute permeability |
| \mathbf{g} | = | acceleration due to gravity |
| \mathcal{W} | = | fracture aperture or width |
| \mathbf{u} | = | displacement |
| $\boldsymbol{\sigma}^{por}$ | = | Cauchy stress tensor |
| $\boldsymbol{\varepsilon}$ | = | strain tensor |
| λ, μ | = | Lame parameters |
| α | = | dimensionless Biot coefficient |
| M | = | Biot constant |
| \mathbf{f} | = | body force |
| S_{wirr} | = | Irreducible water saturation |
| S_{or} | = | Residual oil saturation |

Chapter 6

Coupled Fracture Propagation and Reservoir Flow Model

6.1 Introduction

Hydraulic fracturing is a well known method for recovering oil and gas from tight gas and shale plays. It is pivotal for meeting a continually growing energy demand. Concerns are also being raised regarding its impact on long and short term environmental implications. Thus, there is an imminent need for physically and mathematically consistent, accurate and robust computational models for representing fluid filled fractures in a poroelastic medium. The simplest model description involves coupling of (1) mechanical deformation, (2) reservoir-fracture fluid flow, (3) and fracture propagation. The rock deformation is usually modeled using the linear elasticity theory (Biot (1941b,c, 1955b)). For fluid flow modeling, lubrication theory and Darcy flow are assumed in the fracture and reservoir respectively, which are coupled

This work has been partly presented at the SPE Hydraulic Fracturing Technology conference (Wick et al. (2014a)) and published as an ICES report (Wick et al. (2014b)). Phase field fracture propagation models for poroelastic media are primarily developed by Drs. Andro Mikelić, Thomas Wick and Mary F. Wheeler. The coupling of phase field fracture propagation and reservoir flow models is done by Gurpreet Singh under the supervision of Prof. Mary F. Wheeler with assistance from Dr. Thomas Wick. The phase field models were also used here to study applications of interest to the oil and gas industry.

through a leakage term. Finally, for fracture propagation the conventional energy-release rate approach of linear elastic fracture mechanics (LEFM) theory is used. We also note some of the concurring modeling and numerical approaches for fracture propagation currently used such as cohesive zone models (Xu and Needleman (1994)), displacement discontinuity methods (Crouch (1976)), partition-of-unity (Babuska and Belenk (1997)) based XFEM/GFEM methods (Moes et al. (1999); de Borst et al. (2006); Secchi and Schrefler (2012); Babuska and Banerjee (2012)), boundary element formulations (BEM) (Castonguay et al. (2013)) and peridynamics (Silling (2000)).

Variational approaches (Francfort and Marigo (1998); Bourdin et al. (2008)) and a thermodynamically consistent phase field formulation (C. Miehe (2010)) have been employed in solid mechanics. An application to hydraulic fracturing is given in (Bourdin et al. (2012)). C. Miehe (2010) extended the variational approach (Francfort and Marigo (1998); Bourdin et al. (2008)) by modeling crack irreversibility through an entropy condition satisfying the second law of thermodynamics and decomposing the strain tensor to account for tension and compression. Our approach (Mikelić et al. (2013a,b)) is based upon C. Miehe (2010) with an extension to porous media applications where solids (geomechanics) interact with fluids. To develop a phase-field formulation for such applications, geomechanics and porous media flows are decoupled using fixed-stress splitting (Settari and Walters (2001); Mikelić and Wheeler (2012)). With this methodology, modeling and simulations of hydraulic fractures in poroelasticity have been considered (Mikelić et al. (2014a,b); Wheeler

et al. (2014a); Wick et al. (2014a)).

We provide a brief recapitulation describing Griffith's model for fracture growth in brittle media. The classical theorem of minimum energy suggests that an equilibrium state achieved by an elastic body deformed by surface forces is such that the potential energy of the system is minimal. This was later augmented by Griffith (1921), in his seminal work, assuming a different equilibrium state is possible which accounts for formation of fractures as a mechanism for lowering potential energy. This criterion of rupture assumes that the cohesive forces, due to molecular attraction, act close to the fracture tip. Thus, the contribution of cohesive forces (surface potential energy) to the total potential energy can be assumed to be negligible. Based upon these assumptions, a decrease in potential energy is proportional to the generated surface area with the critical energy release rate (G_c) as the constant of proportionality. In this work, we rely upon this classical work along with its assumptions on the fracture growth criteria. As noted by Barenblatt (1962), we do not underestimate the significance of cohesive forces at the fracture tip. However, the contribution of these forces to the total potential energy is assumed to be significant only during fracture nucleation which diminishes as the fracture grows. Based upon these arguments we assume that LEFM is applicable.

Using a phase-field approach, a lower-dimensional crack surface is approximated as a diffusive transition zone by a phase-field function φ . Fig. 6.1 shows this diffusive transition zone (also brittle or mushy-zone) between the

broken (white zone) and the unbroken (brown zone) states of the material. A fixed-topology finite element phase-field approach is shown where a (lower-dimensional) crack is approximated with the help of a phase-field function. The phase-field function is an indicator function with values 0 and 1 inside and outside the crack, respectively. The mushy-zone also provides a smooth interpolation for the interface between a fracture and reservoir. A coupling of reservoir fluids and geomechanics allows a comprehensive study of this multiscale problem where only few results have been published to date (see for instance Dean and Schmidt (2008) and Lujun and Settari (2007)). Further, we also describe an algorithm to integrate fracture growth patterns with our reservoir simulator IPARS (Implicit Parallel Accurate Reservoir Simulator). This allows for both short term transient pressure analysis and long term recovery predictions. We note that crack or fracture propagation, which will be used interchangeably, implies both variation of fracture width (or aperture) and its length.

The major advantages of using phase-field modeling for crack propagation are four-fold: First, and most important, the model is easy to implement and uses a fixed-grid topology in which remeshing for resolving the exact fracture location is avoided. Second, fracture nucleation, propagation, kinking, and curvilinear path are intrinsically determined. This avoids computational overheads associated with post-processing of quantities such as stress intensity factors. Third, we can easily handle large fracture networks since complex phenomena of joining and branching does not require keeping track of fracture

interfaces. Fourth, modeling crack growth in heterogeneous media does not require special treatment. Here however, the length-scale parameter ε should be chosen accordingly. Additionally, the crack opening displacement (fracture aperture) can be calculated using the phase-field function. We use the pressurized crack propagation model in a poroelastic medium using a phase-field approach proposed by Mikelić et al. (2013a,b).

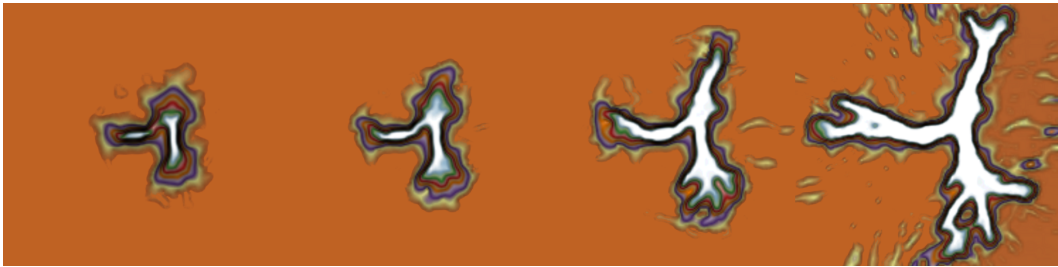


Figure 6.1: Evolution of two pressurized fractures: first joining, then nonplanar growth and finally branching in heterogeneous porous media.

We investigate the phase-field approach for different crack propagation scenarios including heterogeneous porous media including permeability and geomechanical parameters. We perform numerical studies for multi-stage and sequential hydraulic fracturing scenarios while discussing the effect of stress shadowing, rock heterogeneities and fracture spacing. Third, we consider the phase-field model as a fractured-well approach in a reservoir and we consequently couple this approach to a reservoir simulator. This paper concentrates primarily on the approach for fracture growth using slick-water injection. We account for varying reservoir complexities such as natural fractures, faults and barriers using a comprehensive fractured poroelastic reservoir flow model. This

allows for a two-stage production optimization owing to (1) a well-engineered hydraulic fracturing scheme followed by (2) an optimal fractured well placement considering far from well-bore reservoir complexities. This chapter is organized as follows: we first provide our motivation for the work and the reason for our choice of using a phase-field model for hydraulic fracturing. In the next section, we provide the governing equations for the fracture phase-field approach as well as the reservoir flow equations. In the section after, we provide details on the coupling algorithm between the fracture phase-field model and the reservoir simulator. In the final section, numerical tests are discussed to demonstrate our method.

6.2 Pressurized and Fluid-filled Crack Propagation Models using Phase-field

In this section, we describe the proposed model development starting by defining a two-field problem in two unknowns: (1) a vector displacement field and (2) a scalar phase-field variable (φ), assuming a known pressure field (the so-called pressurized fracture propagation). This is later extended to a three-field problem, adding scalar pressure (p) as an unknown, accounting for flow inside the porous rock matrix and the fracture (the so-called fluid-filled fracture propagation). Therein, a single pressure diffusion equation (see Mikelić et al. (2014a)), derived from the mass conservation equation and Darcy’s law, is used for local flow field calculations. The elasticity and phase-field equations are formulated as an energy minimization problem. We obtain a weak form of

the differential equations by differentiating this energy minimization function with respect to the solution variables. This serves as a natural setting for using a Galerkin finite element method for spatial discretization. Before we begin, it is important to discuss the key features of the classical brittle fracture theory (Griffith (1921)) used in this work. The theory postulates two physical phenomena: (1) linear elasticity and (2) fracture propagation, as energy dissipation mechanisms, strictly separated by a threshold (critical energy release rate) assuming a sharp transition between the fractured and non-fractured media. The Griffith's criterion for brittle fracture propagation assumes:

1. The crack growth is irreversible.
2. The energy release rate is bounded above by a critical energy release rate.
3. The crack grows if and only if the energy release rate is critical.

Let Ω be the reservoir domain, as shown in Fig. 6.2, with the fracture $\mathcal{C} \subset \Omega$.

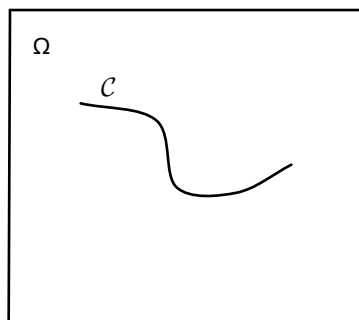


Figure 6.2: Problem description.

6.2.1 Pressurized fracture propagation model (two-field problem)

We begin by describing the pressurized fracture approach where a known pressure field is assumed on the domain Ω . The pressure remains invariant along the fracture length varying only temporally based upon a simple correlation. The pressure variation along the fracture length is assumed to be negligible. Later we show that this assumption is valid if the fracture conductivity is substantially larger than the reservoir conductivity, which is usually the case. The energy functional for a poroelastic material (Ω) with a crack (\mathcal{C}) reads:

$$E(u, \mathcal{C}) = \underbrace{\frac{1}{2} \int_{\Omega} \sigma_E : e(u)}_{\text{Elastic energy}} - \underbrace{\int_{\Omega} \alpha_B (p - p_0) \nabla \cdot u}_{\text{Pore pressure contribution}} + \underbrace{G_c \mathcal{H}^{d-1}(\mathcal{C})}_{\text{Fracture energy}}, \quad (6.1)$$

with the following constitutive stress-strain equation and definition of strain $e(u)$:

$$\sigma_E = 2\mu e(u) + \lambda \text{tr}(e(u))I, \quad (6.2)$$

$$e(u) = \frac{1}{2}(\nabla u + \nabla u^T). \quad (6.3)$$

where μ and λ denote the Lamé parameters, σ_E the Cauchy stress tensor, $e(u)$ the strain tensor, α_B the Biot coefficient, p the pore pressure, p_0 the reference pressure, u the displacements. G_c is the critical elastic energy release rate depending on the material and is determined experimentally and \mathcal{H}^{d-1} is the length (or surface area) in a 2D (or 3D) domain. Please note that G_c

is related to stress intensity factor under certain assumptions on the material such as an isotropic, linear elastic solid (Irwin (1958)). Further, we follow the approach presented by Ambrosio and Tortorelli (1990) for approximating the fracture length (\mathcal{H}^{d-1}) using an elliptic functional

$$\mathcal{H}^{d-1} = \frac{1}{2\varepsilon} \|1 - \varphi\|^2 + \frac{\varepsilon}{2} \|\nabla\varphi\|^2, \quad (6.4)$$

thereby introducing an additional variable φ , referred to as the phase-field variable hereafter. This variable is a quantity defined on the entire domain Ω for a time span varying from 0 to T. A careful examination of **Eqn. 6.4** shows, for a given value of $\varepsilon > 0$, this functional assumes lowest values when φ is a constant assuming values of either 0 representing a fracture or 1 representing the porous rock matrix. Please note that these values are strictly 0 or 1 for a continuum (strong form) description of a pressurized fracture model. We notice that the phase-field approach is related to gradient-type material modeling with a characteristic length-scale. Here, the above regularization parameter ε can be considered as such a length-scale parameter that has a physical meaning (Pham et al. (2011); C. Miehe (2010) and references cited therein). The second term ensures that φ changes smoothly between 0 and 1 allowing the representation of the fracture as a diffuse interface. **Eqn. 6.4** represents a mathematically-consistent approximation of the *true* crack \mathcal{H}^{d-1} . In order to satisfy assumptions 2 and 3 the energy functional (**Eqn. 6.1**) is

regularized with φ as follows:

$$\begin{aligned}
E_\varepsilon(u, \varphi) = & \frac{1}{2} \int_{\Omega} ((1 - \kappa)\varphi_+^2 + \kappa)\sigma_E : e(u) - \int_{\Omega} \alpha_B(p - p_0)\varphi_+^2 \nabla \cdot u \\
& + G_c \left(\frac{1}{2\varepsilon} \|1 - \varphi\|^2 + \frac{\varepsilon}{2} \|\nabla\varphi\|^2 \right)
\end{aligned} \tag{6.5}$$

Here, φ_+ is the maximum of φ and 0, $\kappa \approx 0$ (determined by machine precision) is a positive regularization parameter for the elastic energy and the length-scale parameter ε denotes the width of the transition zone in which φ changes from 0 to 1 (this width is illustrated as the contour lines between the white and brown regions in Fig. 6.1). One can see from **Eqn. 6.5** that if φ is 0 (fracture), the first and second terms become zero and the energy functional is dominated by the critical energy release rate G_c . Similarly when φ is 1, the third term becomes zero. An intermediate behavior can be seen for values between 0 and 1. Finally, we impose the irreversibility constraint (assumption (1)) on φ ; i.e.,

$$\partial_t \varphi \leq 0, \tag{6.6}$$

which ensures that the state variables change in the direction of energy minimization or entropy maximization, in accord with the 2nd law of thermodynamics. Then, the final energy functional reads:

$$\begin{aligned}
E_\varepsilon(u, \varphi) = & \frac{1}{2} \int_{\Omega} ((1 - \kappa)\varphi_+^2 + \kappa)\sigma_E : e(u) - \frac{1}{2} \int_{\Omega} \alpha_B(p - p_0)\varphi_+^2 \nabla \cdot u \\
& + G_c \left(\frac{1}{2\varepsilon} \|1 - \varphi\|^2 + \frac{\varepsilon}{2} \|\nabla\varphi\|^2 \right) + I_{K(\varphi^{n-1})}(\varphi),
\end{aligned} \tag{6.7}$$

where the last term $I_{K(\varphi^{n-1})}(\varphi^n)$ is a penalization term to impose the irreversibility constraint (6.6). We are now ready to derive differential equations

in a Galerkin fashion that can be easily adapted and implemented in legacy reservoir simulators using finite element discretizations. For the sake of brevity, we directly introduce these differential equations. The reader is referred to Mikelić et al. (2013a) for a detailed derivation. The problem statement then reads: Find u and φ such that,

$$\int_{\Omega} ((1 - \kappa)\varphi_+^2 + \kappa) \mathcal{G}e(\eta) : e(w) - \int_{\Omega} (\alpha_B - 1)(\varphi_+^2 p \operatorname{div} w) + \int_{\Omega} \varphi_+^2 \nabla p w = 0$$

$$\forall \text{ admissible test functions } w,$$
(6.8)

as well as,

$$\int_{\Omega} (1 - \kappa)(\varphi_+ \mathcal{G}e(\eta) : e(\eta)\psi - \int_{\Omega} 2(\alpha_B - 1)(\varphi_+ p \operatorname{div} \eta)\psi + 2 \int_{\Omega} \varphi_+ \nabla p \eta \psi$$

$$+ G_c \left(- \int_{\Omega} \frac{1}{\varepsilon} (1 - \varphi)\psi + \int_{\Omega} \varepsilon \nabla \varphi \nabla \psi \right)$$

$$+ \int_{\Omega} (\Xi + \gamma(\varphi - \varphi^{n-1}))^+ \psi = 0 \quad \forall \text{ admissible test functions } \psi.$$
(6.9)

Here, Ξ and γ are a penalization function and parameter, respectively, to enforce the irreversibility constraint of crack growth with the help of an augmented Lagrangian formulation (Wheeler et al. (2014a)). In the last term, φ^{n-1} denotes the phase-field solution to the previous time step.

6.2.2 Fluid-filled fracture propagation model (three-field problem)

In the previous section, a given uniform fracture pressure was assumed for crack propagation. Here we briefly describe an extension of this approach where a pressure field is computed by solving a flow problem on the entire domain (both reservoir and fracture). An extended Reynold's lubrication

equation and Darcy's law are solved in the fracture and reservoir domains, respectively along with the fluid mass conservation equations. The benefit of our proposed approach is that both sets of equations have similar structure identified by the phase-field variable as separate fracture ($\Omega_F(t)$) and reservoir ($\Omega_R(t)$) domains. Here, $\Omega_F(t)$ is the volume approximation of the crack \mathcal{C} . The reader is referred to Mikelić et al. (2014a). The mass conservation equations for fluid flow are:

$$\begin{aligned} \partial_t \rho_F + \nabla \cdot (\rho_F v_F) &= q_F - q_L \quad \text{in } \Omega_F(t), \\ \partial_t (\rho_R \phi_R) + \nabla \cdot (\rho_R v_R) &= q_R \quad \text{in } \Omega_R(t). \end{aligned} \tag{6.10}$$

Please note that the fracture porosity is set to one. The fracture volume is accounted for by the spatial discretization. Here, the velocities are defined by the Reynold's lubrication equation and Darcy's law for the fracture and the reservoir, respectively:

$$z_j = -\frac{K_j}{\nu_j} (\nabla p_j - \rho_j g). \tag{6.11}$$

The term q_L represents the leakage from the fracture owing to the 3D approximation of 2D Reynold's lubrication equation for the fracture domain. Where, $j = F, R$ denotes the fracture and reservoir domains, ϕ_j the fluid fraction, K_j the permeability tensor, ν_j and ρ_j the fluid viscosity and density, respectively, g the gravity and q_j the source/sink term. A comparison of Darcy's law and Reynold's lubrication equation shows that $K_F = \frac{w(u)^2}{12\mu}$, where $w(u)$ is the fracture width (or aperture) calculated from jump in normal displacements u . A detailed derivation of the leakage term can be found in Mikelić et al. (2014a).

6.2.3 Discretization and solution algorithm

The flow and mechanics equations are solved using the fixed-stress iterative coupling scheme (Settari and Walters (2001); Mikelić and Wheeler (2012)) and is described in detail in the algorithmic flow chart 1. We then first discretize in time using a backward Euler scheme followed by spatial discretization with a continuous Galerkin finite element method on a hexahedral grid with grid size parameter h . Here, all variables are discretized by continuous bilinears in space. We note that $h \ll \varepsilon$, which requires fine meshes around the fracture(s). To this end, we use local mesh refinement with hanging nodes (see Figure 6.3).

6.3 Integrating Phase-field Crack Propagation and Fractured Reservoir Flow Models

In this section, we describe the proposed coupling method while outlining a work-flow for translating fracture location, geometry and width information between the phase-field crack propagation model and the production reservoir code. The use of hexahedral elements for spatial discretization in both models allows translation of fracture location and variables from one model to another. The phase-field with crack growth and localized flow is used as a pre-processor step for the fractured reservoir flow. This results in a forward solution with the pertinent fracture geometry and width translated at the end of the propagation.

We consider phase-field as an independent module that can be coupled

Algorithm 1 Augmented Lagrangian fixed-stress solution algorithm

For each time t^n

repeat

Solve augmented Lagrangian loop (outer loop)

repeat

Solve two-field fixed-stress (inner loop):

Solve the pressure diffraction Problem (6.10)

Solve linear elasticity in Problem (6.8)

until Stopping criterion

$$\max\{\|u^l - u^{l-1}\|, \|p^l - p^{l-1}\|\} \leq \text{TOL}_{\text{FS}}, \quad \text{TOL}_{\text{FS}} > 0$$

for fixed-stress split is satisfied

Solve the nonlinear phase-field in Problem (6.9)

Update

$$\Xi_{k+1} = (\Xi_k + \gamma(\varphi_{k+1} - \varphi^{n-1}))_+, \quad k = 0, 1, 2, \dots$$

until Stopping criterion

$$\|\Xi_{k-1} - \Xi_k\| \leq \text{TOL}_{\text{AL}}, \quad \text{TOL}_{\text{AL}} > 0$$

is satisfied

Set: $(u^n, \varphi^n) := (u_k, \varphi_k)$.

Increment $t^n \rightarrow t^{n+1}$.

to other codes. This assumes hydraulic fracture growth to be a local or near well bore phenomenon which is not affected by far-field reservoir complexities such as reservoir boundaries, faults and barriers. Under this assumption, the two processes: hydraulic fracturing and later production are decoupled. Thus a local flow problem with appropriate boundary conditions is solved to compute a local pressure field during fracture propagation. There are two possible approaches for coupling phase-field crack propagation and fractured-reservoir flow model:

1. Phase-field with crack growth and localized flow as a pre-processor step for the fractured reservoir flow. This results in a forward solution with the pertinent fracture geometry and width translated at the end of the propagation. This approach considers phase-field as an independent module that can be coupled to other codes.
2. Phase-field for crack growth with fractured reservoir flow model for fluid flow computations leading to a stronger coupling between the two models.

In this work, we restrict ourselves to the first coupling approach and consider the second one in a future work. The second approach accounts for these far-field reservoir features owing to pressure field calculations using the global fractured-reservoir flow model. A stronger coupling requirement leads to higher computational costs in simulations and implementation. We discuss step by step the coupling approach used to integrate the two models. This

forward coupling is computationally inexpensive and adequately captures local flow field variations effecting fracture growth. Another advantage is that the phase field crack propagation model generates fracture growth information as a standalone module.

The spatial and temporal scales associated with fracture growth and later production from a hydraulically fractured reservoir are widely different. Therefore, it is reasonable to treat the two processes separately. As discussed previously, the phase-field model includes a localized fluid flow description and can therefore generate crack growth information as a stand alone. We then post-process and adapt this crack geometry data for our fractured poroelastic reservoir simulator resulting in a one-way coupling. This approach can be adapted for other legacy reservoir simulators.

6.3.1 Projection of variables/ mesh reconstruction

We start with the phase-field approach and solve for p, u, φ . At the end of the fracturing process, the reservoir simulator needs the pressure p as initial pressure, φ to detect the shape of the fracture and finally the width $w := w(u)$, which is computed as jump of the normal displacements. The shape of the fracture is determined for all $\varphi < thr$, where thr denotes a certain threshold, say $thr = 0.1$ (see Figure 6.3). If $\varphi < thr$ in a cell, it is marked as fracture cell. All unknown quantities are computed at cell centers with the associated co-ordinate information to the reservoir simulator.

We post-process and adapt fracture geometry from crack growth model

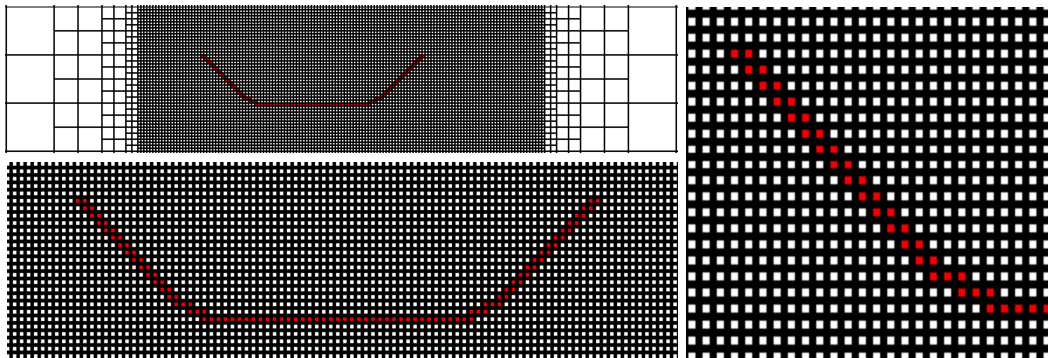


Figure 6.3: Determination of crack shape using threshold of the phase field variable to determine fracture cells (marked red). The phase-field module uses locally-refined grids with hanging nodes, which allows to reduce the computational cost significantly.

for the fractured poroelastic reservoir flow model. Fig. 6.4 shows reconstruction of a coarse, locally distorted, hexahedral mesh which adequately captures the three characteristic length scale variations of a typical elliptic fracture. Fig. 6.5 outlines a work-flow for reconstructing 3D fracture geometry, for

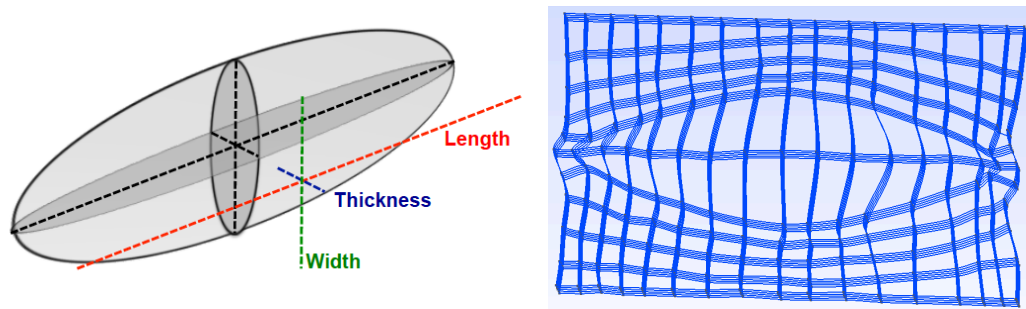


Figure 6.4: Reconstructing the fracture geometry.

reservoir flow simulation, from 2D fracture information generated by the fracture growth model. The first row shows geometry information for one and

three fractures (left and right, respectively) in the YZ plane. A typical fracture growth pattern, in the XZ plane is then used to reconstruct 3D fracture geometries. We use the fact that final fracture geometries after slick water injection are strongly correlated to reservoir rock property data and can therefore be scaled.

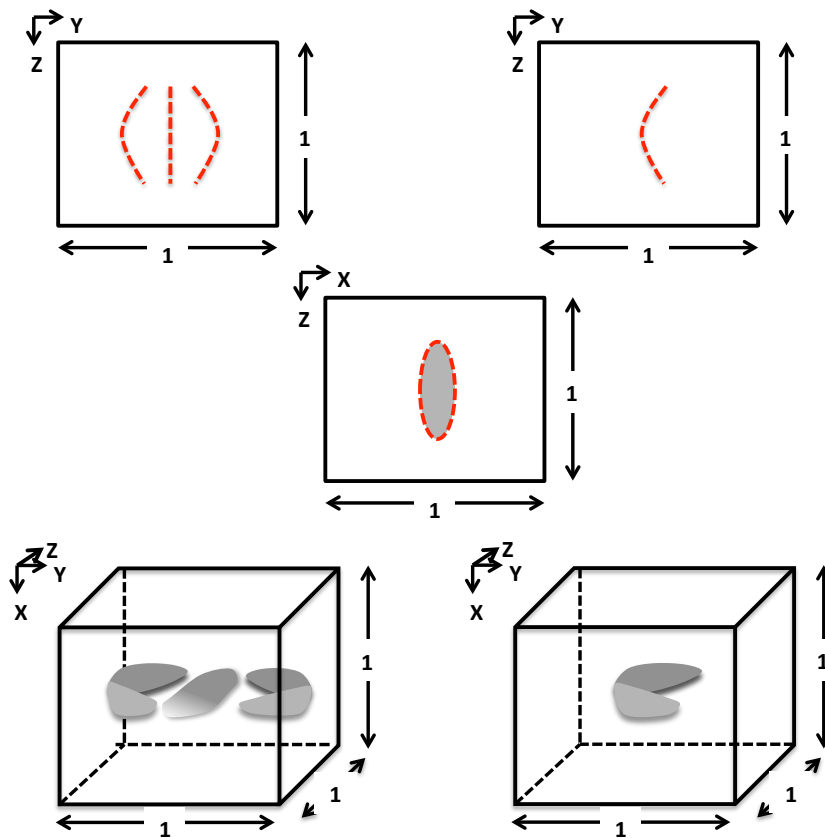


Figure 6.5: Work-flow for reconstructing 3D fracture geometry from 2D information.

6.3.2 Fractured well model

As previously described, the crack propagation model already couples fracture flow to reservoir and is therefore complete in itself. That means, starting with a given setting, we commence with that model and compute a fracture geometry, which might include curvilinear growth, branching and joining. The fracture geometry is passed to the reservoir simulator, as described in the previous section. The width and the pressure information from the phase-field model are set as the initial conditions for the reservoir simulator. Fig. 6.6 (right) shows fractured well placement (red blocks) in a reservoir with natural fractures (shaded orange). The mesh adaption is convenient since both models utilize hexahedral meshes thus avoiding computationally costly interpolation between meshes with different mesh elements (tetrahedral, prisms etc.).

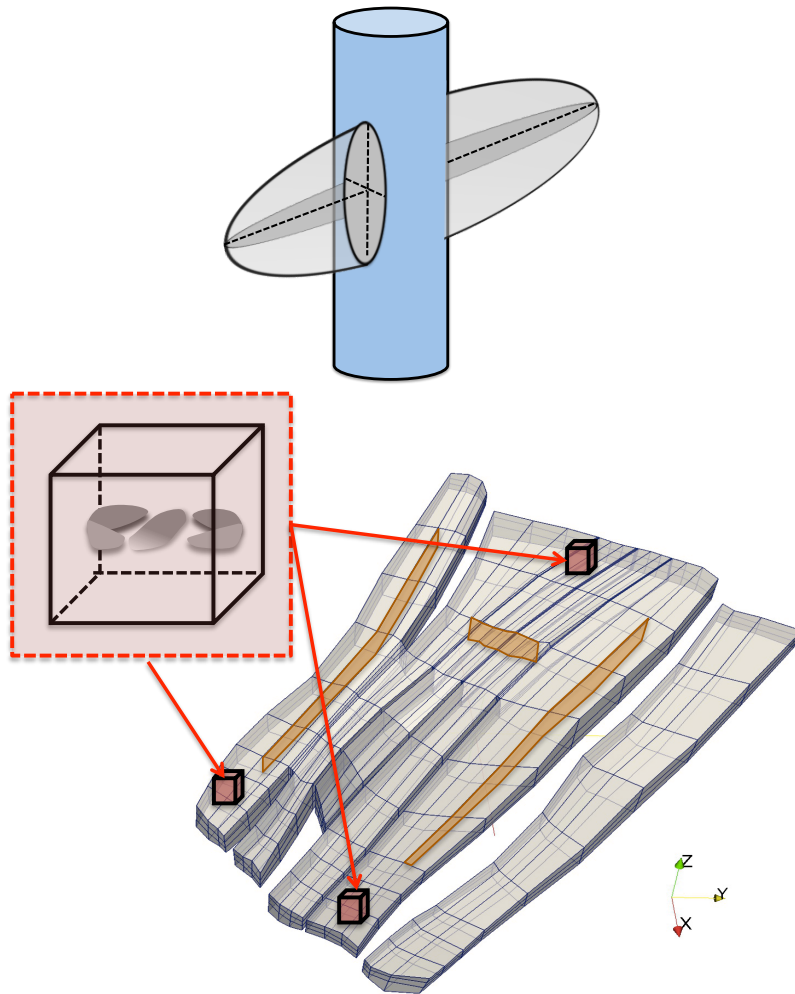


Figure 6.6: Integrating fractures generated by phase field model as a fractured well model.

The key advantage of our suggested ideas is concerned with the effort in coupling. Rather than iterating in each time step between both frameworks, the phase-field is used as a preprocessor step and as such acts as a own module. This allows us to run different well placement scenarios with the reservoir sim-

ulator using the same fracture geometry avoiding redundant fracture growth calculations for each scenario. The accuracy of the phase-field approach for modeling fracture propagation increases, as the mesh is refined.

The spatial and temporal scales associated with crack propagation are much smaller when compared to reservoir flow. Therefore, the use of a fine mesh for fracture growth computations followed by reservoir flow calculations on a coarse mesh is computationally efficient. In order to expedite the calculations for the phase-field fracture growth model, we utilize a dynamic mesh refinement approach with locally refined grids and hanging nodes (see **Fig. 6.3**). For example, if we run 20 time steps, we perform the first 15 on a coarse mesh and refine the last 5 time steps to get more accurate fracture tip and associated variable information. This procedure keeps the computational cost very reasonable while increasing accuracy.

6.4 Results

We illustrate our methodology by several numerical tests in two and three dimensions. First, we highlight the capabilities of the fractured-well phase-field model and present some crack propagation scenarios including multi-stage fractures, stress-shadowing effects and crack growth in heterogeneous porous media with nonplanar fractures. Second, we use one of these scenarios, extract the fracture and run the reservoir simulator.

The fracture-well phase-field model is computed with the multiphysics template (Wick (2013)) in combination with deal.II's (Bangerth et al. (2012))

step-31 for the usage of two different degree-of-freedom-handlers to build an iterative solution algorithm as needed for the fixed-stress splitting. In the following, we provide geometry information and parameters for the test cases.

Geometry, grid and time step parameters

The computational domain for all 2d tests is $\Omega = (0, 4)^2$. Here, two fractures each with length 1 and midpoints $x = 1.5$ and $x = 2.5$ are prescribed. In the second test, the distance is enlarged and the midpoints are $x = 1$ and $x = 3$. In the cases of the three multi-stage fractures, we consider the midpoints $x = 1, 2, 3$. Here, in the first test all three fractures have length 1, in the second test the middle fracture has length 0.5 and in the final test 1.5. In 3d, in the cube $\Omega = (0, 10)^3$, we prescribe a two penny-shape cracks with radius $r = 1.0$ in the $y = 5.0$ -plane with mid-points $(5.0, 3.0, 5.0)$ and $(5.0, 7.0, 5.0)$. The crack is approximated as a volume by extending it with the spatial discretization parameter h in up- and downward y -direction, respectively (for details, we refer the reader to Wheeler et al. (2014a)). As boundary conditions we set the displacements zero on $\partial\Omega$. We compute 50 (2d) and 50 (3d) time steps with time step size $\Delta t = 0.01$ (2d) and $\Delta t = 0.005$ (3d), respectively. We note that the characteristic fracture time scale is,

$$T_F = \frac{L^2 \eta_F c_F}{\tilde{K}_F} = \frac{1 \times 10^{-3} \times 10^{-8}}{10^{-8}} = 10^{-3},$$

in which we assumed a characteristic fracture length 1 and characteristic fracture permeability $\tilde{K}_F = 10^{-4}$.

Model parameters

The augmented Lagrangian penalization parameter is $\gamma = 10^4$ (2d) and $\gamma = 10^3$ (3d). Several parameters and geometry-related issues depend on the spatial mesh size parameter h . Namely, for the regularization parameters we choose the relations $\kappa = 10^{-6} \times h, \varepsilon = 2h = 0.088$ (2d) and $\kappa = 10^{-6} \times h, \varepsilon = 2h = 1.09$ (3d).

Flow parameters

In all examples, the gravity g is set to zero and the fluid is only driven by the point source injection q . We inject fluid at a constant rate into the fractures. In 2d and 3d, we use $q = 1$. Furthermore, the permeability in the reservoir is $K_R = 10^{-12}$. In the the second example, Test 2, we use a randomly varying permeability between 5×10^{-12} and 10^{-13} . Next, $M = 2.5 \times 10^{-8}$, $c_F = 10^{-8}$, $\nu_R = \nu_F = 1.0 \times 10^{-3}$, $\rho_R^0 = \rho_F^0 = 1$. Regarding the Biot coefficient, we perform computations with $\alpha = 0$ because it has been shown in Mikelić et al. (2014a) that $\alpha = 0$ and $\alpha = 1$ yield the same crack patterns if the characteristic time scale of the fracture is taken into account.

Elasticity and phase-field parameters

The fracture toughness is chosen as $G_c = 1.0$. The mechanical parameters are $\mu = 4.2 \times 10^7$ and $\lambda = 2.8 \times 10^7$. In the second example, we employ randomly varying Lamé parameters $\mu = 4.2 \times 10^6 - 9.4 \times 10^7$ and $\lambda = 2.6 \times 10^6 - 9.3 \times 10^7$.

6.4.1 Comparing fracture propagation in 3D and 2D domains

In this example, we first show a numerical experiment simulating simultaneous propagation of two penny-shaped fractures in a 3D domain. This is followed by a 2D experiment, in a similar setting, to compare 2D and 3D results. Fig. 6.7 shows fracture patterns during growth at $T = 0, 15$ and 25 seconds for the 3D case. Similarly, Fig. 6.8 shows fracture locations at $T = 0, 20$ and 30 seconds for the 2D case.

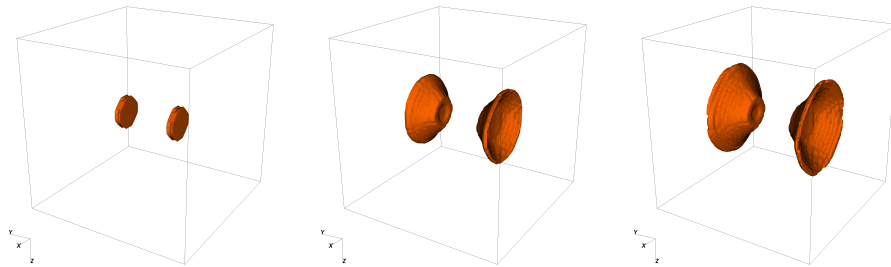


Figure 6.7: Crack pattern for simultaneous propagation of two penny-shaped fractures at $T = 0, 15$ and 25 seconds in 3D domain.

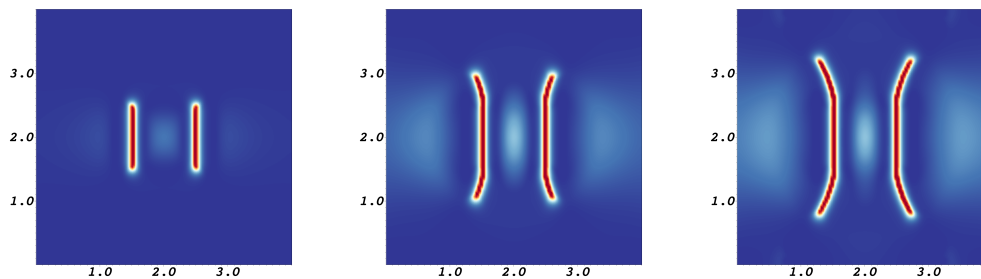


Figure 6.8: Crack pattern for simultaneous propagation of two fractures at $T=0, 20$ and 30 seconds in a 2D domain.

Since the two cases presented here are symmetrical the temporal variation of pressures at the centers of the two fractures, for each case, are similar. Figs. 6.9 and 6.10 shows the time evolution of pressure at the center of one of the fractures for the 3D (top) and 2D (bottom) domains.

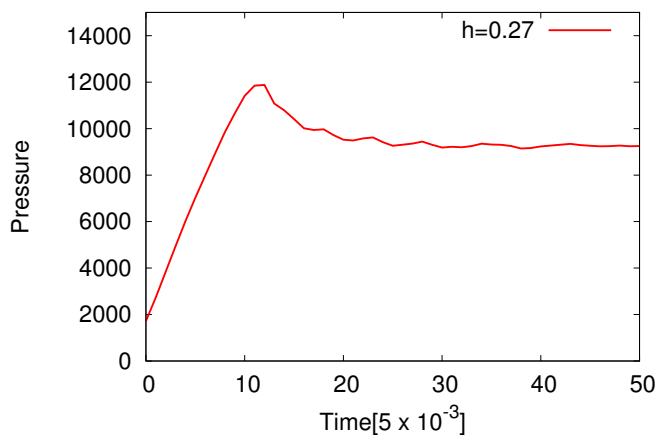


Figure 6.9: Transient pressure at the center of the fractures for 3D case.

Note that the pressure builds up to threshold value and then starts dropping as the fracture starts growing. The results show resemblance of the fracture growth and transient pressure for the 3D and 2D cases.

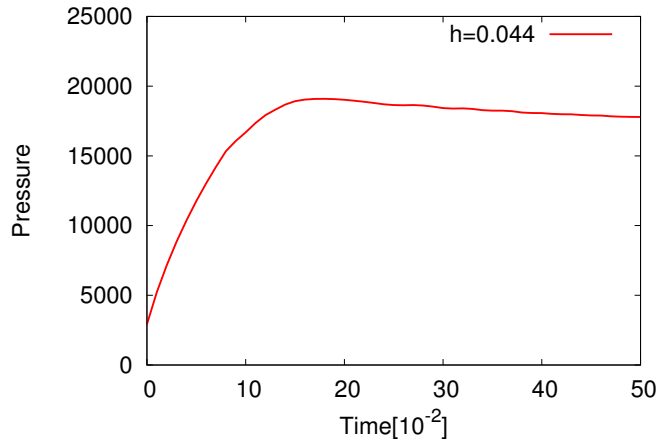


Figure 6.10: Transient pressure at the center of the fractures for 2D case.

6.4.2 Effect of fracture spacing on fracture growth

In this section, we present a numerical experiment, similar to the 2D case presented earlier, with a larger initial fracture spacing and studying the resulting effect on the fracture pattern. The fracture locations at time $T = 0$, 20 and 20 seconds are shown in Fig. 6.11. It can be observed by comparing Figs. 6.10 and 6.11 that as the spacing is reduced the fracture pattern becomes diverging. This result demonstrates that an optimal fracture spacing can be achieved which maximizes reservoir fracture interface area and therefore productivity.

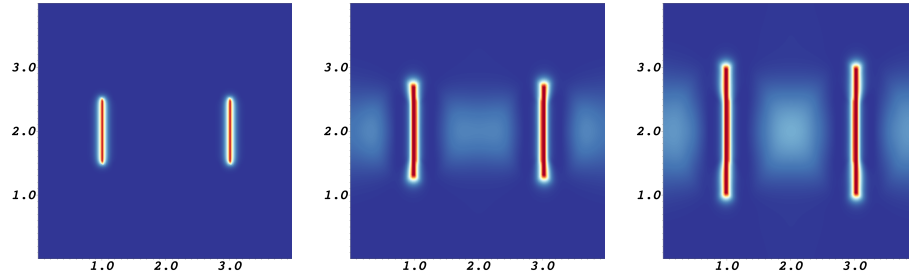


Figure 6.11: Crack pattern for simultaneous propagation of two fractures, with larger spacing, at $T=0$, 20 and 30 seconds.

6.4.3 Effect of discrete fractures on fracture growth

In this example, we study the effect of an existing fracture on the propagation of another fracture. This setting is devised to provide insight into growth patterns for sequential hydraulic fracturing. In Fig. 6.12 the left fracture is stationary whereas the right fracture grows due to injection of hydraulic fluids. The stationary fracture (left) is given a higher material stiffness property compared to the reservoir in order to replicate a propped fracture. As it can be seen, the hydraulic fracture does not show considerable pattern change due to the presence of an adjacent discrete fracture. Although a more detailed study can be conducted to evaluate the combined effect of orientation, we restrict ourselves to the case of parallel fracture for the sake of brevity. Fig. 6.13 shows the stress fields (Frobenius norm) at times $T = 0$, 20 and 40 seconds.

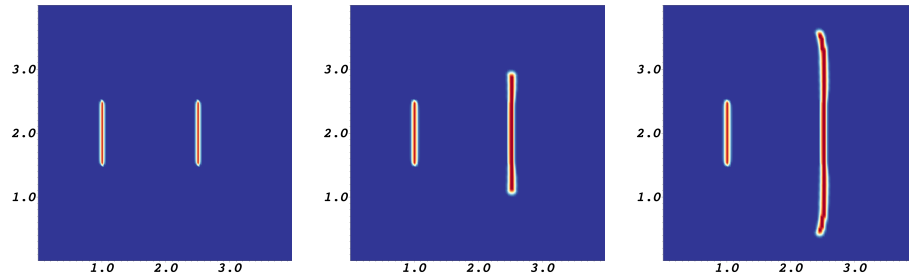


Figure 6.12: Crack pattern for sequential hydraulic fracturing at $T=0$, 20 and 40 seconds.

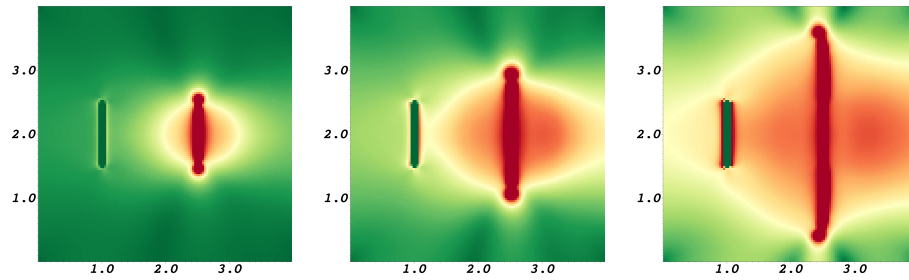


Figure 6.13: Stress field for sequential hydraulic fracturing at $T=0$, 20 and 40 seconds.

6.4.4 Effect of heterogeneity on fracture growth

In this set of tests, we extend the case of two simultaneous fracture propagation in a 2D domain to a heterogeneous porous media Fig. 6.15 and non-constant reservoir permeabilities Fig. 6.16. Fig. 6.15 and Fig. 6.16 show fracture growth with branching and joining for different times.

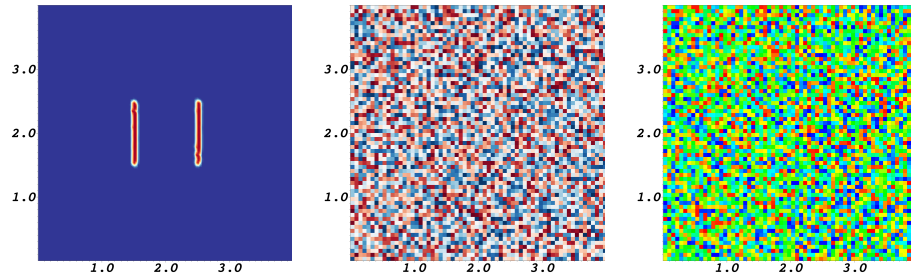


Figure 6.14: Initial crack pattern (left), randomly distributed Lamé coefficients (middle) and non-constant permeability (right). In the two latter figures, red denotes high values and blue/green low values.

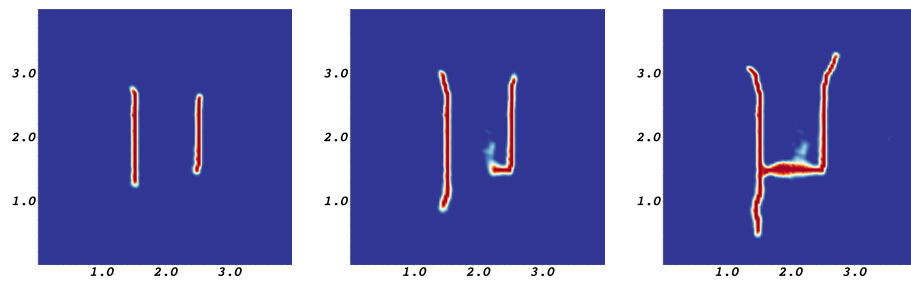


Figure 6.15: Crack pattern for fracture propagation in a heterogeneous medium at $T = 20, 30, 50$ seconds.

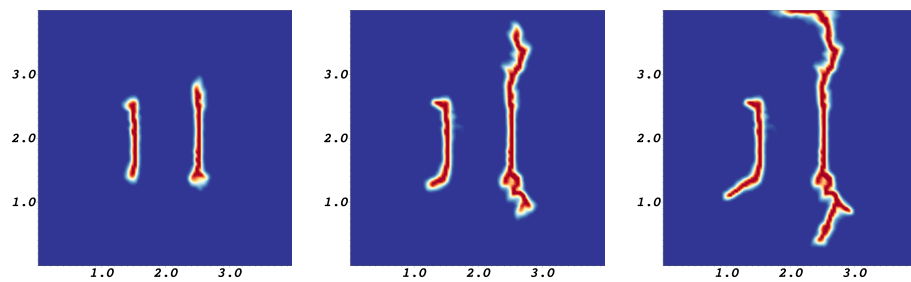


Figure 6.16: Crack pattern for fracture propagation in a heterogeneous medium and non-constant permeability at $T = 5, 10$ and 15 seconds.

6.4.5 Effect of stress shadowing on fracture growth

Here, we investigate the effect of stress-shadowing and initial fracture nucleation lengths on fracture growth for simultaneous propagation of three fractures. The material properties (Lameé parameters) are kept homogenous to accentuate observations and are by no means restrictive. Three cases were considered: a) equal fracture nucleation lengths (Fig. 6.17), b) shorter nucleation length for middle fracture (Fig. 6.19) and c) longer nucleation length for middle fracture (Fig. 6.21). Please note that although boundary conditions play an important role in fracture growth the emphasis here is solely on fracture-fracture interaction.

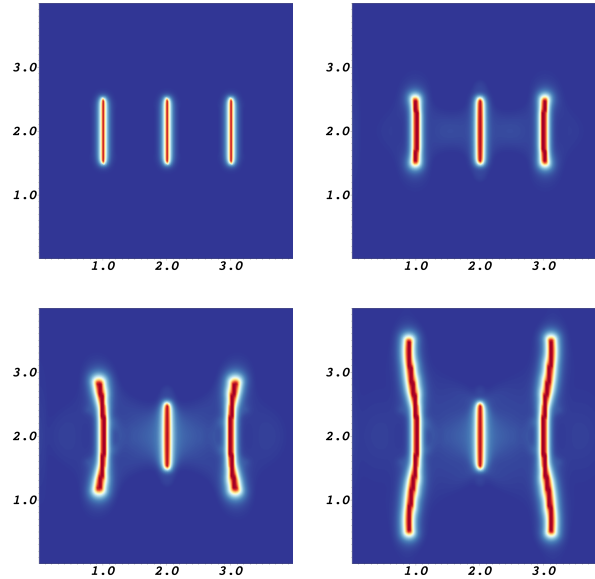


Figure 6.17: Example 3, Test 1, crack pattern at $T = 0, 20, 30, 50$.

Figs. 6.18, 6.20 and, 6.22 show the stress-fields (Frobenius norm) for

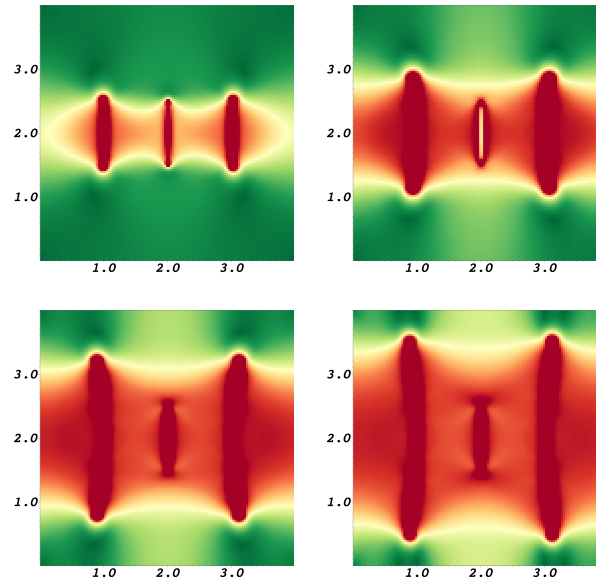


Figure 6.18: Example 3, Test 2, stress distribution at $T = 0, 20, 30, 50$.

the aforementioned three cases. In, Fig. 6.17 we observe that the growth of the middle fracture is shunned due to the stress shadowing from the outer two fractures. Similar behavior is observed for the case with shorter nucleation length for middle fracture. However, the case with longer nucleation length for middle fracture shows contrasting behavior. Here the stress shadow owing to the middle fracture shuns the growth of outer fractures. This numerical test shows that a careful evaluation of stress shadowing effects is pivotal for planning a hydraulic fracturing job, beginning from perforation to propagation using slick water injection.

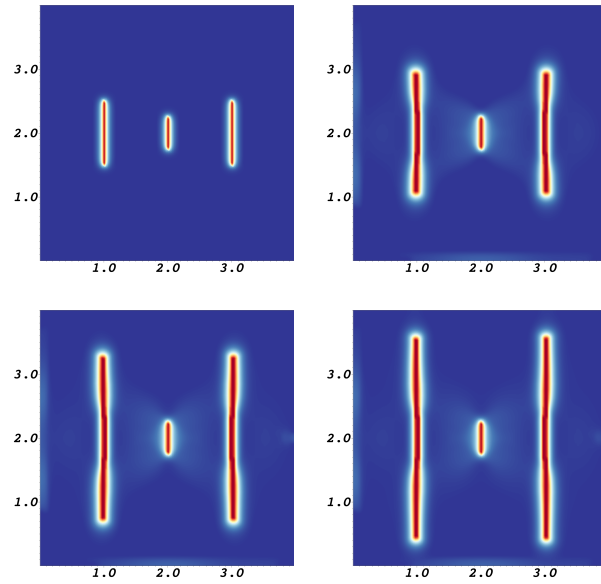


Figure 6.19: Example 3, Test 2, crack pattern at $T = 0, 20, 30, 50$.

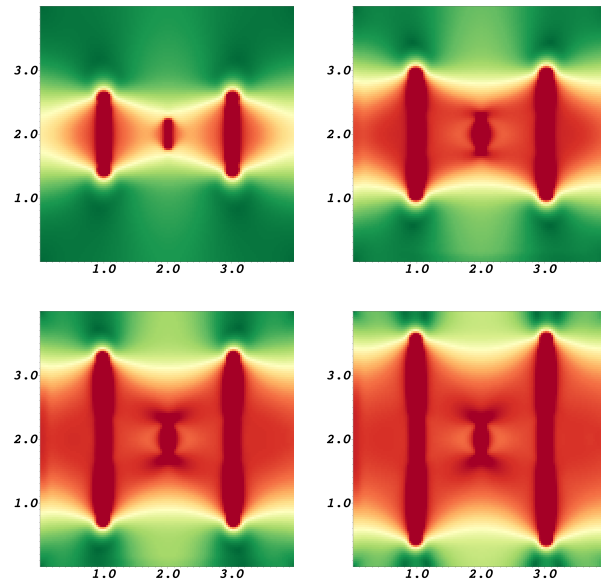


Figure 6.20: Example 3, Test 2, stress distribution at $T = 0, 20, 30, 50$.

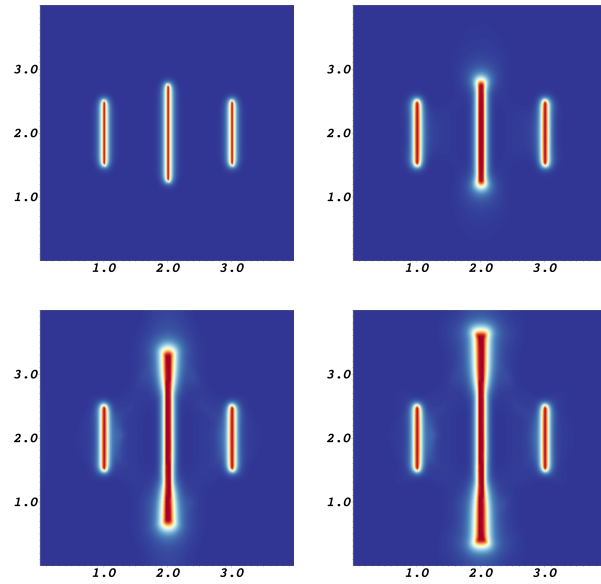


Figure 6.21: Example 3, Test 3, crack pattern at $T = 0, 20, 30, 50$.

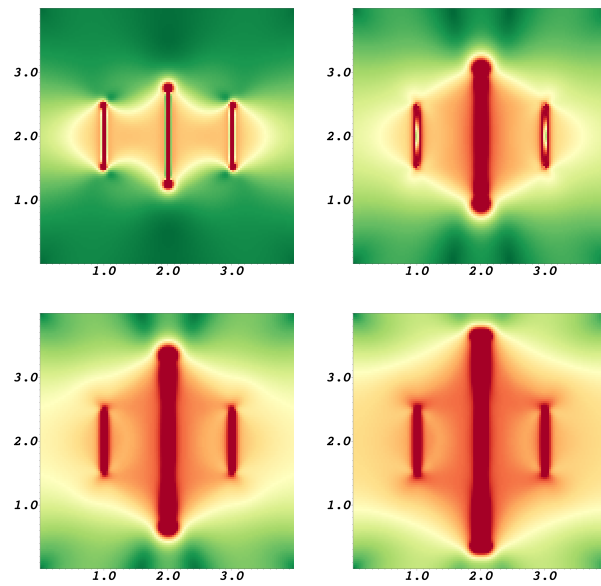


Figure 6.22: Example 3, Test 3, stress distribution at $T = 0, 20, 30, 50$.

6.4.6 Coupling the phase-field model to a reservoir simulator

In this section, we present an example to demonstrate the aforementioned approach for an explicit coupling of fracture growth to a reservoir simulator based upon general hexahedral discretization. Two synthetic cases are generated from Brugge field geometry (see e.g. Peters et al. (2009); Chen et al. (2010)) where the wells are either relocated or augmented with hydraulic fractures. Here the use of fractured wells reduces the number of injection wells while improving sweep efficiency. The phase field fracture propagation model, followed by production evaluation of reservoir, allows us to develop an intuitive understanding of recovery predictions and serves as a decision making tool for design, evaluation and long term field developments.

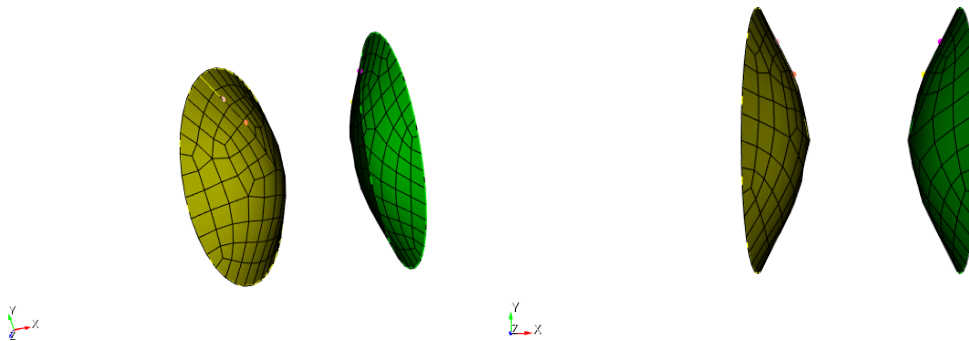


Figure 6.23: Coarse fracture mesh after adaptation.

Although not restrictive, for the sake of simplicity, we consider the fracture pattern as shown in Fig. 6.7. The geometry information from the phase field fracture propagation model is post-processed and adapted to obtain a coarser mesh while maintaining mesh quality. This reduces time-step size

| | | | |
|----------|--------------------------|----------------------|-------------------------|
| ϕ | 0.15-0.22 | $K_x \neq K_y = K_z$ | 0-3800 mD |
| c_w | 1.E-7 psi ⁻¹ | c_o | 1.E-4 psi ⁻¹ |
| ρ_w | 62.4 lbm/ft ³ | ρ_o | 56 lbm/ft ³ |
| ν_w | 1 cP | ν_o | 2 cP |
| S_w^0 | 0.31 | P_w^0 | 1500 psi |

Table 6.1: Brugge field: reservoir and fluid properties

restrictions and numerical errors associated with mesh elements. Fig. 6.23 shows the reconstructed, coarse, structured fracture mesh with quadrilateral (hexahedral in 3D) elements. This fracture pattern is integrated with a wellbore model and is used as a fractured well model in a reservoir simulator.

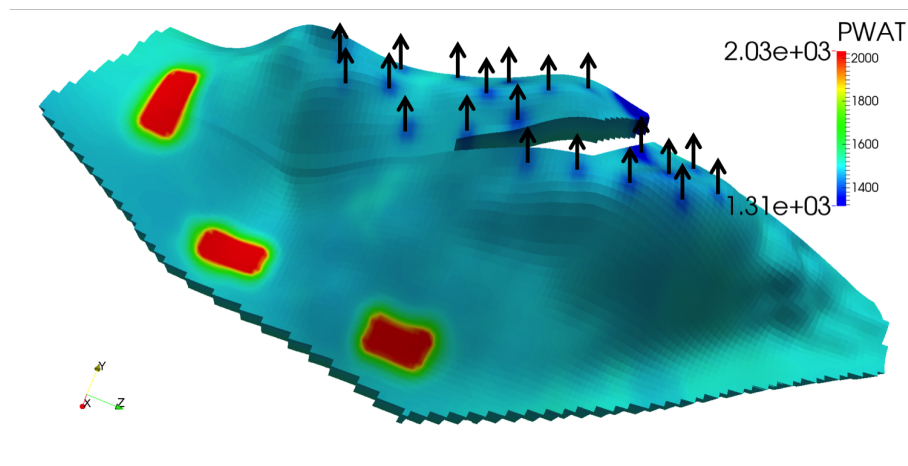


Figure 6.24: Brugge field geometry with fractured injection wells.

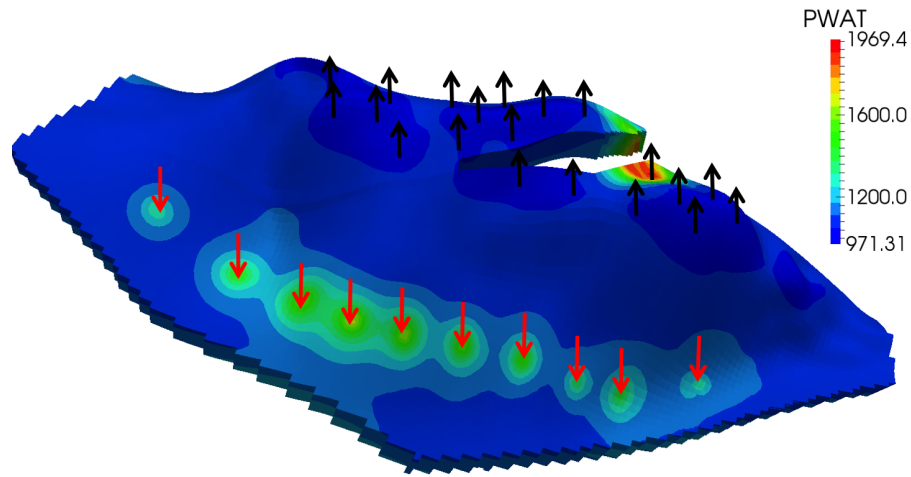


Figure 6.25: Original Brugge field with injection and production wells.

Table 6.1 provides material and fluid properties required for solving flow and geomechanics. The values presented in the table provide typical values used for this simulation run. Figure 6.24 shows the fractured Brugge field geometry with 20 bottom-hole pressure specified production wells at 1000 psi. Here a pressure profile after 2 days is used to aid in visualizing the location of the fractured injection wells. The three red regions show the hydraulically fractured, injection wells with a bottom-hole pressure specification of 2600 psi. The original Brugge field is shown in Fig. 6.25 with 30 bottom-hole pressure specified wells with 10 injectors at 2600 psi and 20 producers at 1000 psi where injectors are located at a higher elevation compared to the producers. The distorted reservoir geometry and fractures are captured using $9 \times 48 \times 139$ general hexahedral elements and then discretized using a MFMFE scheme

(Singh et al. (2014a)). Figure 6.26 and 6.27 displays permeability fields in the X, Y and Z directions.

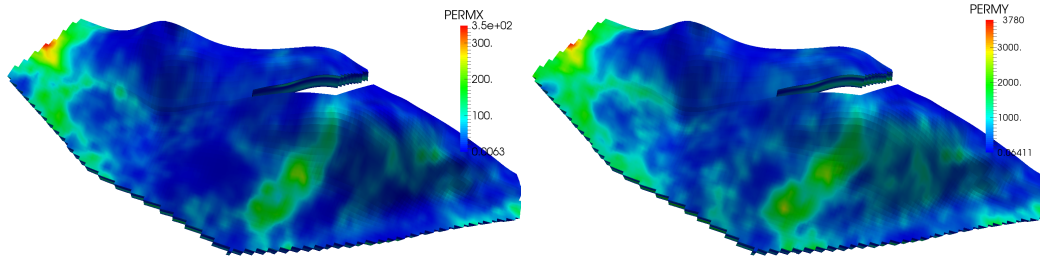


Figure 6.26: X (left) and Y (right) direction permeability fields.

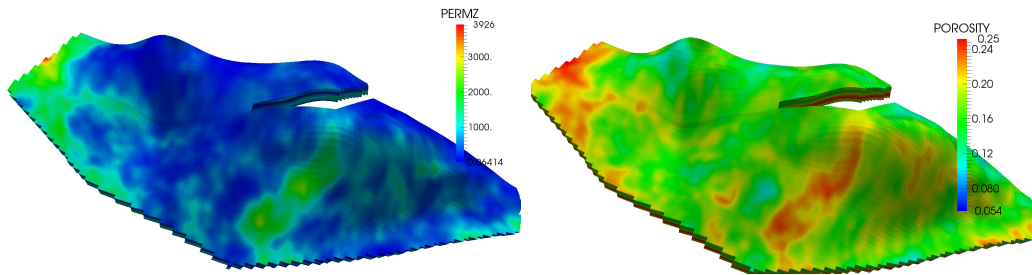


Figure 6.27: Z direction permeability (left) and porosity (right) fields.

Figs. 6.28 and 6.29 shows pressure and saturation profiles, respectively at the end of 1000 days. The fractured injection wells are placed at greater depths compared to production wells so that the gravity assists in oil recovery. A comparison between the pressure and saturation profiles for the two cases show that a lower number of fractured wells are required for improved sweep efficiencies compared to conventional wells.

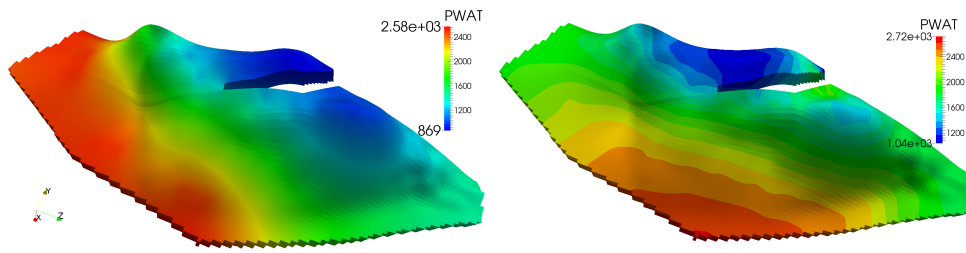


Figure 6.28: Pressure profiles after 1000 days for fractured (left) and original (right) Brugge field cases.

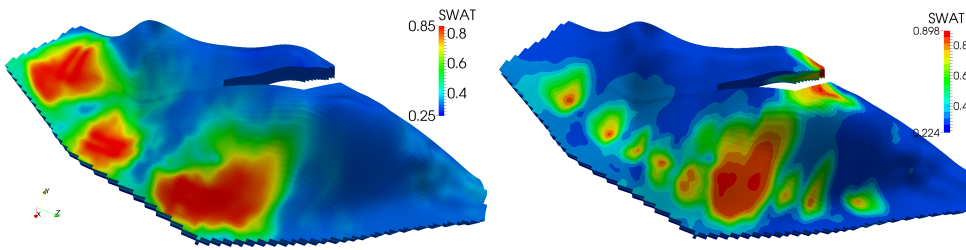


Figure 6.29: Saturation profiles after 1000 days for fractured (left) and original (right) Brugge field cases.

6.5 Nomenclature

| | | |
|----------------------------------|---|---------------------------------------|
| Ω | = | reservoir domain |
| \mathcal{C} | = | fracture domain |
| $E(u, \mathcal{C})$ | = | energy functional |
| σ_E | = | stress tensor |
| $e(u)$ | = | strain tensor |
| α_B | = | Biot coefficient |
| p | = | fluid pressure |
| p_0 | = | reference pressure |
| u | = | displacement vector |
| G_c | = | critical energy release rate |
| $\mathcal{H}^{d-1}(\mathcal{C})$ | = | length of fracture, Hausdroff measure |
| μ, λ | = | Lamé parameters |
| ν | = | fluid viscosity |
| I | = | identity tensor |
| φ | = | phase field variable |
| κ, ε | = | regularization parameters |
| $w(u)$ | = | fracture aperture or width |

- $K =$ absolute permeability
- $\rho =$ fluid density
- $g =$ acceleration due to gravity
- $q_{F,R} =$ source/sink for fracture (F) or reservoir (R)
- $q^L =$ fracture leakage term

Chapter 7

Conclusions and Recommendations

We developed a compositional flow model using MFMFE for spatial discretization. The use of general hexahedral grid leads to fewer number unknowns when compared to tetrahedral grids and therefore lower computational costs. Further the discretization scheme allows sufficient flexibility in capturing complex reservoir geometries including non-planar interfaces. The hexahedra is a plausible choice for mesh elements since reservoir petrophysical data is usually available on similar elements. An MFMFE scheme therefore facilitates adaptation with minimal changes to given information. Finally, the general compositional flow model presented here encompasses single, multi-phase and black oil flow models. This presents a future prospect for multi-model capabilities where different flow models can be used in separate reservoir domains.

A fractured poro-elastic reservoir model is also presented where the fractures are modeled as surfaces. The contrast between reservoir and fracture is fully resolved using different flow models and capillary pressure and relative permeability curves. A solution algorithm and numerical scheme based on MFMFE approximation has been described. The fracture geometry along with its non-planarity is accurately captured using general hexahedral ele-

ments. The model is validated against experimental lab data for spontaneous, capillary imbibition of a Berea sandstone core. Several numerical experiments, including a field case, have been performed which demonstrate that the recovery pattern is strongly influenced by the geometry and orientations of the fractures. These examples provide both qualitative and quantitative understanding of the underlying physical processes. The use of explicit flow models for both hydraulic and discrete fractures provide us with an accurate depiction of flow fields. This allows design and evaluation of hydraulic fracture jobs considering intricate details. Incorporating the geomechanical effects show that the influence of fractures on the stress field is more prominent around the production than the injection wells.

We successfully coupled this phase-field approach with a reservoir simulator. The integration is based on a computationally efficient one-way coupling which allows the use of the phase-field approach as a pre-processor step. With our proposed approach we are able to simulate hydraulic fracturing and production stages. An extension to black-oil and compositional models for the reservoir flow description can also be achieved.

Appendices

Appendix A

Wellbore Models

A.1 Introduction

This appendix presents horizontal and deviated well-bore models for slightly compressible two phase flow systems. The elements/grid-blocks containing well-bore are identified using an existing IPARS (Integrated Parallel Accurate Reservoir Simulator) algorithm for tracing vertical wells given the well-bore endpoints. For example, let us consider a horizontal/vertical well. Figure A.1 shows a vertical, horizontal and deviated (from left to right) well that communicates with the reservoir along a length L (shaded blue). The well specifications are usually made either point wise (bottom hole pressure) or at the well head as a mass/volume rate. A well model is therefore required to calculate a continuous distribution of pressure ,for given well specifications, as a function of distance from the bottom hole.

Well models are broadly classified into two categories: (1) bottomhole pressure specified and, (2) rate specified wells. An outline of the existing IPARS implementation of vertical well model is presented in order to familiarize the reader with the theoretical approach and assumptions behind its development. A description of horizontal well model theory and implemen-

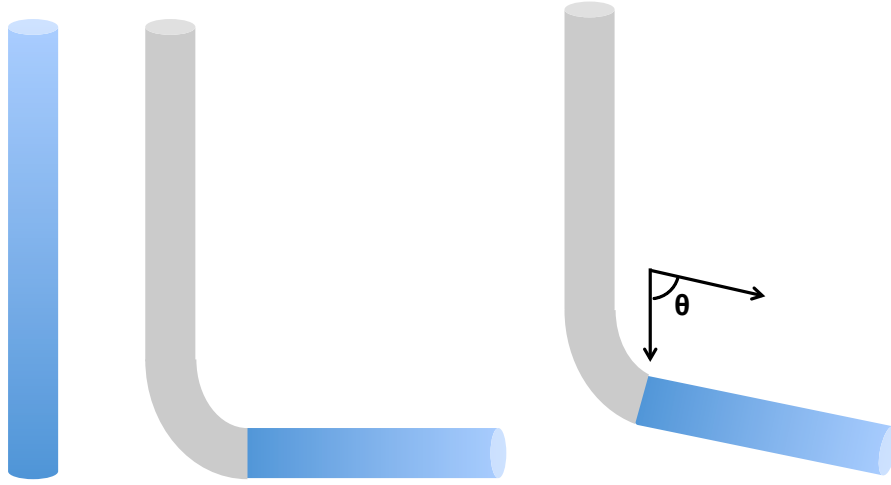


Figure A.1: Vertical, horizontal and deviated well (left to right)

tation is then presented following a brief discussion on the common factors between horizontal and vertical wells. Conventional wellbore models (Joshi; Economides et al.) calculate pressure distribution along well-bore based upon the type of well specification. The pressure drop (dP) across an incremental wellbore length (dL) is obtained from macroscopic energy balance given by eqn. (A.1).

$$\frac{dP}{dL_{Total}} = \frac{dP}{dL_{gravity}} + \frac{dP}{dL_{friction}} + \frac{dP}{dL_{inertia}} \quad (A.1)$$

A.2 Vertical Well Models

A number of assumptions are made during model development, listed as follows:

1. Frictional losses owing to the solid-fluid surface interactions are assumed to be negligible.
2. Inertial effects such as fluid acceleration due to expansion are neglected.
3. The fluid is assumed to be slightly compressible.
4. An average wellbore density (ρ_{WB}) equal to the density at the center of wellbore is assumed.
5. The system is considered to be isothermal assuming negligible throttling effect.
6. The well/reservoir interaction occurs along wellbore curved surface area.

First two assumptions imply that a hydrostatic equilibrium exists inside the wellbore given by eqn. (A.2) whereas, the third suggests that fluid density varies with pressure according to eqn. (A.3). The fourth assumption states the density averaging approach that exists for vertical well models. One must bear in mind that the last two assumptions are subjective. The model description may differ based upon the choice of incompressible, slightly or fully compressible fluid and the density averaging approach employed.

$$P + \rho gL = a \tag{A.2}$$

$$\rho = \rho_0 \exp[c(P - P_0)] \tag{A.3}$$

Here a is an arbitrary constant, c is the fluid compressibility. and ρ_0 is the reference density corresponding to a reference pressure P_0 .

Let us now consider a discretized reservoir where the wellbore intersects grid elements, as shown in figure A.2. Equation (A.2) can be rewritten for fluid inside the wellbore and adjacent formation given by eqns. (A.4) and (A.5), respectively. The fourth assumption provides the average wellbore density from eqn. (A.3) given by eqn. (A.6). The mass flow rate of phase ‘f’ from the wellbore to the grid element ‘i’ is given by eqn. (A.7), frequently referred as inflow performance relationship.

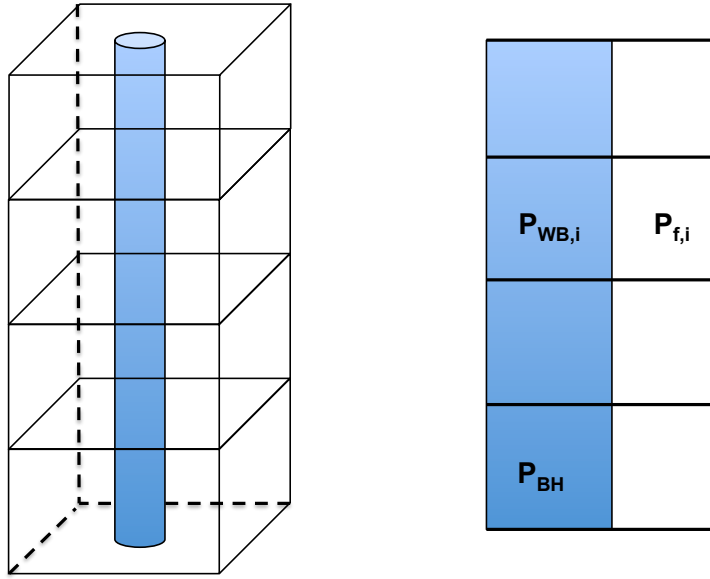


Figure A.2: Elements containing vertical well in a discretized reservoir

$$P_{WB,i} = P_{BH} + \rho_{WB}g(D_{WB,i} - D_{BH}) \quad (A.4)$$

$$\bar{P}_{f,i} = P_{f,i} + \rho_{f,i}g(D_{WB,i} - D_i) \quad (A.5)$$

$$\rho_{WB,f} = \rho_{o,f} \exp \left[c_f \left(P_{BH} + \rho_{WB,f} g \frac{\Delta h}{2} - P_o \right) \right] \quad (\text{A.6})$$

$$q_{f,i} = \rho_{f,i} G_i L_i K_i k_{f,i} (P_{WB,i} - \bar{P}_{f,i}) / \mu_{f,i} \quad (\text{A.7})$$

Here,

L_i = length of open wellbore intersecting element 'i'.

K_i = permeability of element 'i' normal to wellbore.

$k_{f,i}$ = relative permeability of phase 'f' in element 'i'.

G_i = dimensionless geometric factor.

$\rho_{f,i}$ = density of phase 'f' in element 'i'.

$\mu_{f,i}$ = viscosity of phase 'f' in element 'i'.

$\bar{P}_{f,i}$ = formation pressure of phase 'f' at the center of wellbore element 'i'.

$P_{WB,i}$ = wellbore pressure at the center of element 'i'.

P_{BH} = bottom hole pressure (specification).

$P_{f,i}$ = formation pressure of phase 'f' at the center of element 'i'.

$D_{WB,i}$ = depth at the center of wellbore element 'i'.

D_i = depth at the center of element 'i'.

D_{BH} = depth of bottom hole.

$\rho_{WB,f}$ = average wellbore density of phase 'f'.

$q_{f,i}$ = mass flow rate of phase 'f' entering/leaving element 'i'.

c_f = compressibility of phase 'f'.

Δh = total length of open wellbore.

A.2.1 Bottomhole Pressure Specified Wells

The wellbore pressure distribution for bottom hole pressure specified wells is rather straightforward. The average wellbore density is calculated directly from eqn. (A.6) followed by evaluation of pressure distribution using eqn. (A.4).

A.2.2 Rate Specified Wells

Rate specified wells present an added level of difficulty since neither bottom hole pressure nor average wellbore density is known. The specified total mass rate is related to the mass rate injected or produced from each element 'i' is given by eqn. (A.8).

$$q_{sc,f} = \sum_i q_{f,i} \quad (A.8)$$

Eqns. (A.5) thru (A.8) solved for P_{BH} results in eqn. (A.9). A pressure distribution is then obtained using a successive substitution approach as shown in figure A.3. A successive substitution type approach is adopted to solve equations (A.6) and (A.9) for the evaluation of pressure distribution. An initial guess for average wellbore density is given by eqn. (A.10).

$$P_{BH} = \left(\sum_i \frac{F_i k_{f,i} \rho_{f,i}}{\mu_{f,i}} \left[P_{f,i} + \rho_{f,i} g (D_{WB,i} - D_i) - \rho_{WB} g (D_{WB,i} - D_{BH}) \right] + q_{sc} \right) \frac{1}{\sum_i \frac{F_i k_{f,i} \rho_{f,i}}{\mu_{f,i}}} \quad (A.9)$$

$$\rho_{WB} = \frac{\sum_i F_i k_{f,i} \rho_{f,i}}{\sum_i \frac{F_i k_{f,i}}{\mu_i}} \quad (A.10)$$

Here, $F_i = G_i L_i K_i$, q_{sc} is the well mass rate specification and k is the successive substitution iterate.

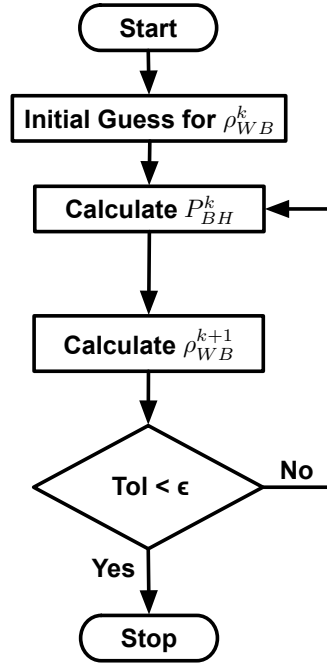


Figure A.3: Calculation of pressure distribution for rate specified vertical wells

A.3 Horizontal/Deviated Well Models

In this section, we formulate a general wellbore flow model which accounts for horizontal as well as deviated wells. A more general two phase flow model which accounts for changes in pressure distributions due to varying spatial distribution of fluid phases at a well bore cross section is given by Singh (2009). One of the primary differences between vertical and horizontal/deviated wells is the geometric factor (G_i), in Eqn. (A.7), for vertical

wells. The basic assumptions remain the same as vertical wells with an exception of frictional term which will be included hereafter in pressure distribution calculations. The gravity term disappears as we transition from vertical to deviated to strictly horizontal wells. The incremental pressure drop, assuming L is positive downwards, is then given by eqn. (A.11).

$$\frac{dP}{dL} = \rho \vec{g} - \frac{f_m \rho v^2}{2d} - \rho v \frac{dv}{dL} \quad (\text{A.11})$$

1. Inertial effects such as fluid acceleration due to expansion are neglected.
2. The pressure distribution is assumed to be invariant with respect to the spatial distribution of fluid phases at a given well bore cross section.
3. The fluid is assumed to be newtonian and slightly compressible.
4. A hydrostatic equilibrium is assumed inside the formation.
5. The system is isothermal.
6. The wellbore interacts with the reservoir along curved surface area.

For an injection well eqn. (A.11) reduces to eqn. (A.12) analogous to eqn. (A.4) for vertical wells discussed previously. The formation pressure and fluid density are given by eqns. (A.13) and (A.14), respectively in accord with assumptions two and three.

$$P_{WB,i} = P_{WB,i-1} + \rho_{WB,i} g (L_i) \cos(\theta) - f_m \rho_{WB,i} v_i^2 \frac{L_i}{2d} \quad (\text{A.12})$$

$$\bar{P}_{f,i} = P_{f,i} + \rho_{f,i} g (D_{WB,i} - D_i) \quad (\text{A.13})$$

$$\rho_{WB,i,f} = \rho_{o,f} \exp [c_f (P_{WB,i} - P_o)] \quad (\text{A.14})$$

The wellbore/reservoir interaction is accounted using an inflow performance relationship, expressed as eqn. (A.15). An additional mass conservation equation is required to form a consistent system given by eqn. (A.16).

$$q_{f,i} = \rho_{f,i} G_i L_i K_i k_{f,i} (P_{WB,i} - \bar{P}_{f,i}) / \mu_{f,i} \quad (\text{A.15})$$

$$v_i = v_{i+1} + \frac{q_{f,i} L_i}{2\pi r \rho_{WB,i}} \quad (\text{A.16})$$

Here f_m is the dimensionless friction factor, v_i is the average fluid velocity inside wellbore intersecting element ‘i’ and θ is the angle between deviated well with the gravity vector direction.

Equations (A.12) thru (A.16) form a consistent system which can be solved in a fully implicit manner to obtain a pressure distribution.

A.3.1 Bottomhole Pressure Specification

A bottom hole pressure specification implies a value $P_{WB,i}$ along the open wellbore is given. The value of P_{BH} is therefore set explicitly to the given value in the resulting Jacobian.

A.3.2 Rate Specified Wells

Similarly, a well rate specification implies a value of $q_{SC,f}$ is provided. Thus, a corresponding equation in the resulting jacobian must explicitly reflect this specification.

Appendix B

Phase Behavior Model: Derivatives

B.1 Peng-Robinson Cubic Equation of State

$$\bar{Z}_\alpha^3 - (1 - B_\alpha)\bar{Z}_\alpha^2 + (A_\alpha - 3B_\alpha^2 - 2B_\alpha)\bar{Z}_\alpha - (A_\alpha B_\alpha - B_\alpha^2 - B_\alpha^3) = 0 \quad (\text{B.1a})$$

$$Z_\alpha = \bar{Z}_\alpha - C_\alpha \quad (\text{B.1b})$$

$$A_\alpha = \sum_{i=2}^{N_c} \sum_{j=2}^{N_c} \xi_{i\alpha} \xi_{j\alpha} A_{ij} \quad (\text{B.1c})$$

$$A_{ij} = (1 - \delta_{ij})(A_i A_j)^{0.5} \quad (\text{B.1d})$$

$$A_i = \Omega_{ai}^o \left[1 + m_i(1 - T_{ri}^{0.5}) \right]^2 \frac{p_{ri}}{T_{ri}} \quad (\text{B.1e})$$

$$B_\alpha = \sum_{i=2}^{N_c} \xi_{i\alpha} B_i \quad (\text{B.1f})$$

$$C_\alpha = \frac{P^*}{RT} \sum_{i=2}^{N_c} \xi_{i\alpha} c_i \quad (\text{B.1g})$$

$$B_i = \Omega_{bi}^o \frac{p_{ri}}{T_{ri}} \quad (\text{B.1h})$$

$$C_i = \frac{P^* c_i}{RT} \quad (\text{B.1i})$$

$$p_{ri} = \frac{P^*}{P_{ci}} \quad (\text{B.1j})$$

$$T_{ri} = \frac{T}{T_{ci}} \quad (\text{B.1k})$$

$$\begin{aligned}
m_i &= 0.374640 + 1.54226\omega_i - 0.26992\omega_i^2 && \text{if } \omega_i \leq 0.49 \\
&= 0.379642 + 1.48502\omega_i = 0.164423\omega_i^2 + 0.016666\omega_i^3 && \text{if } \omega_i > 0.49
\end{aligned} \tag{B.2}$$

Here,

δ_{ij} = Binary interaction parameters between component ‘i’ and ‘j’ (constant).

p_{ci} = Critical pressure of component ‘i’ (constant).

T_{ci} = Critical temperature of component ‘i’ (constant).

ω_i = Accentric factor for component ‘i’ (constant, deviation of a molecule from being spherical).

C_α = Volume shift parameter (constant).

$\Omega_{\alpha/bi}^o$ = Constants corresponding to the equation of state.

Z_α = Compressibility of phase ‘ α ’.

B.2 Derivatives of Fugacity Equation

The fugacity equation is given by,

$$\begin{aligned}
\ln(\Phi_{i\alpha}) &= -C_i + \frac{B_i}{B_\alpha}(\bar{Z}_\alpha - 1) - \ln(\bar{Z}_\alpha - B_\alpha) \\
&\quad - \frac{A_\alpha}{2\sqrt{2}B_\alpha} \left(\frac{2 \sum_{j=2}^{N_c} \xi_{j\alpha} A_{ij}}{A_\alpha} - \frac{B_i}{B_\alpha} \right) \ln \left(\frac{\bar{Z}_\alpha + (1 + \sqrt{2})B_\alpha}{\bar{Z}_\alpha + (1 - \sqrt{2})B_\alpha} \right)
\end{aligned} \tag{B.3}$$

Further, for the sake of convenience we define Δ and Θ ,

$$\Delta = \frac{A_\alpha}{2\sqrt{2}B_\alpha} \left(\frac{2 \sum_{j=2}^{N_c} \xi_{j\alpha} A_{ij}}{A_\alpha} - \frac{B_i}{B_\alpha} \right) \tag{B.4a}$$

$$\Theta = \ln \left(\frac{\bar{Z}_\alpha + (1 + \sqrt{2})B_\alpha}{\bar{Z}_\alpha + (1 - \sqrt{2})B_\alpha} \right) \tag{B.4b}$$

B.2.1 Derivative with respect to pressure (P^*)

$$\begin{aligned}
\frac{\partial \ln(\Phi_{i\alpha})}{\partial P^*} = & -\frac{\partial C_i}{\partial P^*} + \left\{ \frac{(\bar{Z}_\alpha - 1)}{B_\alpha} \frac{\partial B_i}{\partial P^*} + \frac{B_i}{B_\alpha} \frac{\partial \bar{Z}_\alpha}{\partial P^*} - \frac{B_i}{B_\alpha^2} (\bar{Z}_\alpha - 1) \frac{\partial B_\alpha}{\partial P^*} \right\} \\
& - \frac{1}{(\bar{Z}_\alpha - B_\alpha)} \left\{ \frac{\partial \bar{Z}_\alpha}{\partial P^*} - \frac{\partial B_\alpha}{\partial P^*} \right\} - \Theta \left\{ \frac{1}{\sqrt{2} B_\alpha} \sum_{j=2}^{N_c} \xi_{i\alpha} \frac{\partial A_{ij}}{\partial P^*} \right. \\
& \left. - \frac{\sum_{j=2}^{N_c} \xi_{i\alpha} A_{ij} \partial B_\alpha}{\sqrt{2} B_\alpha^2 \partial P^*} - \frac{B_i}{2\sqrt{2} B_\alpha^2} \frac{\partial A_\alpha}{\partial P^*} - \frac{A_\alpha}{2\sqrt{2} B_\alpha^2} \frac{\partial B_i}{\partial P^*} - \frac{B_i}{\sqrt{2} B_\alpha^3} A_\alpha \frac{\partial B_\alpha}{\partial P^*} \right\} \\
& - \Delta \left(\frac{\bar{Z}_\alpha + (1 - \sqrt{2}) B_\alpha}{\bar{Z}_\alpha + (1 + \sqrt{2}) B_\alpha} \right) \left\{ \frac{\frac{\partial \bar{Z}_\alpha}{\partial P^*} + (1 + \sqrt{2}) \frac{\partial B_\alpha}{\partial P^*}}{\bar{Z}_\alpha + (1 - \sqrt{2}) B_\alpha} \right. \\
& \left. - \frac{\bar{Z}_\alpha + (1 - \sqrt{2}) B_\alpha}{(\bar{Z}_\alpha + (1 + \sqrt{2}) B_\alpha)^2} \left(\frac{\partial \bar{Z}_\alpha}{\partial P^*} + (1 - \sqrt{2}) \frac{\partial B_\alpha}{\partial P^*} \right) \right\}
\end{aligned} \tag{B.5}$$

$$\frac{\partial B_\alpha}{\partial P^*} = \sum_{i=2}^{N_c} \frac{\xi_{i\alpha} \Omega_{bi}^o}{T_{ri} p_{ci}} \tag{B.6a}$$

$$\frac{\partial A_\alpha}{\partial P^*} = \sum_{i=2}^{N_c} \sum_{j=2}^{N_c} \xi_{i\alpha} \xi_{j\alpha} \frac{\partial A_{ij}}{\partial P^*} \tag{B.6b}$$

$$\frac{\partial A_{ij}}{\partial P^*} = (1 - \delta_{ij}) \left[\left(\frac{A_i}{A_j} \right)^{0.5} \frac{\partial A_j}{\partial P^*} + \left(\frac{A_j}{A_i} \right)^{0.5} \frac{\partial A_i}{\partial P^*} \right] \tag{B.6c}$$

$$\frac{\partial A_i}{\partial P^*} = \Omega_{ai}^o [1 + m_i (1 - T_{ri}^{0.5})]^2 \frac{2p_{ri}}{p_{ci} T_{ri}} \tag{B.6d}$$

$$\frac{\partial B_i}{\partial P^*} = \frac{\Omega_{bi}^o}{T_{ri} p_{ci}} \tag{B.6e}$$

$$\frac{\partial C_i}{\partial P^*} = \frac{c_i}{RT} \tag{B.6f}$$

B.2.2 Derivative with respect to component concentration (N_k)

$$\begin{aligned}
\frac{\partial \ln(\Phi_{i\alpha})}{\partial N_k} = & -\frac{\partial C_i}{\partial N_k} + \left\{ \frac{(\bar{Z}_\alpha - 1)}{B_\alpha} \frac{\partial B_i}{\partial N_k} + \frac{B_i}{B_\alpha} \frac{\partial \bar{Z}_\alpha}{\partial N_k} - \frac{B_i}{B_\alpha^2} (\bar{Z}_\alpha - 1) \frac{\partial B_\alpha}{\partial N_k} \right\} \\
& - \frac{1}{(\bar{Z}_\alpha - B_\alpha)} \left\{ \frac{\partial \bar{Z}_\alpha}{\partial N_k} - \frac{\partial B_\alpha}{\partial N_k} \right\} - \Theta \left\{ \frac{1}{\sqrt{2}B_\alpha} \sum_{j=2}^{N_c} \xi_{i\alpha} \frac{\partial A_{ij}}{\partial N_k} - \frac{1}{\sqrt{2}B_\alpha} \sum_{j=2}^{N_c} A_{ij} \frac{\partial \xi_{j\alpha}}{\partial N_k} \right. \\
& \left. - \frac{\sum_{j=2}^{N_c} \xi_{i\alpha} A_{ij} \partial B_\alpha}{\sqrt{2}B_\alpha^2 \partial N_k} - \frac{B_i}{2\sqrt{2}B_\alpha^2} \frac{\partial A_\alpha}{\partial N_k} - \frac{A_\alpha}{2\sqrt{2}B_\alpha^2} \frac{\partial B_i}{\partial N_k} - \frac{B_i}{\sqrt{2}B_\alpha^3} A_\alpha \frac{\partial B_\alpha}{\partial N_k} \right\} \\
& - \Delta \left(\frac{\bar{Z}_\alpha + (1 - \sqrt{2})B_\alpha}{\bar{Z}_\alpha + (1 + \sqrt{2})B_\alpha} \right) \left\{ \frac{\frac{\partial \bar{Z}_\alpha}{\partial N_k} + (1 + \sqrt{2})\frac{\partial B_\alpha}{\partial N_k}}{\bar{Z}_\alpha + (1 - \sqrt{2})B_\alpha} \right. \\
& \left. - \frac{\bar{Z}_\alpha + (1 - \sqrt{2})B_\alpha}{(\bar{Z}_\alpha + (1 + \sqrt{2})B_\alpha)^2} \left(\frac{\partial \bar{Z}_\alpha}{\partial N_k} + (1 - \sqrt{2})\frac{\partial B_\alpha}{\partial N_k} \right) \right\}
\end{aligned} \tag{B.7}$$

$$\frac{\partial B_\alpha}{\partial N_k} = \sum_{i=2}^{N_c} \left(B_i \frac{\partial \xi_{i\alpha}}{\partial N_k} + \xi_{i\alpha} \frac{\partial B_i}{\partial N_k} \right) \tag{B.8a}$$

$$\frac{\partial A_\alpha}{\partial N_k} = \sum_{i=2}^{N_c} \sum_{j=2}^{N_c} \left(\xi_{i\alpha} \xi_{j\alpha} \frac{\partial A_{ij}}{\partial N_k} + \frac{\partial \xi_{j\alpha}}{\partial N_k} \xi_{i\alpha} A_{ij} + \frac{\partial \xi_{i\alpha}}{\partial N_k} \xi_{j\alpha} A_{ij} \right) \tag{B.8b}$$

$$\frac{\partial A_{ij}}{\partial N_k} = (1 - \delta_{ij}) \left[\left(\frac{A_i}{A_j} \right)^{0.5} \frac{\partial A_j}{\partial N_k} + \left(\frac{A_j}{A_i} \right)^{0.5} \frac{\partial A_i}{\partial N_k} \right] \tag{B.8c}$$

$$\frac{\partial A_i}{\partial N_k} = 0 \tag{B.8d}$$

$$\frac{\partial B_i}{\partial N_k} = 0 \tag{B.8e}$$

$$\frac{\partial C_i}{\partial N_k} = 0 \tag{B.8f}$$

$$\tag{B.8g}$$

$$\frac{\partial \xi_{io}}{\partial N_k} = \frac{1}{1 + (K_i - 1)\nu} \frac{\partial z_i}{\partial N_k} \quad (\text{B.9a})$$

$$\frac{\partial \xi_{ig}}{\partial N_k} = \frac{K_i}{1 + (K_i - 1)\nu} \frac{\partial z_i}{\partial N_k} \quad (\text{B.9b})$$

$$\frac{\partial z_i}{\partial N_k} = \frac{1}{\sum_{i=2}^{N_c} N_i} \frac{\partial N_i}{\partial N_k} - \frac{N_i}{\left(\sum_{i=2}^{N_c} N_i\right)^2} \frac{\partial}{\partial N_k} \sum_{i=2}^{N_c} N_i \quad (\text{B.9c})$$

$$\left. \frac{\partial N_i}{\partial N_k} \right|_{i \neq k} = 0 \quad (\text{B.9d})$$

$$\left. \frac{\partial N_i}{\partial N_k} \right|_{i=k} = 1 \quad (\text{B.9e})$$

B.2.3 Derivative with respect to $\ln K_k$

$$\frac{\partial \ln(\Phi_{i\alpha})}{\partial \ln K_k} = K_k \frac{\partial \ln(\Phi_{i\alpha})}{\partial K_k} \quad (\text{B.10})$$

$$\begin{aligned} \frac{\partial \ln(\Phi_{i\alpha})}{\partial K_k} = & -\frac{\partial C_i}{\partial K_k} + \left\{ \frac{(\bar{Z}_\alpha - 1)}{B_\alpha} \frac{\partial B_i}{\partial K_k} + \frac{B_i}{B_\alpha} \frac{\partial \bar{Z}_\alpha}{\partial K_k} - \frac{B_i}{B_\alpha^2} (\bar{Z}_\alpha - 1) \frac{\partial B_\alpha}{\partial K_k} \right\} \\ & - \frac{1}{(\bar{Z}_\alpha - B_\alpha)} \left\{ \frac{\partial \bar{Z}_\alpha}{\partial K_k} - \frac{\partial B_\alpha}{\partial K_k} \right\} - \Theta \left\{ \frac{1}{\sqrt{2}B_\alpha} \sum_{j=2}^{N_c} \xi_{i\alpha} \frac{\partial A_{ij}}{\partial K_k} - \frac{1}{\sqrt{2}B_\alpha} \sum_{j=2}^{N_c} A_{ij} \frac{\partial \xi_{j\alpha}}{\partial K_k} \right. \\ & \left. - \frac{\sum_{j=2}^{N_c} \xi_{i\alpha} A_{ij} \frac{\partial B_\alpha}{\partial K_k} - \frac{B_i}{2\sqrt{2}B_\alpha^2} \frac{\partial A_\alpha}{\partial K_k} - \frac{A_\alpha}{2\sqrt{2}B_\alpha^2} \frac{\partial B_i}{\partial K_k} - \frac{B_i}{\sqrt{2}B_\alpha^3} A_\alpha \frac{\partial B_\alpha}{\partial K_k} \right\} \\ & - \Delta \left(\frac{\bar{Z}_\alpha + (1 - \sqrt{2})B_\alpha}{\bar{Z}_\alpha + (1 + \sqrt{2})B_\alpha} \right) \left\{ \frac{\frac{\partial \bar{Z}_\alpha}{\partial K_k} + (1 + \sqrt{2})\frac{\partial B_\alpha}{\partial K_k}}{\bar{Z}_\alpha + (1 - \sqrt{2})B_\alpha} \right. \\ & \left. - \frac{\bar{Z}_\alpha + (1 - \sqrt{2})B_\alpha}{(\bar{Z}_\alpha + (1 + \sqrt{2})B_\alpha)^2} \left(\frac{\partial \bar{Z}_\alpha}{\partial K_k} + (1 - \sqrt{2})\frac{\partial B_\alpha}{\partial K_k} \right) \right\} \end{aligned} \quad (\text{B.11})$$

$$\frac{\partial B_\alpha}{\partial K_k} = \sum_{i=2}^{N_c} \left(B_i \frac{\partial \xi_{i\alpha}}{\partial K_k} + \xi_{i\alpha} \frac{\partial B_i}{\partial K_k} \right) \quad (\text{B.12a})$$

$$\frac{\partial A_\alpha}{\partial K_k} = \sum_{i=2}^{N_c} \sum_{j=2}^{N_c} \left(\xi_{i\alpha} \xi_{j\alpha} \frac{\partial A_{ij}}{\partial K_k} + \frac{\partial \xi_{j\alpha}}{\partial K_k} \xi_{i\alpha} A_{ij} + \frac{\partial \xi_{i\alpha}}{\partial K_k} \xi_{j\alpha} A_{ij} \right) \quad (\text{B.12b})$$

$$\frac{\partial A_{ij}}{\partial K_k} = (1 - \delta_{ij}) \left[\left(\frac{A_i}{A_j} \right)^{0.5} \frac{\partial A_j}{\partial K_k} + \left(\frac{A_j}{A_i} \right)^{0.5} \frac{\partial A_i}{\partial K_k} \right] \quad (\text{B.12c})$$

$$\frac{\partial A_i}{\partial K_k} = 0 \quad (\text{B.12d})$$

$$\frac{\partial B_i}{\partial K_k} = 0 \quad (\text{B.12e})$$

$$\frac{\partial C_i}{\partial K_k} = 0 \quad (\text{B.12f})$$

$$\frac{\partial \xi_{io}}{\partial K_k} = - \frac{z_i \nu}{[1 + (K_i - 1)\nu]^2} \frac{\partial K_i}{\partial K_k} \quad (\text{B.12g})$$

$$\frac{\partial \xi_{ig}}{\partial K_k} = \left\{ \frac{z_i}{1 + (K_i - 1)\nu} - \frac{z_i K_i \nu}{[1 + (K_i - 1)\nu]^2} \right\} \frac{\partial K_i}{\partial K_k} \quad (\text{B.12h})$$

$$\left. \frac{\partial K_i}{\partial K_k} \right|_{i \neq k} = 0 \quad (\text{B.12i})$$

$$\left. \frac{\partial K_i}{\partial K_k} \right|_{i=k} = 1 \quad (\text{B.12j})$$

B.2.4 Derivative with respect to ν

$$\begin{aligned}
\frac{\partial \ln(\Phi_{i\alpha})}{\partial \nu} = & -\frac{\partial C_i}{\partial \nu} + \left\{ \frac{(\bar{Z}_\alpha - 1) \partial B_i}{B_\alpha \partial \nu} + \frac{B_i \partial \bar{Z}_\alpha}{B_\alpha \partial \nu} - \frac{B_i (\bar{Z}_\alpha - 1) \partial B_\alpha}{B_\alpha^2 \partial \nu} \right\} \\
& - \frac{1}{(\bar{Z}_\alpha - B_\alpha)} \left\{ \frac{\partial \bar{Z}_\alpha}{\partial \nu} - \frac{\partial B_\alpha}{\partial \nu} \right\} - \Theta \left\{ \frac{1}{\sqrt{2} B_\alpha} \sum_{j=2}^{N_c} \xi_{i\alpha} \frac{\partial A_{ij}}{\partial \nu} - \frac{1}{\sqrt{2} B_\alpha} \sum_{j=2}^{N_c} A_{ij} \frac{\partial \xi_{j\alpha}}{\partial \nu} \right. \\
& \left. - \frac{\sum_{j=2}^{N_c} \xi_{i\alpha} A_{ij} \partial B_\alpha}{\sqrt{2} B_\alpha^2 \partial \nu} - \frac{B_i \partial A_\alpha}{2\sqrt{2} B_\alpha \partial \nu} - \frac{A_\alpha \partial B_i}{2\sqrt{2} B_\alpha^2 \partial \nu} - \frac{B_i A_\alpha \partial B_\alpha}{\sqrt{2} B_\alpha^3 \partial \nu} \right\} \\
& - \Delta \left(\frac{\bar{Z}_\alpha + (1 - \sqrt{2}) B_\alpha}{\bar{Z}_\alpha + (1 + \sqrt{2}) B_\alpha} \right) \left\{ \frac{\frac{\partial \bar{Z}_\alpha}{\partial \nu} + (1 + \sqrt{2}) \frac{\partial B_\alpha}{\partial \nu}}{\bar{Z}_\alpha + (1 - \sqrt{2}) B_\alpha} \right. \\
& \left. - \frac{\bar{Z}_\alpha + (1 - \sqrt{2}) B_\alpha}{(\bar{Z}_\alpha + (1 + \sqrt{2}) B_\alpha)^2} \left(\frac{\partial \bar{Z}_\alpha}{\partial \nu} + (1 - \sqrt{2}) \frac{\partial B_\alpha}{\partial \nu} \right) \right\}
\end{aligned} \tag{B.13}$$

$$\frac{\partial B_\alpha}{\partial \nu} = \sum_{i=2}^{N_c} \left(B_i \frac{\partial \xi_{i\alpha}}{\partial \nu} + \xi_{i\alpha} \frac{\partial B_i}{\partial \nu} \right) \tag{B.14a}$$

$$\frac{\partial A_\alpha}{\partial \nu} = \sum_{i=2}^{N_c} \sum_{j=2}^{N_c} \left(\xi_{i\alpha} \xi_{j\alpha} \frac{\partial A_{ij}}{\partial \nu} + \frac{\partial \xi_{j\alpha}}{\partial \nu} \xi_{i\alpha} A_{ij} + \frac{\partial \xi_{i\alpha}}{\partial \nu} \xi_{j\alpha} A_{ij} \right) \tag{B.14b}$$

$$\frac{\partial A_{ij}}{\partial \nu} = (1 - \delta_{ij}) \left[\left(\frac{A_i}{A_j} \right)^{0.5} \frac{\partial A_j}{\partial \nu} + \left(\frac{A_j}{A_i} \right)^{0.5} \frac{\partial A_i}{\partial \nu} \right] \tag{B.14c}$$

$$\frac{\partial A_i}{\partial \nu} = 0 \tag{B.14d}$$

$$\frac{\partial B_i}{\partial \nu} = 0 \tag{B.14e}$$

$$\frac{\partial C_i}{\partial \nu} = 0 \tag{B.14f}$$

$$\frac{\partial \xi_{io}}{\partial \nu} = -\frac{z_i (K_i - 1)}{[1 + (K_i - 1)\nu]^2} \tag{B.14g}$$

$$\frac{\partial \xi_{ig}}{\partial \nu} = -\frac{z_i K_i (K_i - 1)}{[1 + (K_i - 1)\nu]^2} \tag{B.14h}$$

Bibliography

- Gabor Acs, Sandor Doleschall, and Eva Farkas. General purpose compositional model. *Old SPE Journal*, 25(4):543–553, 1985.
- Omar Al-Hinai, Gurpreet Singh, Tameem M Almani, Gergina Pencheva, and Mary Fanett Wheeler. Modeling multiphase flow with nonplanar fractures. *SPE Reservoir Simulation Symposium, Woodlands, TX*, 2013.
- L Ambrosio and V M Tortorelli. Approximation of Functionals Depending on Jumps by Elliptic Functionals via Gamma-Convergence. *Communications on Pure and Applied Mathematics*, 43(8):999–1036, December 1990.
- Todd Arbogast, Mary F Wheeler, and Ivan Yotov. Mixed finite elements for elliptic problems with tensor coefficients as cell-centered finite differences. *SIAM Journal on Numerical Analysis*, 34(2):828–852, 1997.
- I. Babuska and U. Banerjee. Stable generalized finite element method (sgfem). *Comput. Methods Appl. Mech. Engrg.*, 201-204:91–111, 2012.
- I. Babuska and J.M. Belenk. The partition of unity method. *Int. J. Numer. Methods Engrg.*, 40:727–758, 1997.
- Wolfgang Bangerth, Timo Heister, Guido Kanschat, and many others. *Differential Equations Analysis Library*, 2012.

- Grigory Isaakovich Barenblatt. The mathematical theory of equilibrium cracks in brittle fracture. *Advances in applied mechanics*, 7(1), 1962.
- Peter Bastian, Z. Chen, R.E. Ewing, R. Helmig, H. Jakobs, and V. Reichenberger. *Numerical simulation of multiphase-flow in fractured porous media*, volume 522 of *Lecture Notes in Physics*. Springer, 2000.
- M A Biot. Consolidation Settlement Under a Rectangular Load Distribution. *Journal of applied physics*, 12(5):426, 1941a.
- M A Biot. Theory of Elasticity and Consolidation for a Porous Anisotropic Solid. *Journal of applied physics*, 26(2):182, 1955a.
- M.A. Biot. Consolidation settlement under a rectangular load distribution. *J. Appl. Phys.*, 12(5):426–430, 1941b.
- M.A. Biot. General theory of three-dimensional consolidation. *J. Appl. Phys.*, 12(2):155–164, 1941c.
- M.A. Biot. Theory of elasticity and consolidation for a porous anisotropic solid. *J. Appl. Phys.*, 25:182–185, 1955b.
- Maurice A Biot. General theory of threedimensional consolidation. *Journal of applied physics*, 12(2):155–164, 1941d.
- B. Bourdin, G.A. Francfort, and J.-J. Marigo. The variational approach to fracture. *J. Elasticity*, 91(1–3):1–148, 2008.

- B. Bourdin, C. Chukwudozie, and K. Yoshioka. A variational approach to the numerical simulation of hydraulic fracturing. SPE Journal, Conference Paper 159154-MS, 2012.
- Franco Brezzi, Jim Douglas, Jr, and L Donatella Marini. Two families of mixed finite elements for second order elliptic problems. *Numerische Mathematik*, 47(2):217–235, 1985.
- Franco Brezzi, Jim Douglas, Jr, Ricardo Durán, and Michel Fortin. Mixed finite elements for second order elliptic problems in three variables. *Numerische Mathematik*, 51(2):237–250, 1987.
- M. Hofacker C. Miehe, F. Welschinger. Thermodynamically consistent phase-field models of fracture: variational principles and multi-field fe implementations. *International Journal of Numerical Methods in Engineering*, 83: 1273–1311, 2010.
- S.T. Castonguay, M.E. Mear, R.H. Dean, and J.H. Schmidt. Predictions of the growth of multiple interacting hydraulic fractures in three dimensions. SPE Journal, Conference Paper 166259-MS, 2013.
- Yih-Bor Chang. Development and application of an equation of state compositional simulator, 1990.
- C. Chen, Y. Wang, and G. Li. Closed-loop reservoir management on the brugge test case. *Computational Geosciences*, 14:691–703, 2010.

- Keith Coats. An equation of state compositional model. *Old SPE Journal*, 20 (5):363–376, 1980.
- S.L. Crouch. Solution of plane elastic problem by the displacements discontinuity method. *Int. J. Num. Meth. in Eng.*, 10:301–343, 1976.
- R. de Borst, J. Rethoré, and M.A. Abellan. A numerical approach for arbitrary cracks in a fluid-saturated porous medium. *Arch. Appl. Mech.*, 75:595–606, 2006.
- R. H. Dean and J.H. Schmidt. Hydraulic fracture predictions with a fully coupled geomechanical reservoir simulator. *SPE Journal*, Conference Paper 116470-MS, 2008.
- R H Dean, X Gai, C M Stone, and S E Minkoff. A comparison of techniques for coupling porous flow and geomechanics. *SPE Journal*, 11(1):132–140, March 2006.
- M.J. Economides, D.A. Hill, and C.E. Economides. Petroleum production systems. *Text*.
- G. A. Francfort and J.-J. Marigo. Revisiting brittle fracture as an energy minimization problem. *J. Mech. Phys. Solids*, 46(8):1319–1342, 1998.
- Najla Frih, Jean E Roberts, and Ali Saada. Modeling fractures as interfaces: a model for Forchheimer fractures. *Computational Geosciences*, 12(1):91–104, January 2008.

- Benjamin Ganis, Vivette Girault, Mark Mear, Gurpreet Singh, and Mary Wheeler. Modeling Fractures in a Poro-Elastic Medium. *Oil & Gas Science and Technology – Revue d'IFP Energies nouvelles*, December 2013.
- Vivette Girault, M F Wheeler, Benjamin Ganis, and Mark Mear. A lubrication fracture model in a poro-elastic medium. *ICES Report*, pages 1–54, December 2013.
- A A Griffith. The Phenomena of Rupture and Flow in Solids. *Philosophical Transactions of the Royal Society of London. Series A, Containing Papers of a Mathematical or Physical Character*, 221:163–198, January 1921.
- A Grillo, D Logashenko, S Stichel, and G Wittum. Simulation of density-driven flow in fractured porous media. *Advances in Water Resources*, 33(12):1494–1507, 2010.
- H Hoteit and A Firoozabadi. Multicomponent fluid flow by discontinuous Galerkin and mixed methods in unfractured and fractured media. *Water Resources Research*, 41(11), November 2005.
- H Hoteit and A Firoozabadi. Compositional modeling of discrete-fractured media without transfer functions by the discontinuous Galerkin and mixed methods. *SPE Journal*, 11(3):341–352, September 2006.
- Hussein Hoteit and Abbas Firoozabadi. An efficient numerical model for incompressible two-phase flow in fractured media. *Advances in Water Resources*, 31(6):891–905, June 2008a.

- Hussein Hoteit and Abbas Firoozabadi. Numerical modeling of two-phase flow in heterogeneous permeable media with different capillarity pressures. *Advances in Water Resources*, 31(1):56–73, January 2008b.
- Ross Ingram, Mary F Wheeler, and Ivan Yotov. A Multipoint Flux Mixed Finite Element Method on Hexahedra. *SIAM Journal on Numerical Analysis*, 48(4):1281–1312, January 2010.
- G. Irwin. Elastizität und plastizität. Handbuch der Physik, Editor: S. Flügge, Bd. 6, 1958.
- S.D. Joshi. Horizontal well technology. *Text*.
- M Juntunen and Mary F Wheeler. Two-phase flow in complicated geometries. *Computational Geosciences*, 17(2), 2012.
- Zuleima Tharays Karpyn. Capillary-driven Flow in Fractured Sandstone, 2005.
- Jihoon Kim, Hamdi Tchelepi, and Ruben Juanes. Rigorous coupling of geomechanics and multiphase flow with strong capillarity. 2011.
- Jihoon Kim, Eric L Sonnenthal, and Jonny Rutqvist. Formulation and sequential numerical algorithms of coupled fluid/heat flow and geomechanics for multiple porosity materials. *International Journal for Numerical Methods in Engineering*, 92(5):425–456, June 2012.
- A Lauser, C Hager, R Helmig, and B Wohlmuth. A new approach for phase transitions in miscible multi-phase flow in porous media. *Advances in Water Resources*, 34(8):957–966, 2011.

- J. Lujun and A. Settari. A novel hydraulic fracturing model fully coupled with geomechanics and reservoir simulator. *SPE Journal*, Conference Paper 110845-MS, 2007.
- Vincent Martin, Jérôme Jaffré, and Jean E Roberts. Modeling Fractures and Barriers as Interfaces for Flow in Porous Media. *SIAM Journal on Scientific Computing*, 26(5):1667–1691, January 2005.
- M.L. Michelsen. Calculation of multiphase equilibrium. *Computers & chemical engineering*, 18(7):545–550, July 1994.
- A. Mikelić and M. F. Wheeler. Convergence of iterative coupling for coupled flow and geomechanics. *Comput Geosci*, 17(3):455–462, 2012.
- A. Mikelić, M.F. Wheeler, and T. Wick. A phase-field approach to the fluid filled fracture surrounded by a poroelastic medium. ICES-Preprint 13-15, Jun 2013a.
- A. Mikelić, M.F. Wheeler, and T. Wick. A quasi-static phase-field approach to the fluid filled fracture. ICES-Preprint 13-22, Aug 2013b.
- A. Mikelić, M.F. Wheeler, and T. Wick. A phase-field method for propagating fluid-filled fractures coupled to a surrounding porous medium. ICES Report 14-08, April 2014a.
- A. Mikelić, M.F. Wheeler, and T. Wick. Phase-field modeling of pressurized fractures in a poroelastic medium. ICES-Preprint 14-18, Jul 2014b.

- Andro Mikelic and Mary F Wheeler. Convergence of iterative coupling for coupled flow and geomechanics. *Computational Geosciences*, 17(3):455–461, October 2012.
- Andro Mikelic, Bin Wang, and Mary F Wheeler. Numerical convergence study of iterative coupling for coupled flow and geomechanics. *Computational Geosciences*, January 2014.
- N. Moes, J. Dolbow, and T. Belytschko. A finite element method for crack growth without remeshing. *Int. J. Numer. Methods Engrg.*, 46:131–150, 1999.
- Jorge Monteagudo and A Firoozabadi. Control-volume method for numerical simulation of two-phase immiscible flow in two- and three-dimensional discrete-fractured media. *Water Resources Research*, 40(7), July 2004.
- Jorge Monteagudo and Abbas Firoozabadi. Control-volume model for simulation of water injection in fractured media: incorporating matrix heterogeneity and reservoir wettability effects. *SPE Journal*, 12(3):355–366, 2007.
- R Okuno, R T Johns, and K Sepehrnoori. A New Algorithm for Rachford-Rice for Multiphase Compositional Simulation. *SPE Journal*, 15(2):313–325, June 2010.
- Donald W Peaceman. Interpretation of Well-Block Pressures in Numerical Reservoir Simulation. *Old SPE Journal*, 18(03):183–194, 1978.

- E. Peters, R. Arts, G. Brouwer, and C. Geel. Results of the Brugge benchmark study for flooding optimisation and history matching. *SPE 119094-MS. SPE Reservoir Simulation Symposium*, 2009.
- K. Pham, H. Amor, J.-J. Marigo, and C. Maurini. Gradient Damage Models and Their Use to Approximate Brittle Fracture. *Int. J. of Damage Mech.*, pages 1–36, May 2011.
- H.H. Rachford and J.D. Rice. Procedure for Use of Electronic Digital Computers in Calculating Flash Vaporization Hydrocarbon Equilibrium. *Transactions of the American Institute of Mining and Metallurgical Engineers*, 195:327–328, 1952.
- Osborne Reynolds. On the Theory of Lubrication and Its Application to Mr. Beauchamp Tower’s Experiments, Including an Experimental Determination of the Viscosity of Olive Oil. *Proceedings of the Royal Society of London*, 40(242-245):191–203, 1886.
- I F Roebuck, Jr, G E Henderson, Jim Douglas, Jr, and W T Ford. The compositional reservoir simulator: case I-the linear model. *Old SPE Journal*, 9(01):115–130, 1969.
- N.P. Roussel and M.M. Sharma. Quantifying transient effects in altered-stress refracturing of vertical wells. *SPE Hydraulic Fracturing Technology Conference*, 2009.

- S. Secchi and B. A. Schrefler. A method for 3-d hydraulic fracturing simulation. *Int J Fract*, 178:245–258, 2012.
- A Settari and D A Walters. Advances in coupled geomechanical and reservoir modeling with applications to reservoir compaction. *SPE Journal*, 6(3): 334–342, September 2001.
- Stewart A Silling. Reformulation of elasticity theory for discontinuities and long-range forces. *Journal of the Mechanics and Physics of Solids*, 48(1): 175–209, 2000.
- G Singh and Mary F Wheeler. Compositional Flow Modeling Using Multi-point Flux Mixed Finite Element Method. *ECMOR XIV-14th European conference on the ...*, 2014a.
- G. Singh, T. Wick, M.F. Wheeler, G. Pencheva, and K. Kumar. Impact of accurate fractured reservoir flow modeling on recovery predictions. SPE 188630-MS, SPE Hydraulic Fracturing Technology Conference, Woodlands, TX, 2014a.
- Gurpreet Singh. *Finite-volume Analysis of Two-phase Split at T-junctions*. PhD thesis, The Pennsylvania State University, 2009.
- Gurpreet Singh and Mary F Wheeler. Compositional Flow Modeling Using a Multi-point Flux Mixed Finite Element Method. *ICES Report 14-28*, pages 1–21, August 2014b.

- Gurpreet Singh, Gergina Pencheva, Kundan Kumar, Thomas Wick, Benjamin Ganis, and Mary F Wheeler. Impact of Accurate Fractured Reservoir Flow Modeling on Recovery Predictions. *SPE Hydraulic Fracturing Technology Conference*, 2014b.
- Gurpreet Singh, Thomas Wick, Mary F Wheeler, Gergina Pencheva, and Kundan Kumar. Coupled Flow and Geomechanics Modeling for Fractured Poroe-lastic Reservoirs. *ICES Report 14-17*, pages 1–22, July 2014c.
- Shuyu Sun and Abbas Firoozabadi. Compositional Modeling in Three-Phase Flow for CO₂ and other Fluid Injections using Higher-Order Finite Element Methods. *SPE Annual Technical Conference and Exhibition*, 2009.
- K. Terzaghi. *Theoretical soil mechanics*. J. Wiley, New York, 1943.
- Sunil George Thomas. On some problems in the simulation of flow and trans-
port through porous media. 2009.
- J W Watts. A compositional formulation of the pressure and saturation equa-
tions. *SPE Reservoir Engineering*, 1(3):243–252, 1986.
- Mary F Wheeler and Guangri Xue. Accurate locally conservative discretiza-
tions for modeling multiphase flow in porous media on general hexahedra
grids. *Proceedings of the 12th European Conference on the Mathematics of
Oil Recovery-ECMOR XII*, publisher EAGE, 2011.

- Mary F Wheeler and Ivan Yotov. A Multipoint Flux Mixed Finite Element Method. *SIAM Journal on Numerical Analysis*, 44(5):2082–2106, January 2006.
- Mary F Wheeler, Guangri Xue, and Ivan Yotov. A Family of Multipoint Flux Mixed Finite Element Methods for Elliptic Problems on General Grids. *Procedia Computer Science*, 4:918–927, January 2011a.
- Mary F Wheeler, Guangri Xue, and Ivan Yotov. A multipoint flux mixed finite element method on distorted quadrilaterals and hexahedra. *Numerische Mathematik*, 121(1):165–204, November 2011b.
- Mary F Wheeler, Guangri Xue, and Ivan Yotov. Accurate cell-centered discretizations for modeling multiphase flow in porous media on general hexahedral and simplicial grids. *SPE Reservoir Simulation Symposium*, 2011c.
- M.F. Wheeler, T. Wick, and W. Wollner. An augmented-Lagangrian method for the phase-field approach for pressurized fractures. *Comp. Meth. Appl. Mech. Engrg.*, 271:69–85, 2014a.
- M.F. Wheeler, T. Wick, and W. Wollner. An augmented-Lagangrian method for the phase-field approach for pressurized fractures. *Comp. Meth. Appl. Mech. Engrg.*, 271:69–85, 2014b.
- T. Wick. Solving monolithic fluid-structure interaction problems in arbitrary Lagrangian Eulerian coordinates with the deal.ii library. *Archive of Numerical Software*, 1:1–19, 2013.

- T. Wick, G. Singh, and M.F. Wheeler. Pressurized fracture propagation using a phase-field approach coupled to a reservoir simulator. SPE 168597-MS, SPE Proc., 2013.
- T. Wick, G. Singh, and M.F. Wheeler. Pressurized fracture propagation using a phase-field approach coupled to a reservoir simulator. SPE 168597-MS, SPE Hydraulic Fracturing Technology Conference, Woodlands, TX, 2014a.
- Thomas Wick, Gurpreet Singh, and Mary F Wheeler. Fluid-Filled Fracture Propagation using a Phase-Field Approach and Coupling to a Reservoir Simulator. *ICES Report 14-20*, pages 1–27, August 2014b.
- X. Xu and A. Needleman. Numerical simulations of fast crack growth in brittle solids. *Journal of the Mechanics and Physics of Solids*, 42:1397–1434, 1994.
- Larry Young and Robert Stephenson. A generalized compositional approach for reservoir simulation. *Old SPE Journal*, 23(5):727–742, 1983.

Vita

Gurpreet Singh was born in Dasuya, Punjab, India on 24 November 1984, the eldest son of Kabal Singh and Shivraj Kaur. He received a Bachelor of Technology degree in Chemical Engineering from the Guru Gobind Singh Indraprastha University in 2007. He then travelled to the United States of America to pursue Master of Science in Petroleum Engineering from the Pennsylvania State University. After finishing in Fall 2008, he applied to the doctoral degree program at the University of Texas at Austin in Petroleum Engineering where he started in Spring 2009.

Permanent address: 5/1/D Rail Vihar,
Mansa Devi Compex, Sector 4,
Panchkula, Haryana 134114

This dissertation was typeset with L^AT_EX[†] by the author.

[†]L^AT_EX is a document preparation system developed by Leslie Lamport as a special version of Donald Knuth's T_EX Program.